



Oskar J. Sandberg

# Charge collection in thin-film devices based on low-mobility semiconductors

Theory, simulation, and applications to organic solar cells



# Charge collection in thin-film devices based on low-mobility semiconductors

Theory, simulation, and applications  
to organic solar cells

OSKAR J. SANDBERG

PHYSICS

CENTER FOR FUNCTIONAL MATERIALS

NATIONAL GRADUATE SCHOOL IN NANOSCIENCE (NGS-NANO)

FACULTY OF SCIENCE AND ENGINEERING

ÅBO AKADEMI UNIVERSITY

ÅBO 2018

*Supervisor*

PROFESSOR RONALD ÖSTERBACKA  
PHYSICS, CENTER FOR FUNCTIONAL MATERIALS  
ÅBO AKADEMI UNIVERSITY

*Pre-examiners*

PROFESSOR THOMAS KIRCHARTZ  
IEK5-PHOTOVOLTAIK  
FORSCHUNGSZENTRUM JÜLICH

PROFESSOR CARSTEN DEIBEL  
INSTITUT FÜR PHYSIK  
TECHNISCHE UNIVERSITÄT CHEMNITZ

*Opponent for the public defense*

ASSOCIATE PROFESSOR MORITZ RIEDE  
DEPARTMENT OF PHYSICS  
UNIVERSITY OF OXFORD

ISBN 978-952-12-3719-5  
PAINOSALAMA OY – TURKU, FINLAND 2018

# Contents

|   |            |
|---|------------|
| <b>Contents</b>   | <b>iii</b> |
| <b>Preface</b>  | <b>vii</b> |
| Acknowledgments . . . . .   | vii        |
| List of included publications . . . . .   | ix         |
| Author's contribution to the included articles . . . . .                                | x          |
| List of additional publications . . . . .   | xi         |
| <b>1 Basic concepts and principles</b>  | <b>1</b>   |
| 1.1 Introduction . . . . .  | 1          |
| 1.1.1 Thin-film diodes . . . . .  | 2          |
| 1.1.2 Organic bulk heterojunction solar cells . . . . .                                 | 4          |
| 1.2 Electronic processes in disordered materials . . . . .                              | 5          |
| 1.2.1 Inorganic semiconductors . . . . .  | 6          |
| 1.2.2 Organic semiconductors . . . . .  | 9          |
| 1.3 The charge transport equations . . . . .  | 11         |
| 1.3.1 The drift-diffusion equations . . . . .   | 12         |
| 1.3.2 Drift-diffusion and mobility from the viewpoint of hopping<br>transport . . . . . | 14         |
| 1.3.3 Generation and recombination processes in the bulk . . . .                        | 16         |
| 1.3.4 Space charge . . . . .  | 23         |
| 1.4 The motivation and scope . . . . .  | 25         |
|   | iii        |

|          |   |           |
|----------|---|-----------|
| <b>2</b> | <b>Current injection and collection in thin-film devices</b>                                  | <b>27</b> |
| 2.1      | Sandwich-type thin-film structures . . . . .  | 28        |
| 2.1.1    | Metal-semiconductor interfaces . . . . .  | 28        |
| 2.1.2    | The metal-insulator-metal (MIM) concept . . . . .   | 30        |
| 2.1.3    | Ohmic contacts . . . . .  | 31        |
| 2.1.4    | The image charge effect . . . . .   | 35        |
| 2.2      | Charge-transfer mechanisms at electrode-semiconductor contacts                                | 36        |
| 2.2.1    | Thermionic emission and the concept of surface recombination at contacts . . . . .            | 36        |
| 2.2.2    | Interpretation of the surface recombination velocity at contacts in hopping systems . . . . . | 38        |
| 2.3      | Unipolar charge transport in thin-film devices . . . . .                                      | 40        |
| 2.3.1    | Theory . . . . .  | 41        |
| 2.3.2    | Diffusion-limited currents . . . . .  | 43        |
| 2.3.3    | Space-charge-limited currents . . . . .   | 44        |
| 2.3.4    | Injection-limited currents . . . . .  | 45        |
| 2.3.5    | Ohmic linear current-voltage regime . . . . .   | 47        |
| 2.3.6    | The case with a doped semiconductor layer; the Schottky barrier . . . . .                     | 47        |
| 2.3.7    | The impact of the recombination velocity at the collecting contact . . . . .                  | 49        |
| 2.4      | Bipolar currents in thin-film devices . . . . .   | 51        |
| 2.4.1    | The case when bulk recombination dominates . . . . .  | 54        |
| 2.4.2    | The case when surface recombination dominates . . . . .                                       | 55        |
| 2.4.3    | Space-charge-limited double-injection currents . . . . .                                      | 57        |
| <b>3</b> | <b>Charge extraction by a linearly increasing voltage pulse</b>                               | <b>59</b> |
| 3.1      | Basic theory . . . . .  | 60        |
| 3.1.1    | Low-conductivity regime . . . . .   | 60        |
| 3.1.2    | Moderate-conductivity regime; the impact of space charge                                      | 62        |
| 3.1.3    | Influence of bulk recombination . . . . .   | 63        |

|          |   |           |
|----------|---|-----------|
| 3.1.4    | Non-uniform carrier distributions . . . . .   | 65        |
| 3.2      | CELIV on doped samples; the impact of the built-in voltage . . .  | 66        |
| 3.2.1    | The transport-limited regime . . . . .  | 67        |
| 3.2.2    | The capacitive regime . . . . .   | 68        |
| 3.2.3    | Using CELIV to measure the built-in voltage and the dop-<br>ing concentration . . . . .                   | 70        |
| 3.3      | Extraction of carriers injected into structures with blocking contacts                                    | 71        |
| 3.3.1    | Space-charge-limited extraction current transients . . . .  | 72        |
| 3.3.2    | Effect of diffusion in thin-film devices . . . . .  | 74        |
| 3.3.3    | Using CELIV to measure surface recombination velocity<br>at blocking contacts . . . . .                   | 75        |
| <b>4</b> | <b>Charge collection and the effect of contacts in organic thin-film<br/>solar cells</b>                  | <b>77</b> |
| 4.1      | Charge transport and recombination in organic solar cells . . . .   | 78        |
| 4.1.1    | Negligible recombination between photoinduced carriers .  | 78        |
| 4.1.2    | Charge transport <i>vs.</i> bulk recombination . . . . .  | 80        |
| 4.1.3    | Diffusion-limited photocurrents . . . . .   | 83        |
| 4.2      | The role of the contacts . . . . .  | 84        |
| 4.2.1    | Simplified analytical model . . . . .   | 84        |
| 4.2.2    | Competition between bulk recombination and surface re-<br>combination in case of ohmic contacts . . . . . | 87        |
| 4.2.3    | Interplay between bulk recombination and surface recom-<br>bination at non-ohmic contacts . . . . .       | 90        |
| 4.2.4    | Poor extraction of majority carriers at the contacts . . . .  | 96        |
| 4.3      | The impact of space charge on the photocurrent . . . . .  | 98        |
| 4.3.1    | The influence of a doping-induced space-charge region . .   | 98        |
| 4.3.2    | Space-charge-limited photocurrents due to imbalanced mo-<br>bilities . . . . .                            | 101       |
| 4.3.3    | The effect of a space-charge region in the vicinity of the<br>electrode . . . . .                         | 103       |

## Contents

|          |   |            |
|----------|---|------------|
| 4.4      | Experimental demonstration on inverted organic solar cell devices                       | 105        |
| 4.4.1    | The model system $\text{TiO}_2/\text{P3HT:PCBM}$ and the light-soaking effect . . . . . | 106        |
| 4.4.2    | Investigating the reason for the s kink in the $J$ - $V$ curve using CELIV . . . . .    | 106        |
| 4.4.3    | Light-intensity-dependent open-circuit voltage measurements . . . . .                   | 109        |
| 4.4.4    | The surface recombination velocity of holes at $\text{TiO}_2/\text{P3HT}$               | 110        |
| <b>5</b> | <b>Summary</b>  | <b>113</b> |
|          | <b>Bibliography</b>   | <b>115</b> |
|          | <b>Svensk resumé</b>  | <b>129</b> |

# Preface

This thesis summarizes my main research during the time period 2012 to 2017 and is based on six scientific articles, Papers I to VI, as given in the List of included publications. The research was carried out at the physics department at Åbo Akademi University, within the organic electronics group, under the supervision of Professor Ronald Österbacka. Although the research is focused on organic electronics, and in particular organic solar cells, the results of the thesis are generally applicable to sandwich-type thin-film devices based on low-mobility semiconductors. The articles are the result of collaboration with other members within the research group and people from the physical chemistry department; the contributions by the author of this thesis to the articles are specified in the Author's contribution to the included articles section below. Apart from these six articles, the author have also taken part in 16 other articles ([Paper 1–Paper 16], see List of additional publications), some of which are closely related to the work in this thesis.

## Acknowledgments

I am greatly thankful for the funding from The Finnish National Doctoral Programme in Nanoscience (NGS-NANO), The Magnus Ehrnrooth Foundation, The Swedish Cultural Foundation in Finland, and Academy of Finland.

I would like to thank my supervisor Professor Ronald Österbacka for giving me the opportunity to work within the area of organic electronics, for his wisdom



## *Preface*

and invaluable advice, and for giving me the freedom to pursue new ideas. I have learned a lot and I hope to continue carrying out research in one way or another within this fascinating area for many years to come.

I would like to thank Mathias Nyman for interesting discussions, practical advice, and collaboration during the years, and for always being ready to act as a sounding board (*bullplank*) regarding the feasibility of my theoretical ideas from an experimental point of view. I also want to thank Simon Sandén, Jan-Henrik Smått, and in particular Anton Sundqvist and Staffan Dahlström for sweating in the lab and making the experiments.

A big thanks to all other friends, fellow students, researchers and staff at the physics department, for inspirational discussions, for support and help with various things, and for making my long journey to the PhD degree a funnier experience. I also want to thank my friends and family in Ostrobothnia. Last but definitely not least, I would like to thank my Hannele for her love, encouragement, and support.

Oskar Sandberg  
Åbo, May 2018

## List of included publications

This thesis is based on the following six publications.

- I. *Determination of surface recombination velocities at contacts in organic semiconductor devices using injected carrier reservoirs*,  
O. J. Sandberg, S. Sandén, A. Sundqvist, J.-H. Smått, and R. Österbacka,  
Phys. Rev. Lett. **118**, 076601 (2017)      © 2017 AMERICAN PHYSICAL SOCIETY
- II. *Direct determination of doping concentration and built-in voltage from extraction current transients*,  
O. J. Sandberg, M. Nyman, and R. Österbacka,  
Org. Electron. **15**, 3413 (2014)      © 2014 ELSEVIER BV
- III. *On the validity of MIS-CELIV for mobility determination in organic thin-film devices*,  
O. J. Sandberg, M. Nyman, S. Dahlström, S. Sandén, B. Törngren, J.-H. Smått, and R. Österbacka,  
Appl. Phys. Lett. **110**, 153504 (2017)      © 2017 AMERICAN INSTITUTE OF PHYSICS
- IV. *Relating charge transport, contact properties, and recombination to open-circuit voltage in sandwich-type thin-film solar cells*  
O. J. Sandberg, A. Sundqvist, M. Nyman, and R. Österbacka,  
Phys. Rev. Applied **5**, 044005 (2016)      © 2016 AMERICAN PHYSICAL SOCIETY
- V. *Effect of contacts in organic bulk heterojunction solar cells*,  
O. J. Sandberg, M. Nyman, and R. Österbacka,  
Phys. Rev. Applied **1**, 024003 (2014)      © 2014 AMERICAN PHYSICAL SOCIETY
- VI. *Origin of the S-shaped JV curve and the light-soaking issue in inverted organic solar cells*,  
A. Sundqvist, O. J. Sandberg, M. Nyman, J.-H. Smått, and R. Österbacka,  
Adv. Energy Mater. **6**, 1502265 (2016)      © 2016 WILEY-VCH

## Author's contribution to the included articles

- I. The author planned the work, developed the analytical theory, performed all the numerical simulations, wrote the first draft of the manuscript, applied the theory to experiments made by S. Sandén and A. Sundqvist, and finalized the manuscript together with the co-authors.
- II. The author planned the work together with M. Nyman. The author developed the analytical theory, performed all the numerical simulations, wrote the first draft of the paper and finalized it with the co-authors. The experiments were executed by M. Nyman.
- III. The author planned the work together with M. Nyman. The author performed all the analytical and numerical calculations, analyzed the numerical results, and wrote the first draft of the paper. The experiments were executed by S. Dahlström, aided by the other co-authors. The author finalized the paper together with the co-authors.
- IV. The author planned the work, performed the numerical simulations, derived the analytical results, wrote the first draft of the paper and finalized it with the co-authors.
- V. The author planned and analyzed the results together with M. Nyman. The author performed all the numerical simulations and the analytical derivations, wrote the first draft and finalized the paper with the co-authors.
- VI. The author executed the numerical modelling and theoretical analysis. Participated in planning the work and writing the first draft of the paper together with A. Sundqvist and M. Nyman. The experiments and device fabrication was executed by A. Sundqvist.

## List of additional publications

1. *Determination of Charge-Carrier Mobility and Built-In Potential in Thin-Film Organic MIM Diodes from Extraction Current Transients*,  
S. Dahlström, O. J. Sandberg, M. Nyman and R. Österbacka,  
Submitted
2. *Effect of the depletion layer capacitance on the mobility determination using transient current extraction of doping-induced charge carriers*,  
O. J. Sandberg, M. Nyman, S. Dahlström and R. Österbacka,  
J. Photon. Energy. **8**, 032208 (2018)
3. *Doping-induced carrier profiles in organic semiconductors determined from capacitive extraction-current transients*,  
M. Nyman, O. J. Sandberg, S. Dahlström, D. Spoltore, C. Körner, Y. Zhang, S. Barlow, S. R. Marder, K. Leo, K. Vandewal, and R. Österbacka,  
Sci. Rep. **7**, 5397 (2017)
4. *Impact of film thickness of thin dip-coated compact TiO<sub>2</sub> layers on the performance of mesoscopic perovskite solar cells*,  
T. Masood, C. Weinberger, J. Sarfraz, E. Rosqvist, S. Sandén, O. J. Sandberg, P. Vivo, S. G. Hashmi, P. D. Lund, R. Österbacka, and J.-H. Smått,  
ACS Appl. Mater. Interfaces **9**, 17906 (2017)
5. *Method for characterizing bulk recombination using photoinduced absorption*,  
N. M. Wilson, S. Sandén, O. J. Sandberg, and R. Österbacka,  
J. Appl. Phys. **121**, 095701 (2017)
6. *Unintentional bulk doping of polymer-fullerene blends from a thin interfacial layer of MoO<sub>3</sub>*,  
M. Nyman, S. Dahlström, O. J. Sandberg, and R. Österbacka,  
Adv. Energy Mater. **6**, 1600670 (2016)

7. *Characterization of the dominating bulk recombination in bulk-heterojunction blends using photoinduced absorption*,  
S. Sandén, N. M. Wilson, O. J. Sandberg, and R. Österbacka,  
Appl. Phys. Lett. **108**, 193301 (2016)
8. *Effect of two-dimensional-Langevin and trap-assisted recombination on the device performance of organic solar cells*,  
M. Nyman, O. J. Sandberg, R. Österbacka,  
J. Photon. Energy. **6**, 014501 (2016)
9. *Transient extraction of holes and electrons separately unveils the transport dynamics in organic photovoltaics*,  
J. Peng, X. Chen, Y. Chen, O. J. Sandberg, R. Österbacka, and Z. Liang,  
Adv. Electron. Mater. **2**, 1500333 (2016)
10. *2D- and trap-assisted 2D-Langevin recombination in polymer:fullerene blends*,  
M. Nyman, O. J. Sandberg, and R. Österbacka,  
Adv. Energy Mater. **5**, 1400890 (2015).
11. *Charge transport in intercalated and non-intercalated polymer:fullerene blends*,  
M. Nyman, O. J. Sandberg, and R. Österbacka,  
Synthetic Metals **201**, 6 (2015)
12. *Charge transport in  $\text{TiO}_2$ /organic devices measured using photo-CELIV: Influence of equilibrium charge reservoir formation*,  
S. Sandén, O. J. Sandberg, Q. Xu, J.-H. Smått, G. Juška, M. Lindén, and R. Österbacka,  
Org. Electron. **15**, 3506 (2014)
13. *Trap-assisted recombination via integer charge transfer states in organic bulk heterojunction photovoltaics*,  
Q. Bao, O. Sandberg, S. Sandén, S. Braun, H. Aarnio, X. Liu, R. Österbacka, and M. Fahlman,  
Adv. Funct. Mater. **24**, 6309 (2014).

14. *Voltage dependent displacement current as a tool to measure the vacuum level shift caused by self-assembled monolayers on aluminum oxide*,  
M. Nyman, O. Sandberg, J. F. Martinez Hardigree, S. Kola, H. E. Katz,  
and R. Österbacka,  
Appl. Phys. Lett. **103**, 243502 (2013)
15. *Effect of a large hole reservoir on the charge transport in TiO<sub>2</sub>/organic hybrid devices*,  
S. Sandén, O. Sandberg, Q. Xu, J.-H. Smått, G. Juška, M. Lindén, and  
R. Österbacka,  
Phys. Chem. Chem. Phys. **14**, 14186-14189 (2012)
16. *The effect of 2D-Langevin and trap-assisted recombination on the open circuit voltage in organic solar cells*,  
M. Nyman, O. J. Sandberg, and R. Österbacka,  
Proc. SPIE 9567, Organic Photovoltaics XVI, 95670C (September 9,  
2015); Conference proceeding

## *Preface*

## CHAPTER 1

# Basic concepts and principles

### 1.1 Introduction

Devices based on organic semiconductors exhibit great potential for future electronics. This includes sandwich-type thin-film devices such as diodes, solar cells, photodetectors, and light-emitting diodes, but also other type of structures such as field-effect transistors [1–3]. Currently, organic light-emitting diodes (OLED) are commercially available. Another emerging organic diode application that is receiving more and more attention is organic solar cells [4–6]. The commercial solar cells on the market today are almost exclusively made of inorganic semiconductors, mainly crystalline silicon. The disadvantage of crystalline silicon is the relatively expensive manufacturing process, requiring a large amount of material. This issue may be overcome with flexible thin-film structures based on organic semiconductors. The main advantage of organic semiconductors is the potential for large-area production using cheap materials at low processing temperatures [2]. Moreover, the properties of organic semiconductors can be manipulated and fine-tuned by organic chemistry, with the promise of environmental-friendly materials. A disadvantage of organic solar cells is their low power conversion efficiencies (PCE), currently being at  $\leq 11.5\%$ ; this is to be compared to the 20-25% typically encountered in conventional  $p$ - $n$  junction



solar cells based on silicon [7]. An emerging organic-inorganic hybrid thin-film solar cell technology that has recently exceeded PCEs of 20% is perovskite solar cells [8–10]. Currently, the main disadvantages of perovskite solar cells are related to the stability and the hazardous materials used in the manufacturing of the active components.

### 1.1.1 Thin-film diodes

A thin-film diode is composed of a thin (intrinsic) semiconductor layer, constituting the active layer, sandwiched between two electrodes, referred to as the anode and the cathode. A schematic picture is shown in Figure 1.1(a). The charge conduction in the semiconductor is carried by negatively-charged electrons in the conduction band and/or positively-charged holes (empty electron states) in the valence band. By applying an external voltage  $V$  to the anode, relative to the cathode, a current of charge carriers will flow through the diode, depending on the polarity of the voltage. The corresponding steady-state current density  $J$ , in accordance with the equivalent-circuit-diode model, is generally of the form

$$J = J_0 \left[ \exp \left( \frac{q[V - JR_s]}{\eta_{id}kT} \right) - 1 \right] + \frac{V - JR_s}{R_{sh}} - J_L, \quad (1.1.1)$$

where  $J_0$  is the dark saturation current,  $\eta_{id}$  is the diode ideality factor, and  $J_L$  is the photoinduced current obtained by illuminating the diode by external photons;  $q$  is the elementary charge,  $k$  is the Boltzmann constant, and  $T$  is the temperature. Furthermore,  $R_s$  is the series resistance (in  $\Omega\text{m}^2$ ) of the external circuit (electrodes and the external wires) and  $R_{sh}$  is the shunt resistance (in  $\Omega\text{m}^2$ ) describing unintentional leakage currents going "around the device" via parasitic conductive pathways within the layer [11]; in the ideal case, these external non-idealities are negligible and  $R_s = 1/R_{sh} = 0$ . A schematic picture of the equivalent circuit is given in Figure 1.1(b). The parameters  $J_0$ ,  $\eta_{id}$ , and  $J_L$  are determined by both material properties of the semiconductor and device

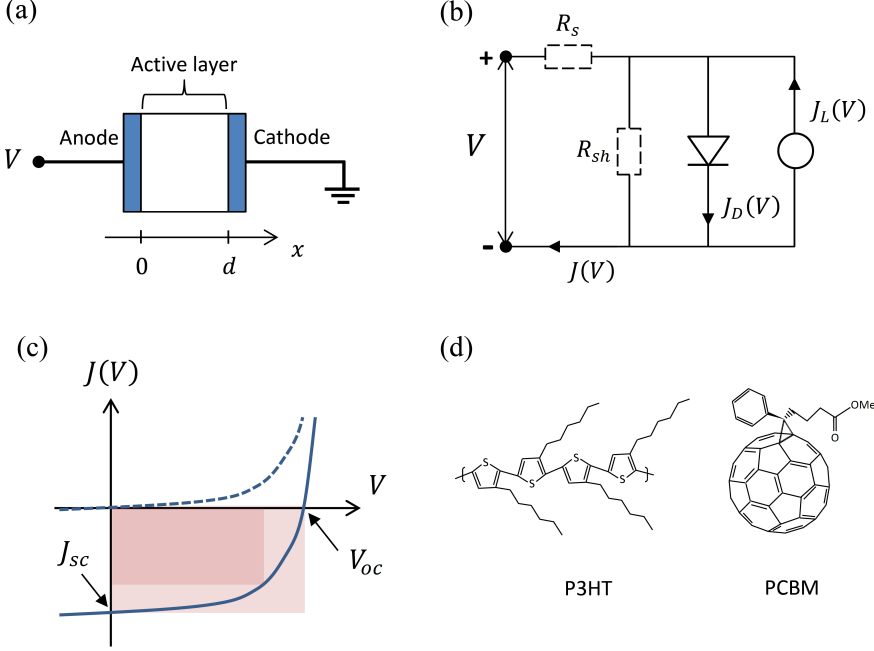


Figure 1.1: (a) A schematic picture of a sandwich-type thin-film diode. The device is composed of an active semiconductor layer, sandwiched between an anode and a cathode. The equivalent circuit of the device is illustrated in (b), where  $J_D(V)$  is the current density component that flows through the diode in the dark. (c) The current-voltage characteristics obtained by applying a voltage  $V$  to the anode, relative to the cathode. The dashed and solid curve corresponds to a diode in dark and under illumination, respectively; the Fill Factor ( $FF$ ) is determined by the ratio of the dark-shaded area relative to the overall shaded area. (d) Example of two organic semiconductors: the polymer poly-(3-hexylthiophene) (P3HT) and the fullerene derivative [6,6]-phenyl-C61-butyric acid methyl ester (PCBM).

parameters, such as the active layer thickness  $d$ , and generally depend on the applied voltage as well. In dark ( $J_L = 0$ ), the diode conducts current under positive voltages (forward bias), whereas the current is suppressed at negative voltages (reverse bias).

By illuminating the diode with an external photon source (of photons with suitable energy), electrons may be promoted to the conduction band, leaving

holes in the valence band; these photoinduced charge carriers give rise to the additional current component  $J_L$  flowing in the reverse direction of the diode. Under these conditions, the diode operates as a photodetector. In case of sun light, the photodetector becomes a solar cell. The current-voltage characteristics ( $J$ - $V$  curve) of a solar cell is depicted in Figure 1.1(c). The power conversion efficiency is given by  $\text{PCE} = -J(V_m)V_m/P_{in}$ , where  $P_{in}$  is the incoming (areal) sun power (of the standard AM 1.5 sun spectra) and  $V_m$  is the voltage at which the output power  $P = -J(V)V$  is at its maximum. The key parameters to be maximized for optimum PCE are the fill factor  $FF \equiv J(V_m)V_m/J_{sc}V_{oc}$ , the short-circuit current  $J_{sc} \equiv J(0)$ , and the open-circuit voltage  $V_{oc} \equiv V(J=0)$ .

### 1.1.2 Organic bulk heterojunction solar cells

In an organic thin-film diode, the active layer is composed of an organic semiconductor, typically a semiconducting polymer, a fullerene, or a small molecule. In dark, the current conduction in the active layer is enabled by charge-carrier injection from the electrode contacts. The properties of the contacts are chosen so that the anode is hole-injecting and/or the cathode is electron-injecting. In forward bias, holes (electrons) are then injected from the anode (cathode) into the active layer, giving rise to the dark current. Examples of two common organic semiconductors that have been widely used in diode and solar cell applications are shown in Figure 1.1(d).

The first organic solar cells were based on a single-semiconductor active layer and exhibited poor power conversion efficiencies well below 1% [12]. Although active layers of only a few hundred nm are needed to effectively absorb photons in most organic semiconductors, these types of organic solar cells are not able to convert a sufficient amount of photoexcitations into free charge carriers. As a photon of sufficient energy is absorbed, an electron is promoted to an excited state leaving a hole behind in the ground state. The subsequent electron-hole pair, commonly referred to as an exciton, is bound together by the mutual coulomb attraction. In organic materials the screening of the electric

field is weak (low dielectric constant), resulting in electron-hole pairs that are strongly bound ( $\gg kT$ ). (This in contrast to inorganic semiconductors, where excitons are weakly bound and dissociate spontaneously to free carriers.) Consequently, following the excitation event, the charge-neutral exciton execute a random walk within the organic layer during the excitation lifetime after which a transition back to the ground state takes place [13]. This issue can be overcome by adding a semiconductor with electron-accepting properties into the active layer, as demonstrated by Tang [14].

Most organic solar cells today are based on blends of two different organic semiconductors: an electron-donating semiconductor (donor, D) and an electron-accepting semiconductor (acceptor, A) [5]. The D:A blend forms an interpenetrating network of separate donor and acceptor phases. This blend is referred to as a bulk heterojunction (BHJ). When an exciton, commonly photoexcited within the donor phase, reach a D-A interface, a charge transfer takes place with the exciton ultimately dissociating into free carriers. In order to harvest an optimal amount of excitons, the phase separation should roughly be twice the exciton diffusion length. Following the charge transfer process (generally occurring via intermediate steps), the electron is located in the acceptor phase and the hole is in the donor [5, 13]. The free electron (hole) is subsequently transported within the acceptor (donor) phase towards the cathode (anode). The electrons and holes that avoid charge-carrier recombination on the way to the electrodes can finally be collected to the external circuit and contribute to the photocurrent. This competition between charge-carrier collection and recombination in organic solar cells is strongly dependent on the charge transport properties of the active semiconductor layer.

## 1.2 Electronic processes in disordered materials

The charge transport properties of a solid is typically classified according to its conductivity, determined by the density of free charge carriers and their mobilities. At thermal equilibrium, the electron and hole density is given by

$$n = \int_{-\infty}^{\infty} g(E) f(E) dE, \quad (1.2.1)$$

$$p = \int_{-\infty}^{\infty} g(E) [1 - f(E)] dE, \quad (1.2.2)$$

respectively, where  $g(E)$  is the associated density of states (DOS) and  $f(E)$  is the occupation probability given by the Fermi-Dirac distribution:

$$f(E) = \frac{1}{1 + \exp\left(\frac{E - E_F}{kT}\right)}, \quad (1.2.3)$$

where  $E_F$  is the Fermi level. At low carrier densities, when the Fermi level is several  $kT$  below the (effective) conduction level edge and several  $kT$  above the (effective) valence level edge, the Boltzmann approximation applies:  $f(E) \approx \exp([E_F - E]/kT)$  and  $1 - f(E) \approx \exp([E - E_F]/kT)$  for electrons and holes, respectively. This is referred to as the non-degenerate limit. The charge-carrier mobility describes the proportionality between the velocity of carriers drifting within the material and the electric field. Under the influence of an external electric field  $F$ , the corresponding drift velocity is given by  $v_{dr} = \mu F$ , where  $\mu$  is the mobility of the carriers (electrons in conduction band or holes in valence band). The mobility is strongly dependent on the electronic energy structure of the material.

### 1.2.1 Inorganic semiconductors

Solid crystals based on inorganic semiconductors, such as Si, consist of an ordered structure of covalently bound atoms. In this structure, the nearest-neighbor distances between atoms are small enough for the wave functions of the outer valence electrons to overlap. Due to the strong interaction, the atomic valence energy levels form continuous bands of extended states, delocalized over the entire crystal. The carrier transport occurs within the highest occupied energy band (valence band) and the lowest unoccupied band (conduction band).

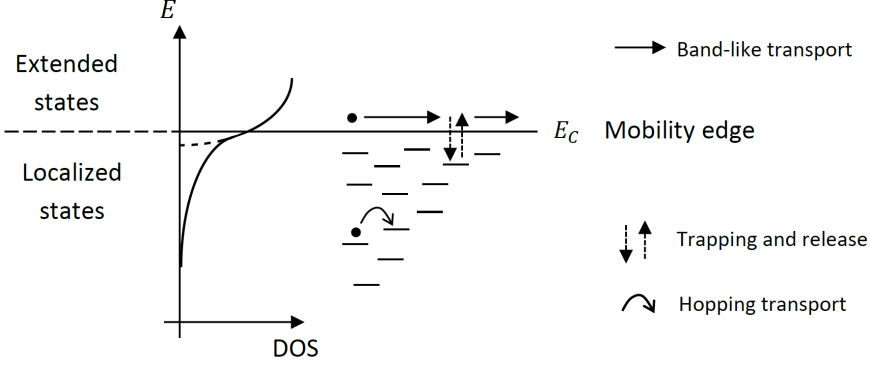


Figure 1.2: Schematic of the electronic structure in disordered inorganic semiconductors. Within the band of extended states, electrons are delocalized and the conduction occurs by band-like transport. In the band (mobility) gap,  $E_V < E < E_C$ , the states are localized and the conduction takes place by hopping.

Electrons and holes introduced into the conduction band and valence band, respectively, effectively behave as a gas of free carriers, executing random thermal motion within the crystal. Under the influence of a small electric field, the carrier transport in the bulk is only limited by scattering with lattice vibrations and impurities, and the carrier mobility can qualitatively be expressed as [15]

$$\mu = \frac{q}{m^*} \tau_{sc} , \quad (1.2.4)$$

where  $\tau_{sc}$  is the effective carrier scattering time, and  $m^*$  is the effective mass. This type of conduction mechanism is referred to as band transport. Typical values for the mobility are on the order of  $100 \text{ cm}^2/\text{Vs}$  and larger. The density of states within the conduction band is  $g(E) = 2N_C [(E - E_C)/kT]^{1/2} / (\sqrt{\pi}kT)$  for  $E > E_C$ , and zero otherwise; here,  $E_C$  is the conduction band edge and  $N_C$  is the effective density of states in the conduction band [15]. In the non-degenerate

limit, the electron density in the conduction band is

$$n = N_C \exp \left( \frac{E_F - E_C}{kT} \right). \quad (1.2.5)$$

An analogous expression is valid for the hole density in the valence band, at  $E < E_V$ , where  $E_V$  is the valence band edge.

In amorphous inorganic materials, the atomic structure is disordered, consisting of a random network of covalently bound atoms. Although delocalized extended states resembling energy bands are still present, owing to the disorder-induced broadening of the energy levels, localized tail states are present within the band gap [16]. In this case,  $E_C$  corresponds to the mobility edge, which is the energy level separating extended delocalized states in the conduction band from localized tail states. A schematic picture is shown in Figure 1.2. The density of localized tail states is typically characterized with an exponential distribution [16],  $g_t(E) = [N_{Ct}/E_{ch}] \exp([E - E_C]/E_{ch})$  for  $E < E_C$ , where  $E_{ch}$  is the characteristic energy and  $N_{Ct}$  is the density of tail states. For  $E_{ch} > kT$ , the density of electrons in the tail states can be evaluated as [17]

$$n_t = N_{Ct} \exp \left( \frac{E_F - E_C}{E_{ch}} \right) \times \left[ \frac{(\pi kT/E_{ch})}{\sin(\pi kT/E_{ch})} \right]. \quad (1.2.6)$$

The disordered structure reduces the free carrier mobility within the extended band (compared to crystalline structures) and  $\mu$  on the order of  $10 \text{ cm}^2/\text{Vs}$  are expected [17]. However, because of the tendency of the tail states to trap carriers, the charge transport in amorphous semiconductors is sometimes presented as a trapping-and-release type of conduction mechanism. These trapping and release events effectively reduce the drift velocity, relative to pure band transport, and the transport is described by a trap-controlled mobility.

In cases when the energetic disorder is large or the temperatures are low, direct "trap-to-trap" transport between localized states starts to dominate the current conduction [16]. This conduction mechanism is referred to as hopping transport, consisting of a combination of thermally activated processes and tun-

neling between localized states. The electron hopping rate from site  $i$  to  $j$ , separated by a distance  $r_{ij}$ , is commonly described by the Miller-Abraham rate [16]

$$\nu_{ij} = \nu_0 \exp(-2\gamma r_{ij}) \times \begin{cases} \exp\left(-\frac{\Delta E_{ij}}{kT}\right) & \text{if } \Delta E_{ij} \geq 0, \\ 1 & \text{if } \Delta E_{ij} < 0, \end{cases} \quad (1.2.7)$$

where  $\gamma$  is the inverse localization radius,  $\Delta E_{ij}$  is the energy difference between sites  $i$  and  $j$ , and  $\nu_0$  is the attempt-to-escape frequency.

### 1.2.2 Organic semiconductors

Organic semiconductors are based on molecules and molecular segments that are bound by alternating single and double bonds, so called  $\pi$ -conjugated bonds, along which electrons are delocalized. The ground state of the delocalized electrons is referred to as the highest occupied molecular orbital (HOMO) with the first excited state being the lowest unoccupied molecular orbital (LUMO). A schematic picture is shown in Figure 1.3. If the overlap (interaction) between the frontier orbitals of nearest-neighbor segments is strong, narrow bands of extended states will be formed; the band of HOMO levels corresponds to the valence band, whereas the LUMO band corresponds to the conduction band [18]. Provided that the band width  $W$  is larger than the energetic uncertainty of the carriers, the carrier conduction is band-like with a mobility given by  $\mu \approx (q\tau_{sc}/kT) \langle v^2 \rangle$ , where  $\sqrt{\langle v^2 \rangle} \sim s/\tau_{sc}$  and  $s$  is the mean free path; this is only valid for  $\mu > qa^2W/\hbar kT$  ( $\sim 1 \text{ cm}^2/\text{Vs}$ ), where  $a$  is the lattice constant [17, 19].

In films of semiconducting polymers and small molecules that are used for diode and solar cell applications, however, energetic disorder effects dominate over nearest-neighbor interactions. Consequently, the conjugation in these polymers is typically only maintained to one or a few repeat units and the interaction (between segments) is mediated by weak van der Waals forces. Because of the weak electronic interaction between separate conjugated segments, the current



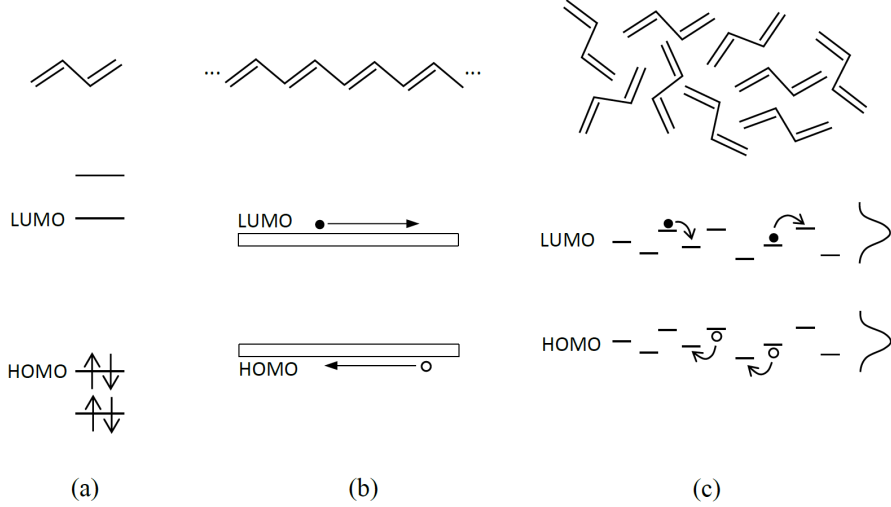


Figure 1.3: Schematic picture of the electronic structures in organic semiconductors. (a) The energy levels of a conjugated segment. (b) Along the conjugated chain, the (intra-chain) transport is ideally taking place by band-like transport. (c) In disordered organic semiconductors, the (inter-chain) transport takes place by hopping of charge carriers between separate conjugated segments, bound to each other by weak van der Waals forces.

conduction is subsequently limited by hopping of charge carriers between the conjugated units (Figure 1.3(c)). The energetic variation of the LUMO and HOMO levels (between conjugated segments) is often approximated by a Gaussian distribution with the energetic variance  $\sigma$ ,

$$g(E) = \frac{N_0}{\sqrt{2\pi\sigma^2}} \exp \left[ -\frac{(E - E_0)^2}{2\sigma^2} \right], \quad (1.2.8)$$

where  $N_0$  is the total density of sites (conjugated segments) and  $E_0$  is the mean value of the corresponding energy levels. The electron density for this type of distribution of LUMO levels can in the non-degenerate (low-carrier) limit be

expressed as [20]

$$n = N_0 \exp \left( \frac{E_F - E_{0,LUMO} + \frac{\sigma^2}{2kT}}{kT} \right) = N_0 \exp \left( \frac{E_F - E_c}{kT} \right), \quad (1.2.9)$$

where  $E_c = E_{0,LUMO} - \sigma^2/2kT$  may be interpreted as an effective conduction level edge.

The hopping rate in disordered organic semiconductors is commonly described by the Miller-Abraham rate (Eq. (1.2.7)) [16, 18]. The Miller-Abrahams hopping rate, however, neglects polaronic effects. Adding/removing an electron to/from a molecule or a conjugated segment will generally also induce an electrostatic reorganization of the surrounding energetic environment, accompanied by a relaxation of the energy levels (of the occupied unit) into the gap. To account for the polaronic relaxation, the hopping rate can be characterized as a Marcus charge transfer process:

$$\nu_{ij} = \frac{|I_{ij}|^2}{\hbar} \sqrt{\frac{\pi}{E_r kT}} \exp \left( -\frac{[\Delta E_{ij} + E_r]^2}{4E_r kT} \right), \quad (1.2.10)$$

where  $E_r$  is the reorganization energy and  $I_{ij}$  describes the electronic coupling between the sites.

### 1.3 The charge transport equations

From a macroscopic perspective, the electrical current in semiconductor devices with planar structures (Figure 1.1(a)) can quite generally be characterized by the following set of basic equations [15, 21–23]. In accordance with Maxwell's fundamental equations, we have the total (time-dependent) current equation

$$j(t) = J_c(x, t) + \varepsilon \varepsilon_0 \frac{\partial F(x, t)}{\partial t}, \quad (1.3.1)$$

where  $J_c(x, t) = J_p(x, t) + J_n(x, t)$  is the conduction current density composed of the sum of the hole and electron current density, the charge carrier continuity equations

$$\frac{\partial n}{\partial t} = \frac{1}{q} \frac{dJ_n}{dx} + \mathcal{R}_n, \quad (1.3.2)$$

$$\frac{\partial p}{\partial t} = -\frac{1}{q} \frac{dJ_p}{dx} + \mathcal{R}_p, \quad (1.3.3)$$

where  $\mathcal{R}_n$  and  $\mathcal{R}_p$  are the respective net generation-recombination rates for electrons and holes, and the Poisson equation

$$\frac{dF}{dx} = \frac{1}{q} \frac{d^2 E_{c,v}}{dx^2} = \frac{\rho_{sc}}{\varepsilon \varepsilon_0} \quad (1.3.4)$$

that relates the electric field  $F$  to the net charge density  $\rho_{sc}$  within the semiconductor layer, with  $\varepsilon \varepsilon_0$  being the permittivity of the layer. Note that  $dj(t)/dx = 0$  and the total current is independent of  $x$ .

### 1.3.1 The drift-diffusion equations

The individual electron and hole current densities are given by the drift-diffusion equations:

$$J_n = \mu_n n \frac{dE_c}{dx} + q D_n \frac{dn}{dx} = \mu_n n \frac{dE_{Fn}}{dx}, \quad (1.3.5)$$

$$J_p = \mu_p p \frac{dE_v}{dx} - q D_p \frac{dp}{dx} = \mu_p p \frac{dE_{Fp}}{dx}, \quad (1.3.6)$$

where  $E_{Fn}$  is the electron quasi-Fermi level,  $E_{Fp}$  is the hole quasi-Fermi level, whereas  $D_n$  and  $D_p$  is the diffusion coefficient for electrons and holes, respectively. The drift-diffusion equations (in some cases also referred to as the Nernst-Planck equations) are very general and have been used to describe the charge transport in a wide variety of systems, including the transport of electrons and holes in semiconductor devices and the transport of ions in liquids and cell membranes [15, 21, 24–26]. The drift-diffusion equations have also been successfully

applied to organic devices [17], including diodes and solar cells [22, 27–31].

The mobilities and the diffusion coefficients are related via the generalized Einstein relation,

$$D_{n(p)} = \frac{\mu_{n(p)} kT}{q} \eta_{n(p)}, \quad (1.3.7)$$

where  $\eta_{n(p)}$  is a dimensionless quantity accounting for the DOS occupation for electrons (holes) [32]; for electrons:  $\eta_n = [\partial(E_{Fn} - E_c)/\partial n] n/kT$ . In non-degenerate systems, the diffusion coefficient obeys the classical Einstein relation,  $\eta_n = \eta_p = 1$ . Conversely, when DOS filling effects become important (degenerate limit), the generalized Einstein relation is typically used instead. However, it has been pointed out that the definition of  $\eta_n$  and  $\eta_p$  in disordered materials also depends on the definitions of free carriers and the mobility [33]. Under low-voltage operation, the classical Einstein relation may be considered a good approximation when describing the electrical behavior in organic diode devices [34]. Unless otherwise stated, the classical Einstein relation is assumed in this work as well.

For the device simulations, the above equations [Eqs. (1.3.1) to (1.3.7)] are solved numerically using the well-established discretization and iteration scheme by Scharfetter and Gummel [35, 36], as outlined in Refs. [23] and [37] (see also Ref. [28]). Under non-degenerate conditions ( $\eta_n = \eta_p = 1$ ), the general solution of Eq. (1.3.5) and Eq. (1.3.6) for the electron and hole density, respectively, takes the form

$$n = N_c \exp\left(\frac{E_{Fn} - E_c}{kT}\right), \quad (1.3.8)$$

$$p = N_v \exp\left(\frac{E_v - E_{Fp}}{kT}\right), \quad (1.3.9)$$

where  $E_c$  is the effective conduction level edge,  $N_c$  is the (effective) density of electron transport states,  $E_v$  is the effective valence level edge, and  $N_v$  is the (effective) density of hole transport states. In case of a Gaussian distribution (Eq. (1.2.8)), we have  $E_c = E_{0,LUMO} - \sigma_n^2/2kT$  and  $E_v = E_{0,HOMO} + \sigma_p^2/2kT$ , where

$\sigma_n$  and  $\sigma_p$  are the disorder parameters of the LUMO and HOMO distribution, respectively.

### 1.3.2 Drift-diffusion and mobility from the viewpoint of hopping transport

In disordered semiconductors where the carrier transport is governed by hopping, the mobilities and diffusion coefficients are to be considered effective quantities [22]. Figure 1.4 shows a schematic picture of the hopping transport. The electron current between adjacent planes  $i$  and  $j$ , separated by a typical hopping distance  $a$ , can be expressed as

$$J_n = qN_j a W_{ji} - qN_i a W_{ij} \equiv q\mu_n F \frac{N_i + N_j}{2} + qD_n \frac{N_j - N_i}{a}, \quad (1.3.10)$$

where  $W_{ij}$  is the hopping rate (averaged over the carrier density) from  $i$  to  $j$ , and  $N_i$  and  $N_j$  are the average electron concentrations within the respective planes [38]. Here, the mobility and the diffusion coefficient:

$$\mu_n = \frac{a [W_{ji} - W_{ij}]}{F}, \quad (1.3.11)$$

$$D_n = \frac{a^2}{2} [W_{ij} + W_{ji}], \quad (1.3.12)$$

respectively. At low electric field strengths ( $q|F|a < kT$ ) in particular is Eq. (1.3.10) well approximated by Eq. (1.3.5), justifying the use of drift-diffusion in this limit. The mobilities associated with hopping transport are generally very low ( $\mu \ll 1 \text{ cm}^2/\text{Vs}$ ), typical values being on the order of  $10^{-4} \text{ cm}^2/\text{Vs}$ .

When the energetic disorder is small, the energy difference between two consecutive sites under an applied electric field is given by  $q|F|a$  (see Figure 1.4). For a hopping rate given by Eq. (1.2.7), dominated by hops between nearest neighbors, the drift velocity can then be approximated as  $v_{dr} = v_{sat}[1 - \exp(-q|F|a/kT)]$ , where  $v_{sat} = a\nu_0 \exp(-2\gamma a)$ . The mobility at low electric

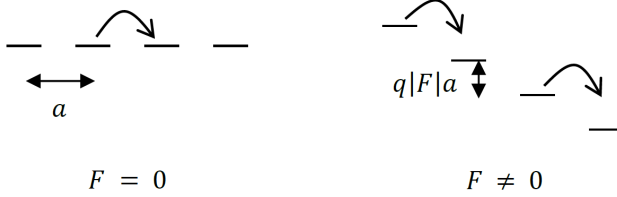


Figure 1.4: Schematic energy level diagram illustrating hopping transport under the influence of an electric field  $F$ . The hopping distance between two sites is given by  $a$ .

field strengths  $|F| \ll 2kT/qa$  is subsequently given by [39]

$$\mu = \frac{v_{dr}}{F} = \frac{qa^2\nu_0}{kT} \exp(-2\gamma a), \quad (1.3.13)$$

for small  $\sigma$ . An analogous expression for the mobility can be found in case of a Marcus charge transfer type hopping rate.<sup>1</sup>

The effect of a Gaussian distribution of energy levels on the mobility in a hopping system was investigated by Bässler using Monte Carlo simulations [40]. The mobility was found to follow a temperature and field dependence of the form  $\ln \mu \propto -4\sigma^2/9(kT)^2 + b(T)\sqrt{F}$  in the limit of low carrier concentrations, where the temperature-dependent coefficient  $b(T)$  also depends on the energetic variance  $\sigma$ . This model is typically referred to as the Gaussian disorder model. A wide variety of extensions and alternatives to this model have been suggested, and in general the mobility also depends on the carrier density [16, 18, 31]. An extended Gaussian disorder model (EGDM), taking into account the DOS

<sup>1</sup>An analogous situation applies for hopping transport described by Marcus charge transfer Eq. (1.2.10); the mobility is obtained as

$$\mu_n = \frac{qa^2}{kT} \frac{|I_{ij}|^2}{\hbar} \sqrt{\frac{\pi}{E_r kT}} \exp\left(-\frac{E_r}{4kT}\right) \left\{ \frac{\sinh(qFa/2kT)}{(qFa/2kT)} \exp\left(-\frac{|qFa|^2}{4E_r kT}\right) \right\},$$

where the factor within the curly brackets  $\{\dots\} \rightarrow 1$  at low electric field strengths, when  $[qFa/\sqrt{6kT}]^2 \ll 1$ .

occupation  $c$  was presented by Pasveer *et al.* [41]. In the EGDM framework, the zero-field mobility in the low carrier density limit ( $c \rightarrow 0$ ) is well approximated by

$$\mu_0(T) = \frac{qa^2\nu_0}{\sigma} c_1 \exp\left(-c_2 \left[\frac{\sigma}{kT}\right]^2\right), \quad (1.3.14)$$

where  $c_1 = 1.8 \times 10^{-9}$  and  $c_2 = 0.42$  in case of uncorrelated Gaussian disorder. Here, the prefactor  $c_1 \sim \exp(-2\gamma a)$  describes the wave function overlap between the states. At large electric field strengths  $|F| > \sigma/qa$  and/or high carrier densities, the mobility is enhanced as  $\mu(T, F, c) = \mu_0(T) f_1(F, T) f_2(c, T)$  where  $f_1(F, T)$  and  $f_2(c, T)$  are the enhancement factors due to non-zero electric field and carrier density, respectively [41]. The onset for the carrier density dependence ( $f_2(c, T) > 1$ ) occurs when the energetic difference between the DOS center and the carrier quasi-Fermi level becomes smaller than  $\sigma^2/kT$  [31]. In the limit of very high electric field strengths, however, all jumps are "downhill" and the drift velocity saturates to  $v_{sat} = a\nu_0 \exp(-2\gamma a)$ , seen as a  $\mu \propto 1/F$ .

The Gaussian disorder model for the mobility neglects the initial relaxation of the carriers. Electrons initially generated within an otherwise empty DOS will relax downwards in energy. During the relaxation process, the carrier mobility decreases with time until an equilibrium condition is established around the electron mean energy  $\sigma^2/kT$  below the DOS center (into the gap) [18]. The initial relaxation is important during non-equilibrium photogeneration conditions, where charges do not have time to relax before leaving the device [42, 43]. Under steady-state conditions, this would be seen as an effectively higher device mobility that also depends on the active layer thickness [44].

### 1.3.3 Generation and recombination processes in the bulk

Apart from injection from the contacts, charge carriers can also be generated by photoinduced and thermal excitations in the bulk. The reverse process of charge-carrier generation is recombination. The excess energy created during this type

of annihilation process can be released by radiative emission of photons (direct recombination), and/or non-radiative emission via phonons (indirect). The net generation-recombination rate of free electrons and holes is given by

$$\mathcal{R}_n = G_L - R_b - R_n^- + G_n^- - R_n^+ + G_n^+, \quad (1.3.15a)$$

$$\mathcal{R}_p = G_L - R_b - R_p^- + G_p^- - R_p^+ + G_p^+, \quad (1.3.15b)$$

respectively, where  $G_L$  is the photogeneration rate of free electron-hole pairs and  $R_b$  is the net recombination rate for bimolecular recombination. Moreover,  $R_n^-$  ( $R_p^+$ ) is the capture rate of electrons (holes) into traps,  $G_n^-$  ( $G_p^+$ ) is the escape rate of electrons (holes) from the traps (back into the transport levels),  $G_p^-$  ( $G_n^+$ ) is the trap-assisted generation rate of free holes (electrons), and  $R_p^-$  ( $R_n^+$ ) is the recombination rate between free holes (electrons) with trapped electrons (holes). In this context, traps are defined as localized states within the gap that do not participate in the charge transport process. By detailed balance, Eq. (1.3.15) generally takes the form  $\mathcal{R}_n = \mathcal{R}_p = G_L - R$ , where

$$R = \beta_R [np - n_i^2] \quad (1.3.16)$$

is the net bulk recombination rate; here,  $n_i^2 = N_c N_v \exp(-E_g/kT)$ , where  $E_g = E_c - E_v$  is the effective electrical bandgap. The recombination coefficient  $\beta_R = \beta_R(n, p)$ , which in general also depends on the carrier densities, is determined by the dominating recombination mechanism.

### Bimolecular recombination

The direct recombination between a free electron and a free hole is a bimolecular process. The net bimolecular recombination rate between electrons and holes is given by

$$R_b = \beta [np - n_i^2], \quad (1.3.17)$$



where  $\beta$  is the associated bimolecular recombination coefficient. In Eq. (1.3.17), the term  $\beta n_i^2$  is the recombination rate at thermal equilibrium and equals the thermal generation rate of free carriers. In homogenous low-mobility materials, the probability for a free electron and a free hole to find each other is determined by the drift time in their mutual Coulomb potential. The requirements for this type of encounter mechanism to occur is that the carrier mean free path (or hopping distance)  $a$  is much smaller than the Coulomb capture radius  $r_c$ , where

$$r_c = \frac{q^2}{4\pi\epsilon\epsilon_0 kT}. \quad (1.3.18)$$

If the recombination is encounter-limited, the bimolecular recombination process is then characterized by Langevin recombination [45], with the bimolecular recombination coefficient given by<sup>2</sup>

$$\beta_L = \frac{q}{\epsilon\epsilon_0} (\mu_n + \mu_p), \quad (1.3.19)$$

being only dependent on the mobilities and the dielectric properties of the medium.

In organic BHJ solar cells, however, electrons and holes are restricted to different phases and the recombination mostly occur at organic interfaces; see

---

<sup>2</sup>The drift velocity of the  $j$ :th positively-charged hole, relative to a negatively-charged electron, is given by

$$\vec{v}_j = (\mu_n + \mu_p) \left[ \vec{F} - \frac{q\vec{r}_j}{4\pi\epsilon\epsilon_0 |\vec{r}_j|^3} \right],$$

where  $\vec{r}_j$  is the distance vector between the two carriers and the external field  $\vec{F}$  is constant. The volume element spanned, in time  $dt$ , is given by  $\vec{v}_j dt \cdot d\vec{\sigma}_j$ , where  $d\vec{\sigma}_j$  is the normal area element. Assuming that the number  $N_e$  of electrons is larger than  $N_h$  of holes, the largest possible number of volume elements is then  $N_e$ . The number of recombination events (*i.e.* the number of elements that contain a hole) is then equal to the product between the total volume spanned and the hole density  $p$  [45]:

$$dN_h = dN_e = p \, dt \sum \oint \vec{v}_j \cdot d\vec{\sigma}_j = -pdt \sum \frac{q(\mu_n + \mu_p)}{\epsilon\epsilon_0} = -\beta_L N_e p \, dt,$$

where Gauss theorem was used. Hence, in terms of carrier densities:  $dp/dt = dn/dt = -\beta_L np$ .

Figure 1.5. In effect, this means that the bimolecular coefficient  $\beta$  for charge encounter is reduced relative to the Langevin coefficient (Eq. (1.3.19)) [46, 47]. Koster *et al.* suggested that the recombination rate under these circumstances is limited by the mobility of the slower carrier, so that  $\beta = q \min(\mu_n, \mu_p) / \varepsilon \varepsilon_0$  [48]. A recent theoretical study found that the impact of the slower mobility indeed increases as the phase domains become larger, whereas the Langevin model is approached in the limit of small phase separations ( $< 5$  nm) [49]. At intermediate phase separations ( $\sim 10$ -35 nm) the mobility dependence of the recombination coefficient was, on the other hand, better approximated by the geometric mean between the electron and hole mobilities ( $\beta \propto \sqrt{\mu_n \mu_p}$ ) [46, 49]. It should be noted, however, that the charge-carrier recombination in most materials is not encounter-limited and generally takes place via intermediate states.

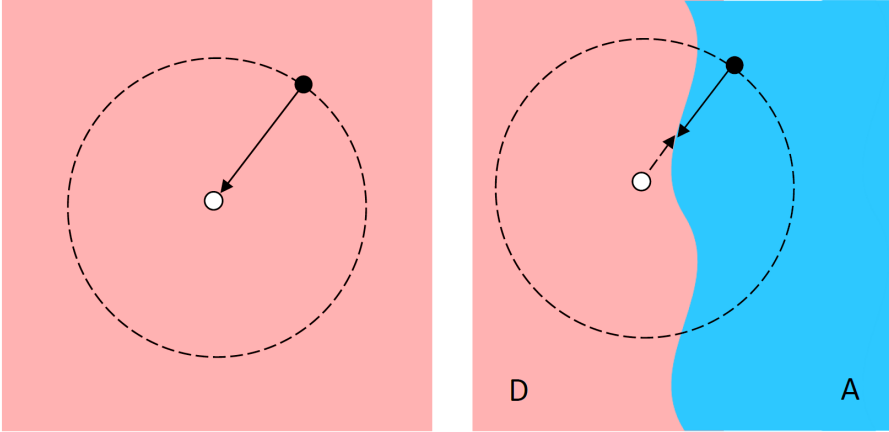


Figure 1.5: Encounter-limited bimolecular recombination between electrons and holes in low-mobility materials. In homogenous materials (to the left) the recombination coefficient for charge encounter is represented by Langevin recombination, dominated by the mobility of the faster carrier. The situation is different in blend structures (to the right), where electrons and holes are restricted to acceptor (A) and donor (D) phases, respectively. In this case, the recombination coefficient for charge encounter is reduced (relative to Langevin) and the impact of the slower mobility enhanced.

## Recombination via intermediate states

The charge-carrier recombination mechanism in the bulk is, in general, a multi-step process [50]. Once an electron and a hole has encountered each other they may combine into a charge-encounter complex, also referred to as a charge-transfer (CT) state [22]. The complex then either recombines with a rate-coefficient  $k_f$  to the ground state or dissociates back into free carriers with a rate-coefficient  $k_d$  [28, 51, 52]. A simplified schematic picture of this process is shown in Figure 1.6. Accordingly, the density of charge-encounter complexes  $X$  is related to the generation and recombination rates of free carriers by

$$\frac{\partial X}{\partial t} = G_0 + R_b - k_d X - k_f X, \quad (1.3.20)$$

$$\mathcal{R}_{n,p} = G_L - R = G^* + k_d X - R_b, \quad (1.3.21)$$

where  $G_0$  is the generation rate of (relaxed) CT states from excitons. Here, we also included the rate  $G^*$  for free carriers to be generated "directly" from (hot) excitons (possibly via highly excited CT states) [53]. At steady-state ( $\partial X/\partial t = 0$ ), the net generation and recombination rates of free carriers may then be expressed as  $G_L = G^* + P G_0$  and  $R = (1 - P) R_b$ , with

$$P = \frac{k_d}{k_f + k_d} \quad (1.3.22)$$

being the probability for the charge-transfer state to dissociate into free charge carriers. Taking this effect into account, the reduced recombination coefficient between free carriers becomes

$$\beta_R = (1 - P) \beta, \quad (1.3.23)$$

where  $\beta$  is the bimolecular rate coefficient for electrons and holes to find each other in space to form a charge-transfer state, while the factor  $(1 - P)$  determines the probability for the complex to ultimately recombine (*i.e.* make a transition to the ground state) once it has been formed.

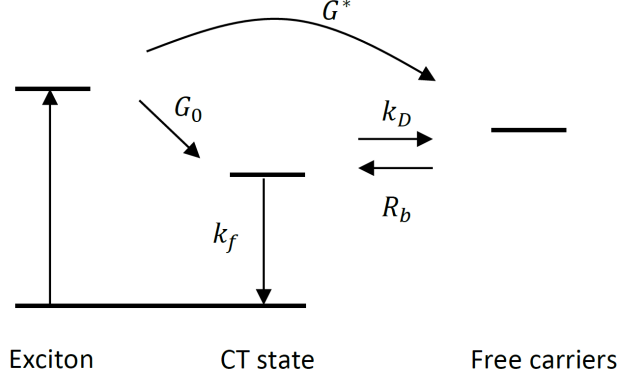


Figure 1.6: A simplified energetic structure diagram representing generation and recombination of free carriers taking place via intermediate charge transfer (CT) states.

The dissociation probability  $P$  has traditionally been characterized as an electric-field-enhanced process in accordance with the Onsager-Braun model [54, 55]. This model, which assumes a homogenous (Langevin) material, has been well reproduced in organic single-layers. At  $F = 0$ , the dissociation coefficient takes the form  $k_d = \beta_L N^* \exp(-\Delta E_{CT}/kT)$ ,<sup>3</sup> where  $\Delta E_{CT}$  is the binding energy of the electron-hole pair. For  $k_d \gg k_f$ , one then finds  $\beta_R = \beta_0 \exp(\Delta E_{CT}/kT)$ , where  $\beta_0$  depends on  $k_f$  and  $N^*$ . In a blend, however, also the relative field orientation and the energetic landscape at the D-A interface need to be taken into account. It has also been suggested that gradients in the density of available states ( $N^*$ ) at the interfaces might play a role [56, 57], with the resulting additional gradient in free energy constituting an entropic driving force for the dissociation [11]. It should be stressed that the complete recombination mechanism in BHJ solar cells is still under debate [22], and experimentally

<sup>3</sup>In accordance with the Onsager-Braun model, the dissociation rate-coefficient reads [55]

$$k_d(0) = \beta_L N^* \exp\left(-\frac{\Delta E_B}{kT}\right), \quad \frac{k_d(F)}{k_d(0)} = \frac{J_1(\sqrt{-8b})}{\sqrt{-2b}} = 1 + b + \frac{b^2}{3} + \frac{b^3}{18} + \dots,$$

where  $\Delta E_{CT} = q^2/4\pi\epsilon\epsilon_0 r_0$ ,  $N^* = 3/4\pi r_0^3$ ,  $b = q|F|r_c/2kT$ , and  $r_0$  is the initial electron-hole separation.

obtained  $\beta_R = \zeta\beta_L$  generally exhibit  $\zeta$  ranging between 1 to  $10^{-3}$  [50, 58–60]. Recent work by Benduhn *et al.* on a large number of organic blend structures suggests that the recombination coefficient  $k_f$  for CT states, and therefore also the overall bimolecular recombination coefficient, is dominated by intrinsic non-radiative processes mediated by intramolecular carbon-carbon vibrations [61].

### Trap-assisted recombination of carriers via traps

The recombination of free carriers can also take place through traps within the bandgap. Electron traps are traps that are negatively-charged when occupied by an electron and neutral when empty (occupied by a hole), referred to as acceptor-like. Conversely, hole traps are donor-like, being neutral when occupied with an electron and positively-charged when occupied by a hole (*i.e.* when empty). If the recombination predominately occurs via acceptor-like traps, the net recombination rate between electrons and holes becomes [21, 62, 63]

$$R_{SRH}^- = R_n^- - G_n^- = R_p^- - G_p^- = \beta_{SRH}^- [np - n_i^2], \quad (1.3.24)$$

in accordance with Shockley-Read-Hall (SRH) statistics. Here, the effective coefficient  $\beta_{SRH}^-$  depends on the carrier density as

$$\beta_{SRH}^- = \sum_j \frac{C_n C_p N_{tj}^-}{C_n (n + n_{1,j}) + C_p (p + p_{1,j})}, \quad (1.3.25)$$

where  $N_{tj}^-$  is the trap density at energy  $E_{tj}^-$ ,  $n_{1,j} = N_c \exp([E_{tj}^- - E_c]/kT)$ ,  $p_{1,j} = N_v \exp([E_v - E_{tj}^-]/kT)$ ,  $C_n$  is the capture (trapping) coefficient of electrons from the conduction level into traps, and  $C_p$  is the recombination coefficient between trapped electrons and free holes. In accordance with Langevin recombination, one expects  $C_p = q\mu_p/\varepsilon\varepsilon_0$  [64]. When this type of SRH recombination mechanism is dominating, we have  $\beta_R = \beta_{SRH}^-$ . Analogous expressions are valid for the recombination taking place via donor-like hole traps:  $R_{SRH}^+ = \beta_{SRH}^+ [np - n_i^2]$ .

Figure 1.7(a) shows a schematic picture of trap-assisted recombination taking place via acceptor-like traps. For monoenergetic traps of density  $N_t$  at the energy level  $E_t$ , the following scenarios may arise. In case of deep midgap trap levels ( $E_{Fn} > E_t > E_{Fp}$ ), a situation where the traps are predominantly acting as recombination centers prevails and the recombination rate is monomolecular,  $R_{SRH}^- \propto n$  (since  $\beta_{SRH}^- \approx C_n C_p N_t / [C_n + C_p] n$  for  $p \approx n$ ). Conversely, if the traps are shallow ( $E_t < E_{Fn}$ ), corresponding to  $n_1 \gg n, p$ , the trap-assisted recombination rate is effectively bimolecular with  $\beta_{SRH}^- = C_p N_t / n_1$ . Under these circumstances, the effect of the traps is mainly to capture and release electrons, effectively slowing down the transport of electrons in the conduction level.

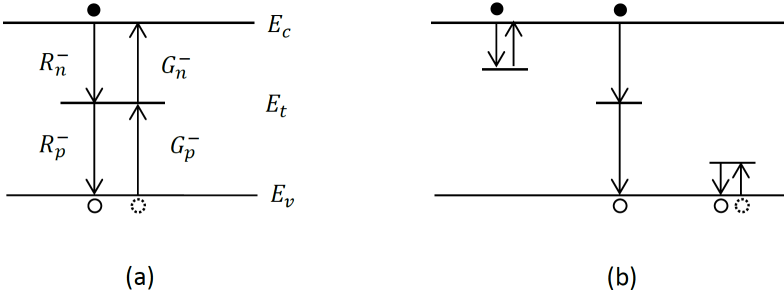


Figure 1.7: (a) Schematic energy level diagram illustrating trap-assisted recombination via acceptor-like traps within the gap. In (b), three different types of acceptor-like traps are depicted: shallow traps situated close to the conduction level, deep traps within the gap, and levels that are deep enough to directly accept an electron from the valence level (*i.e.*  $p$ -dopant levels).

#### 1.3.4 Space charge

In the presence of electrode contacts, a net charge can be established within the active layer. The charge may originate from photogeneration, doping or injection from the contacts. However, on a global scale charge neutrality applies.

This means that the net charge per unit area inside the active layer, defined by

$$Q_s = \int_0^d \rho_{sc}(x) dx, \quad (1.3.26)$$

is exactly balanced by an equal but opposite charge stored on the electrodes, where  $d$  is the thickness of the active layer. From Eq. (1.3.4), one obtains:  $Q_{an} + Q_{cat} - Q_s = 0$ , where  $Q_{an} = \varepsilon \varepsilon_0 F(0)$  and  $Q_{cat} = -\varepsilon \varepsilon_0 F(d)$  is the charge per unit area (immediately outside the surface) in the anode and cathode, respectively. In this respect, the device behaves as a parallel plate capacitor with the geometric capacitance (per unit area)  $C_{geo} = \varepsilon \varepsilon_0 / d$ .

Apart from free charge carriers, also trapped charges contribute to the total space charge within the layer, and thus affect the local electric field in accordance with Eq. (1.3.4). The net space-charge density inside the active layer is given by

$$\rho_{sc} = q[p - n] + q \sum_j [p_{tj} - n_{tj}], \quad (1.3.27)$$

where  $n_{tj}$  and  $p_{tj}$  is the density of trapped electrons and holes, respectively, at the energy level  $E_{tj}$ . The trap occupation is commonly described by Shockley-Hall-Read statistics [21]. At steady-state conditions, the density of trapped electrons in acceptor-like trap levels is<sup>4</sup>

$$n_{tj} = \frac{N_{tj}^- (C_n n + C_p p_{1j})}{C_n (n + n_{1j}) + C_p (p + p_{1j})}. \quad (1.3.28)$$

In the absence of holes ( $p = p_{1j} = 0$ ), the trapped electron occupation is well approximated by Fermi-Dirac statistics, with the quasi-Fermi level being the

---

<sup>4</sup>The kinetics of the density of electrons at a monoenergetic acceptor-type trap level can be described by

$$\frac{dn_t}{dt} = R_n^- - G_n^- + G_p^- - R_p^- = C_n n [N_t^- - n_t] - C_n' N_c n_t + C_p' N_v [N_t^- - n_t] - C_p n_t p,$$

where  $n \ll N_c$  and  $p \ll N_v$  have been assumed. Here,  $C_p' = C_p \exp([E_t - E_v]/kT)$  and  $C_n' = C_n \exp([E_c - E_t]/kT)$ , noting that Fermi-Dirac statistics must apply at thermal equilibrium.

same for trapped and mobile electrons. A schematic picture of acceptor-like trap levels with different trap depths is shown in Figure 1.7(b).

A situation of special interest arise when acceptor-like impurities, with electron-accepting energy levels (*e.g.* the LUMO of the impurity molecule) that are close to (or beyond) the valence level, are introduced into the semiconductor layer. In this case ( $p_1 \gg n, n_1$ ), the acceptor level accepts an electron directly from the valence level, creating a free hole in the active layer. This is a mechanism responsible for *p*-type doping [65]. The density of electrons occupying the acceptor level is given by  $n_t \approx N_t^- / (1 + p/p_1) = N_p$ , being equal to the density of ionized dopants  $N_p$  [66]. The net space-charge density is then  $\rho_{sc} = q [p(x) - N_p]$ . In the absence of an electric field, it then follows from Eq. (1.3.4) that  $p = N_p$ . An analogous situation applies for donor-like impurities, resulting in *n*-type doping.

## 1.4 The motivation and scope

In thin-film diodes based on organic semiconductors, the conductivity of the active layer is in general limiting the current, in contrast to conventional *p-n* junctions. In order to describe the device physics of organic solar cells, a deeper physical understanding of the processes taking place is needed. The charge collection in organic solar cells is generally analyzed from the perspective that charge transport competes with bulk recombination. However, these models generally assume surface recombination at the electrodes to be negligible and do not account for contact effects. The charge collection in these devices are also sensitive to unintentional doping giving rise to doping-induced space-charge regions within the active layer, generally degrading the performance. To be able to further improve and optimize the charge collection in these devices, it is essential to be able to identify and understand these loss mechanisms. The aim of this thesis is to clarify the charge collection in thin-film devices based on low-mobility semiconductors. In particular the interplay between charge transport, recombination and extraction at the contacts is investigated by means of analytical derivations and numerical simulations. Furthermore, analytical methods to



distinguish and quantify relevant parameters related to these loss mechanisms are presented. Special emphasis is devoted to the role of the contacts and how these impact charge extraction in organic solar cells, based on optically thin active layers.

In Chapter 2, we start by reviewing and discussing the underlying theory regarding the charge transport processes taking place at the contacts and within devices. This discussion follows the established general current theory for transport processes at metal-semiconductor contacts, however, from the perspective of thin-film devices based on low-mobility semiconductors thus providing new insights into the charge-carrier collection in these devices.

In Chapter 3, we begin by briefly reviewing the basic theory behind the charge extraction by linearly increasing voltage pulse (CELIV) method, which has frequently been used to extract the charge-carrier mobility in organic solar cells. Afterwards, the theory of CELIV is extended to account for effects of the contacts, these being of particular importance in thin-film devices. Apart from providing corrections to the mobility determination, we also show how the extended theory can be used to quantify other parameters such as the built-in voltage, the doping concentration, and the surface recombination velocity at the contacts, which are relevant for understanding charge collection in organic semiconductor devices.

In Chapter 4, the charge collection in organic solar cells is discussed. The competition between charge-carrier extraction and recombination, the impact of surface recombination and charge-carrier selectivity at the contacts, and the influence of space-charge regions within the active layer is investigated from a theoretical point of view. Based on the results, new tools and methods to distinguish, identify and quantify loss mechanisms related to charge-carrier collection in organic solar cells are presented. To conclude, some of the developed analytical tools and methods are experimentally demonstrated on inverted P3HT:PCBM BHJ solar cells employing  $\text{TiO}_2$  as the electron-selective electrode interlayer.

## CHAPTER 2

# Current injection and collection in thin-film devices

In order to collect charges in thin-film devices, contacts between the semiconductor layer and the electrodes are needed. Different applications generally require different contact properties. If the current in the dark is solely conducted by holes in the active layer, the transport is unipolar and the device is referred to as hole-only. A hole-only diode is realized by choosing the properties of the contacts in such a way that the anode is hole-injecting, whereas the cathode is non-injecting (for both carrier types). In forward bias, holes are then injected from the anode into the active layer, transported through the semiconductor and eventually collected at the cathode. Reversely, an electron-only diode is realized by instead choosing an electron-injecting cathode and a non-injecting anode. If the anode is hole-injecting anode and the cathode electron-injecting, a bipolar (or double-carrier) device is obtained. In this section, the basic theory behind current injection and collection in sandwich-type thin-film devices based on low-mobility semiconductors is discussed.

## 2.1 Sandwich-type thin-film structures

The sandwich-type device structure generally has an electrode-semiconductor-electrode configuration with electrodes (or conducting layers) of different work functions. The work function is defined by the energy difference between the Fermi level and the vacuum level. The electrode with the larger work function constitutes the anode, while the electrode with the lower work function is the cathode. At thermal equilibrium, the Fermi levels are the same and constant throughout the device. The effect of applying an external voltage  $V$  to the anode, with respect to the cathode, is to displace the anode Fermi level relative to the cathode Fermi level,

$$qV = E_{F,cat} - E_{F,an}. \quad (2.1.1)$$

This will disrupt the thermal equilibrium condition, often resulting in a flow of a net current. The applied voltage is related to the local electric field  $F$  inside the active layer via

$$V - V_{bi} = \int_0^d F dx, \quad (2.1.2)$$

where  $V_{bi}$  is the built-in voltage across the active layer and given by the difference between the electrode work functions:

$$V_{bi,0} \equiv \frac{1}{q} [\Phi_{an} - \Phi_{cat}], \quad (2.1.3)$$

where  $\Phi_{an}$  and  $\Phi_{cat}$  is the work function at the anode and the cathode contact, respectively.

### 2.1.1 Metal-semiconductor interfaces

When a contact between a semiconductor and an electrode is formed, some transfer of charge will always be present. Consider a contact between a metal

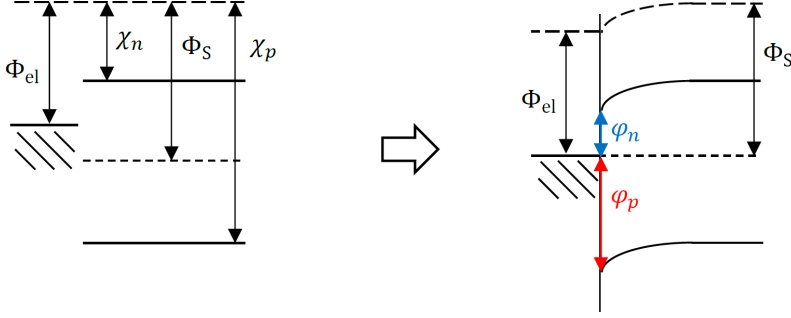


Figure 2.1: Schematic energy level diagram of an electrode-semiconductor system before contact and at thermal equilibrium after contact. To establish equilibrium, charge transfer between the electrode and the semiconductor occurs, to equilibrate the Fermi level in the semiconductor. If this net charge transfer is large enough, energy-level bending will occur at the contact.

electrode and a semiconductor (of infinite layer thickness). The work function of the metal is given by  $\Phi_{el}$ , while  $\Phi_S$  is the work function of the semiconductor. For an intrinsic semiconductor, the Fermi level is originally close to the middle of the bandgap. The energy difference between the valence level edge and the Fermi level at the metal will constitute a barrier for hole injection from the metal into the semiconductor. The hole-injection barrier is given by

$$\varphi_{p,el} = \chi_p - \Phi_{el}, \quad (2.1.4)$$

where  $\chi_p$  corresponds to the ionization potential, describing the difference between the valence level edge and the vacuum level. A corresponding injection barrier can be defined for electrons,

$$\varphi_{n,el} = \Phi_{el} - \chi_n, \quad (2.1.5)$$

given by the difference between the Fermi level at the metal electrode and the conduction level edge of the semiconductor. Here,  $\chi_n$  corresponds to the

electron affinity given by the difference between the conduction level edge and the vacuum level.

Upon intimate contact, charge transfer of electrons and holes, driven by the Fermi level difference between the two solids, will occur between the electrode and the semiconductor to establish thermal equilibrium. Thermal equilibrium is established when the Fermi level in the semiconductor is aligned with the Fermi level of the electrode and the system possess a common spatially constant Fermi level. A schematic picture is shown in Figure 2.1. The equilibrium carrier density in the semiconductor *at the contact* is then given by

$$n_{el} = N_c \exp\left(-\frac{\varphi_{n,el}}{kT}\right), \quad (2.1.6)$$

$$p_{el} = N_v \exp\left(-\frac{\varphi_{p,el}}{kT}\right), \quad (2.1.7)$$

for electrons and holes, respectively. For the case  $\Phi_{el} < \Phi_S$ , there will be a surplus of electrons and a deficit of holes in the semiconductor. The situation is reversed when  $\Phi_{el} > \Phi_S$ . If the net charge transfer is large enough, the Fermi level alignment is also accompanied with an energy-level bending within the semiconductor (close to the contact); see Figure 2.1.

In general, when a metal-semiconductor interface is formed, depending on the quality of the metal and semiconductor surfaces, there might also be impurity-induced, interface-induced, and/or relaxed states present within the gap at the interface [67–70]. In effect, this means that the work function at the contact is strongly dependent on interface properties, such as the density and the energetic position of gap states. Conversely, the work function at the contact can also be modified by permanent dipole moments (*e.g.* using self-assembled mono-layers), or by using doped interlayers.

### 2.1.2 The metal-insulator-metal (MIM) concept

When an intrinsic semiconductor layer is sandwiched between two electrodes a different situation arises. Since the carrier density within the intrinsic semiconductor is inherently very low, these types of thin-film devices essentially behave

as metal-insulator-metal (MIM) structures.

Upon contact, electrons are transferred from the low-work function cathode to the high-work function anode, until the electrode Fermi levels are equal. This results in net negative and positive charge at the anode and cathode surface, respectively, inducing a built-in electric field in the active layer [19, 71]. If the space charge injected into the active layer from the contacts is negligible, the electric field  $F$  in the active layer is uniform. These types of contacts are generally referred to as neutral (or non-ohmic) contacts. A schematic picture of the energy level diagrams of a MIM device with neutral contacts is depicted in Figure 2.2. At thermal equilibrium ( $E_F = \text{const.}$ ), the carrier density vary exponentially with  $x$  inside the active layer:  $p(x) = p_{an} \exp(qFx/kT)$ . Provided that space-charge effects remain negligible under the application of an external voltage (low voltages), the electric field is then given by

$$F = \frac{V - V_{bi}}{d}. \quad (2.1.8)$$

The corresponding potential energy (energy levels), relative to the Fermi level at the cathode, drops linearly across the semiconductor layer as

$$E_v(x) - E_{F,cat} = q(V - V_{bi}) \left[ \frac{x - d}{d} \right] - \varphi_{p,cat}, \quad (2.1.9)$$

where  $\varphi_{p,cat}$  is the hole-injection barrier at the cathode.

### 2.1.3 Ohmic contacts

To ensure efficient charge injection or collection at least one of the contacts needs to be ohmic. A contact is said to be ohmic for holes (electrons) when the hole (electron) current is not limited by this contact. This corresponds to a contact whose resistance or impedance is negligibly small compared to the (rest of) bulk. In practice, a contact becomes ohmic for holes (electrons), when the hole (electron) density at the contact is much larger than within the bulk [15, 19]. This can be achieved by choosing a metal that forms a negligibly small

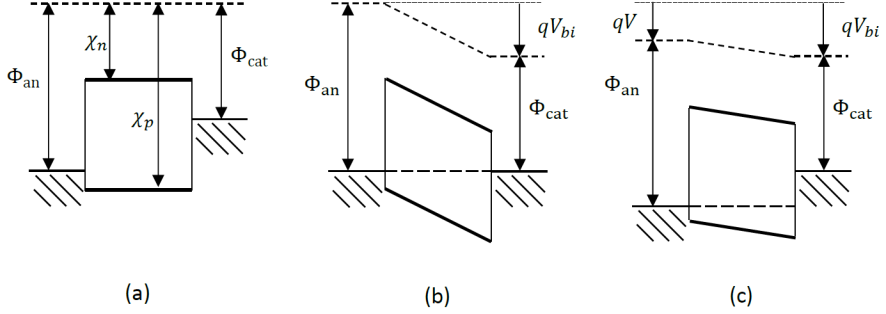


Figure 2.2: Schematic energy level diagrams of a metal-insulator-metal (MIM) device with neutral contacts, which assume that the injected space charge within the active layer (insulator) is negligible: (a) before contact, (b) at thermal equilibrium after contact ( $V = 0$ ), and (c) at an applied positive voltage  $V > 0$ . The energy level diagram in (a) is the same as the one obtained by applying a voltage  $V = V_{bi} = V_{bi,0}$ , referred to as flat-band conditions.

injection barrier with the semiconductor or by heavily doping the region of the semiconductor layer close to the metal.

### Asymmetric contacts with an injecting contact at the anode

When the injection barrier for holes is small at the anode, the amount of carriers originating from the anode can be large enough to cause energy-level bending in the vicinity of the contact in the active layer. The subsequent energy-level bending, determined by the Poisson equation, obeys

$$\frac{d^2 E_v(x)}{dx^2} = \frac{q^2 p(x)}{\varepsilon \varepsilon_0}, \quad (2.1.10)$$

under hole-dominating conditions. In general, at large carrier concentrations, the shape of the DOS becomes important (degenerate regime) [70, 72, 73]. For a Gaussian DOS, the hole density at thermal equilibrium is given by

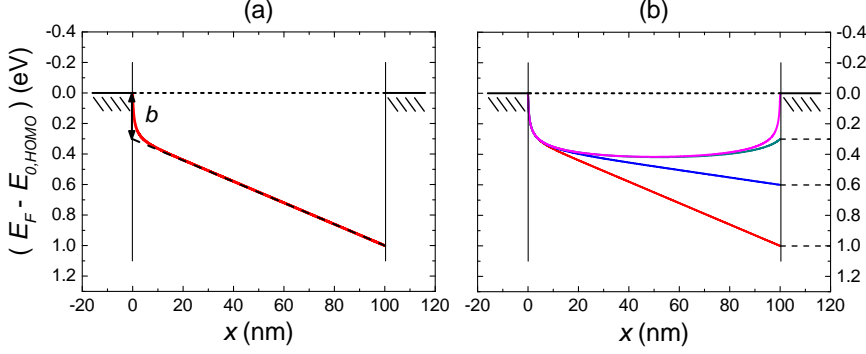


Figure 2.3: (a) Energy level diagram of thin-film device having an Ohmic contact for holes at the anode and a large barrier at the cathode. The device can be treated as a MIM device with an effective injection barrier  $b$  at the anode. In (b) the same device is simulated for different injection barriers at the cathode. A Gaussian distribution (Eq. (2.1.11)) with  $\sigma = 3kT$  and  $N_0 = 10^{21} \text{ cm}^{-3}$  is assumed. The Fermi level of the anode is taken to coincide with the DOS center  $E_{0,HOMO}$  at the anode contact ( $x = 0$ ).

$$p(x) = \frac{N_0}{\sqrt{2\pi\sigma^2}} \int_{-\infty}^{\infty} \frac{\exp\left(-\frac{[E_{0,HOMO}(x)-E]^2}{2\sigma^2}\right)}{1 + \exp\left(\frac{[E_F-E]}{kT}\right)} dE, \quad (2.1.11)$$

where  $\sigma$  is the Gaussian disorder parameter and  $E_{0,HOMO}$  is the center of the HOMO DOS.

At small energetic disorder  $\sigma$ , however, the Boltzmann approximation may be used, and Eq. (2.1.11) can be simplified and re-expressed as  $E_v(x) - E_v(0) = kT \ln[p(0)/p(x)]$ , where  $E_v = E_{0,HOMO} + \sigma^2/2kT$ . Then, if the anode is hole-injecting, while the cathode contact is neutral ( $p(0) \gg p(d)$ ), the hole density within the active layer can be obtained as [74]

$$p(x) = \frac{2B^2 n_0}{\sinh^2\left(\frac{Bx}{d} + \sinh^{-1}\left[B\sqrt{\frac{2n_0}{p(0)}}\right]\right)}, \quad (2.1.12)$$



where  $n_0 \equiv \varepsilon\varepsilon_0 kT/q^2 d^2$  and  $B = \sinh^{-1} \left[ B \sqrt{2n_0/p(d)} \right] - \sinh^{-1} \left[ B \sqrt{2n_0/p(0)} \right]$  as determined from the boundary conditions at the contacts.<sup>5</sup> Provided that the hole density  $p(0)$  at the anode is large enough for energy-level bending to occur, Eq. (2.1.12) reduces to  $p(x) \approx p(0)/[1 + x/\lambda_{an}]^2$  for  $x$  close to the anode, where  $\lambda_{an} = \sqrt{2\varepsilon\varepsilon_0 kT/q^2 p(0)}$  is a characteristic screening length for holes at the anode.

In Figure 2.3(a), the energy level diagrams are shown at moderate  $\sigma$  for conditions when the contact at the anode may be regarded as ohmic for holes. With the exception of the band bending near the injecting contact, the energy levels are linear, in accordance with the MIM picture (see Figure 2.2). Within the band-bending region, extending a few nm into the active layer, the carrier density is generally much higher than in the rest of the bulk. This (thin) accumulation region is acting as a virtual (extended) anode contact with an effective hole-injection barrier  $b$ . Under low-voltage operation, the device subsequently behaves as a MIM diode but with a reduced built-in voltage [30]

$$qV_{bi} = qV_{bi,0} - b, \quad (2.1.13)$$

where  $b$  is the magnitude of energy-level bending within the hole accumulation region. The effect of increasing the disorder parameter  $\sigma$  is mainly to change  $b$ .

## Two hole-injecting contacts

In the case when both contacts are hole-injecting, we arrive at a situation where the hole densities are larger at the contacts than within the active layer. In this

---

<sup>5</sup>Assume  $E_v(x) - E_v(0) = kT \ln[p(0)/p(x)]$ . Then, after multiplying both sides with  $dE_v(x)/dx$  and integrating, Eq. (2.1.10) can be rewritten as

$$\left[ \frac{dE_v(x)}{dx} \right]^2 = \left( \frac{2kT}{\lambda_{an}} \right)^2 \exp \left( \frac{E_v(x) - E_v(0)}{kT} \right) \pm \left( \frac{2kTB}{d} \right)^2,$$

where the last term to the right is an integration constant to be determined from the boundary conditions at the contacts. The (+) and the (−) sign corresponds to the case with  $p(x) > p(d)$  (non-injecting cathode) and  $p(x) < p(d)$  (injecting cathode), respectively, for  $x < d$ . By separating this equation and integrating,  $E_v(x)$  can be obtained.

case, a considerable energy-level bending extending well within the active layer is present at both contacts, with the electric field changing its sign inside the active layer. The situation is depicted in Figure 2.3(b). In the non-degenerate limit (low disorder), the corresponding hole density under equilibrium conditions (constant Fermi level) is given by [74]

$$p(x) = \frac{2B^2 n_0}{\cos^2 \left( \frac{Bx}{d} - \arccos \left[ B \sqrt{\frac{2n_0}{p(0)}} \right] \right)}, \quad (2.1.14)$$

where  $B = \arccos \left[ B \sqrt{2n_0/p(0)} \right] + \arccos \left[ B \sqrt{2n_0/p(d)} \right]$ .<sup>5</sup> When the hole densities at both contacts are much larger than  $2\pi^2 n_0$ , one finds  $B \rightarrow \pi$ . In this case, the hole density within the region close to the cathode can be approximated as  $p(x) \approx p(d)/[1 + (d-x)/\lambda_{cat}]^2$ , with  $\lambda_{cat} = \sqrt{2\varepsilon\varepsilon_0 kT/q^2 p(d)}$  being the associated screening length for carriers accumulated at the cathode.

#### 2.1.4 The image charge effect

At large injection barriers, on the other hand, the carrier density close to the contact might become very small. If the average distance between carriers inside the active layer is much larger than the relevant device dimensions, single-particle effects need to be taken into account [75]. From a single-particle perspective, an injected charge carrier within the semiconductor will induce an oppositely-charged image in the metal. The corresponding electrostatic potential energy  $q\psi(x) = E_{F,cat} - E_v(x)$  (relative to the Fermi level of the electrode) between the positively-charged hole  $q$  within the active layer and its negatively-charged image  $-q'$  in the cathode is given by [15]

$$q\psi(x) = \varphi_{p,cat} - \frac{qq'}{16\pi\varepsilon\varepsilon_0 [d-x]} - qF[x-d], \quad (2.1.15)$$

where  $F$  is the external electric field. When  $F < 0$ , the image charge potential Eq. (2.1.15) will effectively reduce the injection barrier for holes at the cathode

by

$$\Delta\varphi = q\sqrt{\frac{q'F}{4\pi\epsilon\epsilon_0}}. \quad (2.1.16)$$

In case of a metal cathode, we have  $q' = q$ . However, if another dielectric medium (*e.g.* another semiconductor) with a dielectric constant of  $\epsilon_c$  is used as cathode (interlayer), the magnitude of the image charge is reduced as:  $q'/q = (\epsilon_c - \epsilon)/(\epsilon_c + \epsilon)$  [76–78]. Image charge effects are important near contacts that have large injection barriers at which the carrier densities are low (single-particle approximation) [75]. In contrast, for contacts with low injection barriers, where the density at the contact becomes significant, the image charges tend to be screened (effective medium) and can be neglected.

## 2.2 Charge-transfer mechanisms at electrode-semiconductor contacts

Charge-carrier injection and collection at contacts between electrode and active semiconductor layers is a crucial part of the operation of sandwich-type thin-film devices. Many applications also require contacts that are blocking in terms of carrier injection and/or extraction. This may be realized by tuning the energetics at the contacts or by covering the conductive layer with a wide-bandgap insulator or a charge-selective electrode interlayer. In the following, charge-transfer mechanisms taking place between an electrode and a semiconductor are discussed.

### 2.2.1 Thermionic emission and the concept of surface recombination at contacts

In the case when an injection barrier is present between the electrode and the semiconductor, carriers that are to be injected from the electrode into the semiconductor have to traverse this energetic barrier. During ideal conditions, the

particle current flowing from the electrode to the semiconductor is usually described in terms of a thermally activated process referred to as thermionic emission. This is analogous to the emission of (hot) electrons from a metal into (the state continuum of) vacuum at free metal surfaces [79]. For a given (effective) injection barrier between the electrode and the semiconductor, the current of electrons flowing into the conduction band of the semiconductor due to thermionic emission is given by [15]

$$J_{m \rightarrow s} = -A_{th}^* T^2 [1 - Q] \exp\left(-\frac{\varphi_{n,el}}{kT}\right), \quad (2.2.1)$$

where  $A_{th}^* = qk^2 m^* / 2\pi^2 \hbar^3$  is the effective Richardson coefficient and  $Q$  is a reflection factor. Eq. (2.2.1) assumes that the carriers are emitted into the semiconductor from the metal in accordance with a Maxwell-Boltzmann velocity distribution (free electron gas), implying that the carrier conduction in the semiconductor (or the region close to the contact) takes place by band transport.

On the other hand, the collection current of electrons flowing from the semiconductor into the electrode is typically presented as an effective surface recombination process at the contact,  $J_{s \rightarrow m} = qS_R n$ , where  $S_R$  is the collection (or recombination) velocity at the surface. At thermal equilibrium, the macroscopic current is zero, implying that  $J_{m \rightarrow s} = -qS_R n_{el}$ , where  $n_{el} = N_c \exp(-\varphi_{n,el}/kT)$  is the equilibrium hole density at the electrode contact [15, 80]. Subsequently, the net surface recombination current at the contact can be expressed as

$$J = qS_R [n - n_{el}], \quad (2.2.2)$$

with the associated surface recombination velocity being equal to

$$S_R = \frac{A_{th}^* T^2}{qN_c} [1 - Q]. \quad (2.2.3)$$

For an ideal metal-semiconductor interface  $Q \rightarrow 0$ , the upper limit of  $S_R$  is given by the average thermal velocity (in the  $x$ -direction) [15]. For free electrons, this

corresponds to  $S_R = 2.7 \times 10^6$  cm/s at  $T = 300$  K.

### 2.2.2 Interpretation of the surface recombination velocity at contacts in hopping systems

The thermionic injection of carriers into hopping systems has been investigated by Gartstein and Conwell and others [81–87]. In these studies, the charge transfer rate is described in terms of hopping transport, taking both the energetic disorder and the barrier-lowering effect due to image charges into account. Simplified models for the surface recombination velocity have also been discussed to some extent [27, 88, 89]. From a qualitative point of view, the charge-carrier collection at electrode-organic semiconductor contacts can be portrayed as follows.

#### Metal-semiconductor contacts

Consider a metal-semiconductor contact where the hopping rate in the semiconductor is assumed to follow the Miller-Abrahams rate, Eq. (1.2.7). The contact is assumed to be ideal, containing an infinite amount of available states in the metal ( $Q = 0$ ). In this case, the electron flow from the semiconductor to the metal consists of down-hill jumps only (possibly along relaxed states in the image potential). The situation is illustrated in Figure 2.4(a). In accordance with the discussion in Section 1.3.2, the surface recombination velocity should then be equal to the saturated drift velocity as

$$S_R = a\nu_0 \exp(-2\gamma a), \quad (2.2.4)$$

where  $a$  is the hopping distance between a site in the semiconductor and a relaxed site at the metal interface. Since Eq. (2.2.4) corresponds to the upper limit of the drift velocity (for Miller-Abrahams hopping), we thus always have  $S_R \geq \mu|F|$  in this case. Eq. (2.2.4) can also be related to the zero-field EGDM

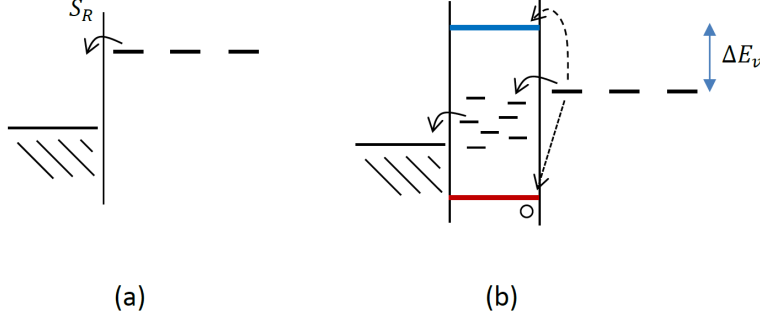


Figure 2.4: Interpretation of the surface recombination velocity at contacts in hopping system: (a) ideal metal-semiconductor contact, and (b) blocking contact where a charge-selective electrode interlayer is inserted between the metal and the semiconductor. The surface recombination of electrons at the blocking contact may take place via thermal activation, hopping transport via impurity-induced gap states, or direct recombination with holes in the interlayer.

mobility at low carrier densities (Eq. (1.3.14)) via

$$S_R \sim \frac{\sigma \mu(T)}{qa} \exp \left( c_2 \left[ \frac{\sigma}{kT} \right]^2 \right). \quad (2.2.5)$$

With typical values of  $\mu = 10^{-4} \text{ cm}^2/\text{Vs}$  (at  $T = 300 \text{ K}$ ) and  $a = 1.5 \text{ nm}$ , this amounts to  $S_R \sim 300 \text{ cm/s}$  for  $\sigma = 58 \text{ meV}$ . This is to be compared to  $S_R \sim 3 \times 10^6 \text{ cm/s}$  expected for "ideal" inorganic semiconductor-metal contacts. It should be noted that  $\gamma$  and  $a$  can in general be different near the interface compared to the bulk.

### Blocking contacts

In several applications, contacts that are selective from the view point of carrier extraction are desired. A charge-selective contact is a contact that only allow one type of carrier to pass through it, whereas the other type is blocked.

Electron-blocking contacts are realized by inserting an electrode interlayer with a higher  $E_c$ , leading to a conduction level-offset  $\Delta E_c$  at the interlayer-organic semiconductor interface. This creates an energetic barrier for electron extraction which reduces the effective hopping velocity Eq. (2.2.4) by a factor of  $\exp(\Delta E_c/kT)$ .

In the ideal case, when the energy-level offset is very large, no electrons can be extracted at the electron-blocking contact layer and  $S_R = 0$ . In practice, however, impurity-induced (or interface-induced) gap states are always present to some extent within the blocking layer [90]. In such situations, electrons may be conducted by hopping via gap states through the layer. This may be described in terms of an effectively reduced surface recombination velocity  $S_{R,\text{eff}} = S_R [1 - Q]$ , relative to Eq. (2.2.4). The factor  $(1 - Q)$  represents the probability of finding a state at the interface. If the density of gap states is large ( $Q \rightarrow 0$ ), the blocking layer effectively behaves as a metal. Furthermore, for charge-selective contacts utilizing conductive (doped) transport layers, direct recombination across the interface presents an additional surface recombination channel. If this mechanism is dominating (*e.g.* taking place between an electron in the active layer and a hole in the  $p$ -doped layer), the associated surface recombination velocity becomes dependent on the doping concentration of the conductive transport layer. A schematic overview is shown in Figure 2.4(b).

## 2.3 Unipolar charge transport in thin-film devices

At  $V = 0$  in dark (thermal equilibrium), the drift component of the current is exactly balanced by diffusion, and the net macroscopic current is zero. Upon applying an external voltage, the magnitude of the internal electric field is changed, resulting in an imbalance between drift and diffusion and a subsequent current. Depending on the applied voltage, the transport properties, and the type of device, different current regimes can be identified. In this section, we consider unipolar (single-carrier) devices with a hole-injecting ohmic contact at the anode and a hole-collecting contact at the cathode.

### 2.3.1 Theory

The current density is obtained by solving the drift-diffusion equation for holes. In accordance with Section 2.2, the boundary conditions at the contacts are

$$J_p(d) = qS_p [p(d) - p_{cat}], \quad (2.3.1)$$

$$J_p(0) = -qS_p [p(0) - p_{an}], \quad (2.3.2)$$

where  $S_P$  and  $S_p$  is the (effective) surface recombination velocity for holes at the anode and cathode contact, respectively. Taking the anode to be ohmic for holes ( $qS_P p_{an} \rightarrow \infty$ ), we thus have  $p(0) = p_{an}$  (or  $E_{Fp}(0) = E_{F,an}$ ), where  $p_{an} = N_v \exp(-b/kT)$  with the effective injection barrier  $b$  (see Section 2.1.3). For hole-dominated charge transport, the current can then be evaluated as<sup>6</sup>

$$J = \frac{qv_p p_{cat}}{1 + v_p/S_p} \left[ \exp\left(\frac{qV}{kT}\right) - 1 \right], \quad (2.3.3)$$

where  $p_{cat} = N_v \exp(-\varphi_{cat}/kT)$  and

$$v_p \equiv \left[ \int_0^d \frac{q}{\mu kT} \exp\left(\frac{E_{F,cat} - \varphi_{p,cat} - E_v(x)}{kT}\right) dx \right]^{-1} \quad (2.3.4)$$

is an effective transport velocity for holes within the active layer [15, 80], which depends on the mobility and the electrostatic potential. Note that, since only holes are considered in this section, the notation  $\varphi_{p,cat} = \varphi_{cat}$  and  $\mu_p = \mu$  is used interchangeably.

In Figure 2.5, a typical  $J$ - $V$  curve of a hole-only MIM diode is shown for

---

<sup>6</sup>Utilizing Eq. (1.3.9), one finds  $J_p(x) = \mu_p p \frac{dE_{Fp}}{dx} = \mu_p kT N_v \exp\left(\frac{E_v - E_{Fp}}{kT}\right) \frac{d}{dx} \left(\frac{E_{Fp}}{kT}\right)$ . Assuming that  $E_{Fp}(0) = E_{F,an}$ , the hole current equation can in conjunction with Eq. (2.1.1) and Eq. (2.3.1) be rewritten as

$$\int_0^d \frac{J_p(x)}{\mu_p kT} \exp\left(\frac{E_{F,cat} - \varphi_{p,cat} - E_v(x)}{kT}\right) dx = p_{cat} \left[ \exp\left(\frac{qV}{kT}\right) - 1 \right] - \frac{J_p(d)}{qS_p}.$$

For hole-only transport,  $dJ_p/dx = 0$ , the steady-state hole current is independent of  $x$  and  $J_p(x) = J_p(d) = J$ .



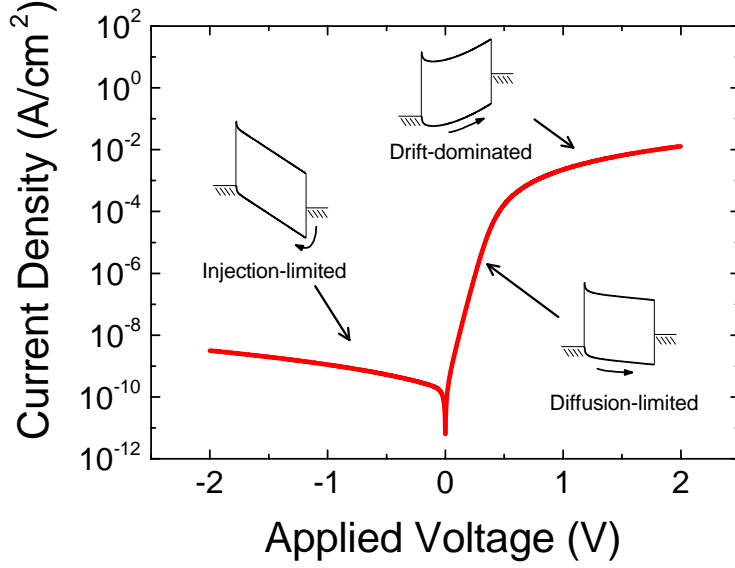


Figure 2.5: The current-voltage characteristics for a hole-only MIM diode with an ohmic contact at the anode is shown on a lin-log scale. The insets depict the corresponding energy level diagrams for the different current regimes: injection-limited ( $V < 0$ ), diffusion-limited ( $0 < V < V_{bi}$ ), and drift-dominated ( $V > V_{bi}$ ).

the case when the charge collection is ideal and not limited by the contacts ( $S_p \gg v_p$ ). In forward bias ( $V > 0$ ), when holes are injected from the anode and collected at the cathode, the current at low voltages  $0 < V < V_{bi}$  is in this case limited by diffusion against the built-in voltage, whereas for  $V > V_{bi}$  the current becomes dominated by the drift component as the current eventually becomes space-charge-limited. In reverse bias ( $V < 0$ ), on the other hand, the current is limited by injection from the cathode contact. In general, depending on the contact properties and the prevailing space-charge effects, other situations may also occur. The different current regimes will be discussed in more detail in the following.

### 2.3.2 Diffusion-limited currents

If the current is limited by charge transport within the bulk and not by the kinetics at the collecting contact, *i.e.*  $S_p \gg v_p$ , the current at low voltages ( $0 < V < V_{bi}$ ) is diffusion-limited. Under these conditions, the cathode virtually acts as a perfect sink that is able to instantly collect all additional holes without any hold up, the hole density at the cathode contact retaining its thermal equilibrium value. The current is constituted by holes injected from the anode, diffusing against the (reverse) internal electric field, and collected at the cathode. The diffusion-limited current reads

$$J = qv_p N_v e^{-\varphi_{cat}/kT} \left[ \exp\left(\frac{qV}{kT}\right) - 1 \right], \quad (2.3.5)$$

where  $v_p$  is the associated effective diffusion velocity given by Eq. (2.3.4). For a MIM diode, with  $E_v(x)$  given by Eq. (2.1.9) and  $V_{bi} = V_{bi,0} - b$ , we have

$$v_p = \frac{q\mu_p [V_{bi} - V]}{d \left[ 1 - \exp\left(\frac{q[V - V_{bi}]}{kT}\right) \right]}, \quad (2.3.6)$$

for  $0 \leq V < V_{bi}$ . At voltages close to zero, the current Eq. (2.3.5) depends linearly with the applied voltage. At larger forward bias, the strength of the opposing internal electric field is reduced, leading to an exponential increase of the collection current. Noting that the effective diffusion velocity simplifies as  $v_p \sim \mu |F|$  for voltages below  $V_{bi}$ , the condition for the charge collection to be diffusion-limited is  $S_p \gg \mu |F|$ . For a mobility of  $10^{-4} \text{ cm}^2/\text{Vs}$ , this corresponds to  $S_p \gg 10 \text{ cm/s}$  at  $|F| = 1 \text{ V}/100 \text{ nm}$ .

In general, also the band-bending parameter  $b$  might depend on the voltage. However, the shape of the current in Eq. (2.3.5) is fairly insensitive to the exact value of  $b$  at voltages below  $V_{bi}$ ; only when  $V$  is close to  $V_{bi}$  does the value of  $b$  become important [30]. The band-bending parameter to be used in Eq. (2.3.5) can be well approximated by

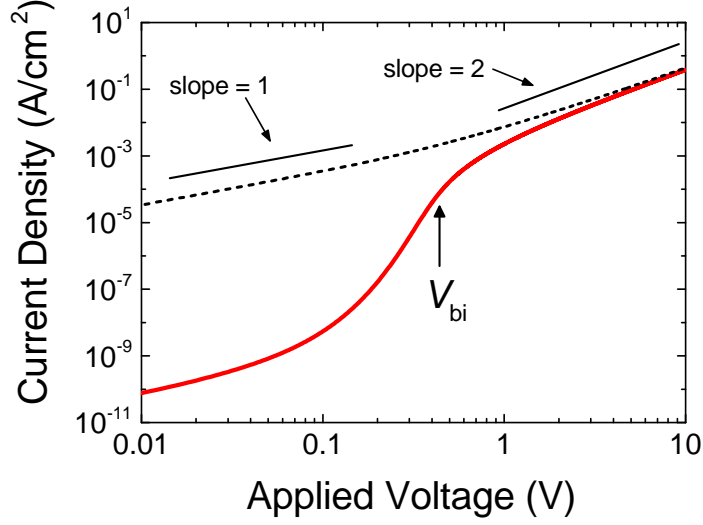


Figure 2.6: Current-voltage characteristics of the hole-only MIM diode (from Figure 2.5) in forward bias on log-log scale. The current for a symmetric device with two hole-injecting contacts, as indicated by the dashed line, is shown for comparison. At voltages above the built-in voltage, the space-charge-current limit is approached, distinguished by the slope of two on the log-log scale ( $J \propto V^2$ ).

$$b = \frac{kT}{q} \left[ \ln \left( \frac{q^2 N_v d^2}{2\varepsilon\varepsilon_0 kT} \right) - 2 \right], \quad (2.3.7)$$

relative to  $E_v(0)$ , as demonstrated by de Bruyn *et al.* [30].

### 2.3.3 Space-charge-limited currents

For  $V > V_{bi}$ , the internal electric field is reversed facilitating injection of holes from the anode. Under these conditions, the space charge of the injected carriers dominates, and the assumption of a constant field inside the active layer is no

longer valid. The corresponding  $J$ - $V$  curve is shown in Figure 2.6. At large enough voltages, the effect of diffusion becomes negligible and the current is dominated by drift,  $J = q\mu p(x) F(x)$ . The electric field is then adjusted in accordance with  $dF/dx = qp(x)/\varepsilon\varepsilon_0 = J/\mu\varepsilon\varepsilon_0 F(x)$ . Provided that a potential minimum is present close to the hole-injecting anode ( $F(0) \approx 0$ ) (see inset in Figure 2.5), the current density can be readily obtained [91]. The *space-charge-limited current* (SCLC) for unipolar carrier injection reads

$$J = \frac{9}{8} \mu \varepsilon \varepsilon_0 \frac{(V - V_{bi})^2}{d^3}, \quad (2.3.8)$$

for  $V \gg V_{bi}$ . Eq. (2.3.8) is generally referred to as the Mott-Gurney square law or Child's law for solids.

Similarly, the net injected charge (per unit area)  $\Delta Q = Q_s(V) - Q_s(0)$ , given by the difference between the net charge within the active layer (Eq. (1.3.26)) at the applied voltage  $V$  and at thermal equilibrium ( $V = 0$ ), in the SCLC limit can be found as

$$\Delta Q = \frac{3\varepsilon\varepsilon_0 [V - V_{bi}]}{2d} = \frac{3}{2} C_{geo} [V - V_{bi}], \quad (2.3.9)$$

for  $V \gg V_{bi}$ . This is the net injected charge that is accumulating within the active layer during steady-state conditions. The capacitance (per unit area) of the device in the SCLC limit is thus effectively increased by a factor of 1.5 relative to the geometric capacitance.

### 2.3.4 Injection-limited currents

In the reverse bias, on the other hand, the current is controlled by diffusion of carriers injected at the cathode. In this case, when carrier injection from contacts with high injection barriers is the source for the current, the current is said to be injection-limited. Under these conditions, the barrier lowering effect due to image charges become important. Taking into account the image-charge potential Eq. (2.1.15), with  $q' = q$ , at the cathode in Eq. (2.3.4), analytical

approximations for the diffusion-limited current Eq. (2.3.5) can be obtained at low and high electric field strengths, as discussed by Emtage and O'Dwyer [92]. At low electric field strengths, Eq. (2.3.6) applies, and Eq. (2.3.4) is well approximated by  $v_p \approx \mu |F|$ . At high electric field strengths  $|F| > kT/q r_c$ , in turn, the reverse current approaches

$$J = \frac{q\mu [V - V_{bi}] N_v}{d} \left[ \frac{4kTd}{\pi^2 q |V - V_{bi}| r_c} \right]^{1/4} \exp \left( -\frac{\varphi_{cat} - \Delta\varphi}{kT} \right), \quad (2.3.10)$$

where  $\Delta\varphi = \sqrt{q^3 |V - V_{bi}| / 4\pi\epsilon\epsilon_0 d}$  and  $r_c = q^2 / 4\pi\epsilon\epsilon_0 kT$  is the Coulomb capture radius. The current under these circumstances, is limited by the diffusion of holes over the lowered potential barrier at the cathode, and is sometimes also referred to as diffusion-limited thermionic emission. Figure 2.7 shows the experimental reverse-bias current of a hole-only MIM diode, based on the polymer PTAA. The current is indeed well reproduced by Eq. (2.3.10).

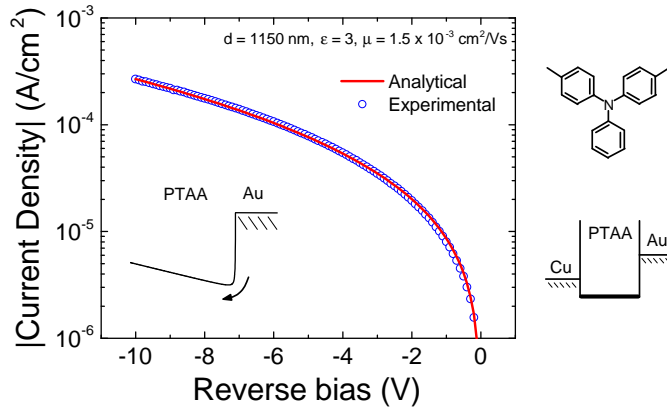


Figure 2.7: Injection-limited cathode currents in hole-only organic diodes, based on poly-(tri-arylamine) (PTAA) [93]. The device structure is Cu/PTAA/Au. The experimental hole-injection current (reverse bias) from the Au-cathode is well reproduced by Eq. (2.3.10), with  $N_v e^{-\varphi_{cat}/kT} \approx 2.1 \times 10^{12} \text{ cm}^{-3}$ . For  $N_v = 3 \times 10^{20} \text{ cm}^{-3}$ , this amounts to  $\varphi_{cat} \approx 485 \text{ meV}$ . The details of the polymer are given in Refs. [94] and [95].

In terms of charge collection at the cathode, the impact of the image potential is to effectively reduce the built-in voltage  $qV_{bi}$  by  $\Delta\varphi_{\text{eff}} = \Delta\varphi - \frac{1}{4}kT \ln(\pi^2 q |F| r_C / 4kT)$  at  $|F| > kT / qr_C$ . At moderate electric field strengths, this reduction is small and overshadowed by the reduction (of  $V_{bi}$ ) due to the energy-level bending from the ohmic anode contact. In the remainder of this thesis, the effect of the image charges on the charge collection is assumed to be negligible.

### 2.3.5 Ohmic linear current-voltage regime

In the special case of two hole-injecting (symmetric) contacts, a situation with vanishing built-in voltage similar to the one in Figure 2.3(b) is approached. When both contacts are ohmic for hole injection, the hole density profile at small voltages will not change significantly from the equilibrium hole distribution given by Eq. (2.1.14). Under these conditions, the current relation  $J = \mu p d E_{Fp} / dx$  can readily be separated and integrated as:  $J = V / \int_0^d [1 / q \mu p(x)] dx$ . The current density at small voltages is consequently found as [96]

$$J = \frac{2q\mu p_{\text{center}} V}{d} \approx \frac{4\pi^2 \varepsilon \varepsilon_0 \mu kT}{q} \frac{V}{d^3}, \quad (2.3.11)$$

where the hole density near the center of the device is given by  $p_{\text{center}} = 2B^2 n_0 \approx 2\pi^2 \varepsilon \varepsilon_0 kT / q^2 d^2$ . This type of current exhibits a linear voltage dependence, commonly referred to as an ohmic current, as shown in Figure 2.6. As the magnitude of the voltage is increased above  $|V| > 32\pi^2 kT / 9q$ , however, the SCLC limit (Eq. (2.3.8)) is eventually approached.

### 2.3.6 The case with a doped semiconductor layer; the Schottky barrier

If the active layer is  $p$ -doped, a different scenario arises. In this case, a space-charge region (of ionized dopants), depleted of free holes, is formed adjacent to the cathode. Provided that the doping concentration is high enough, the

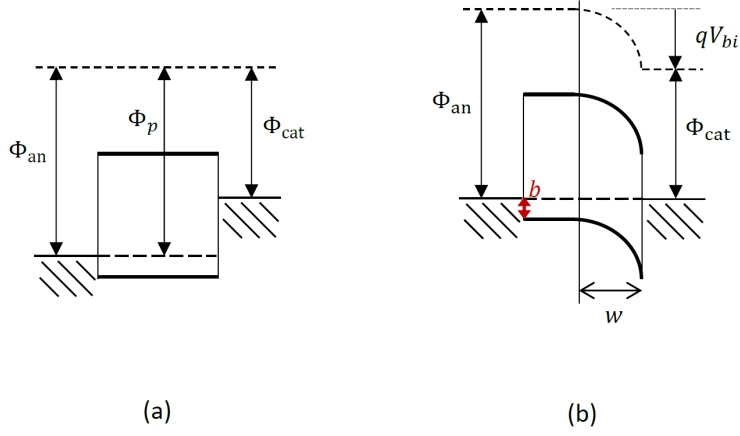


Figure 2.8: Schematic energy level diagrams for the case with a doped semiconductor layer. In (a) the situation before contact (or at flat-band conditions,  $V = V_{bi}$ ), whereas in (b) the situation after contact at thermal equilibrium ( $V = 0$ ).

entire potential difference is absorbed over the space-charge region at quasi-equilibrium conditions; in the remainder of the active layer, referred to as the quasi-neutral region, flat-band conditions prevail. The situation for  $V = 0$  is depicted in Figure 2.8.

The thickness of the depleted space-charge region depends on the dielectric properties of the semiconductor material, the concentration of ionized dopants  $N_p$ , and the potential difference. Taking the concentration of ionized dopants to be uniform, the thickness of the space-charge region is given by [15]

$$w_0 \approx \sqrt{\frac{2\varepsilon\varepsilon_0}{qN_p} \left( V_{bi} - V - \frac{kT}{q} \right)}, \quad (2.3.12)$$

where the term  $kT/q$  is a correction due to diffusion. Eq. (2.3.12) is valid provided that the doping concentration is large enough for  $w_0 < d$  to be fulfilled [97], *i.e.*  $N_p > 2\varepsilon\varepsilon_0 [V_{bi} - V]/qd^2$ . Note that the built-in voltage is in this case

given by  $V_{bi} = V_{bi,0} - b/q$ , with the energy-level bending near the anode given by  $b = kT \ln(N_v/N_p)$ . The corresponding potential energy (relative to the cathode Fermi level) in the space-charge region  $d - w_0 < x \leq d$  reads

$$E_v(x) - E_{Fcat} \approx -\varphi_{cat} - \frac{q^2 N_p}{\varepsilon \varepsilon_0} \left[ \frac{(d-x)^2}{2} - w_0(d-x) \right]. \quad (2.3.13)$$

The electric field is thus linear with position within the space-charge region, whereas  $F = 0$  applies inside the quasi-neutral region (where  $p = N_p$ ). In dark, this system acts as a device with an effective active layer thickness of  $w_0$ , with the quasi-neutral region virtually behaving as an extension of the contact. The forward bias current then approximates as [15]

$$J \approx q\mu \sqrt{\frac{2qN_p[V_{bi} - V]}{\varepsilon \varepsilon_0}} N_v e^{-\varphi_{cat}/kT} \left[ \exp\left(\frac{qV}{kT}\right) - 1 \right], \quad (2.3.14)$$

for  $V < V_{bi}$ .

As the voltage is increased beyond the built-in voltage, the depletion region  $w_0 \rightarrow 0$ . With the exception of the neighborhood of the collecting cathode contact, the active layer is essentially neutral in this case, with  $p \approx N_p$ . Under these conditions, the electric field is constant throughout the active layer and the current approximates as  $J \approx q\mu N_p [V - V_{bi}]/d$ . At larger voltages, when  $V > V_{bi} + 8qN_p d^2/9\varepsilon \varepsilon_0$ , the density of injected carriers eventually start to dominate as the current becomes space-charge-limited.

### 2.3.7 The impact of the recombination velocity at the collecting contact

Thus far the charge collection at the cathode contact has been assumed to be excellent ( $S_p \rightarrow \infty$ ). In general, however, this is not necessarily the case (see Section 2.2.2). In situations when  $S_p \ll v_p$ , the charge collection is instead limited by interface kinetics at the (collecting) contact. The corresponding



diode current reads

$$J = qS_p p_{cat} \left[ \exp \left( \frac{qV}{kT} \right) - 1 \right], \quad (2.3.15)$$

for  $V < V_{bi}$ . Figure 2.9(a) shows the simulated  $J$ - $V$  curves for different surface recombination velocities at the collecting cathode. The effect of reducing  $S_p$  is to shift the onset for the injection towards larger voltages; at voltages below  $V_{bi}$ , the effective voltage shift (relative to Eq. (2.3.5)) is  $\Delta_S \approx kT \ln(1 + \mu|F|/S_p)$ . Furthermore, the carrier density at the cathode is related to the applied voltage via

$$p(d) = p_{cat} + \frac{J}{qS_p} \rightarrow p_{cat} \exp \left( \frac{qV}{kT} \right) \text{ for } S_p \ll v_p. \quad (2.3.16)$$

Under these conditions ( $S_p \ll v_p$ ), the quasi-Fermi level is nearly flat throughout the active layer, being separated from the cathode Fermi level by  $qV$ . In case of negligible space charge, the carrier density inside the active layer is then given by  $p(x) = p(d) \exp(qF[x - d]/kT)$ .

At voltages larger than the built-in voltage,  $V > V_{bi}$ , a bias-induced carrier accumulation can be established at the cathode interface for  $S_p \ll v_p$ . Provided that the quasi-Fermi level remains flat within the accumulation region near the collecting contact, the hole density in this region is well approximated by  $p(x) = p(d)/(1 + [d - x]/\lambda)^2$  (see Section 2.1.3), with  $\lambda = \sqrt{2\varepsilon\varepsilon_0 kT/q^2 p(d)}$  being the corresponding screening length. The net injected charge, accumulating at the collecting contact, is then given by **[Paper I]**

$$\Delta Q \approx \sqrt{2\varepsilon\varepsilon_0 kT p(d)} = \sqrt{2\varepsilon\varepsilon_0 kT \left[ \frac{J}{qS_p} + p_{cat} \right]}. \quad (2.3.17)$$

for  $p(d) \gg p_{cat}$ . Eq. (2.3.17) allows for a direct relation between the current and the accumulated charge to be established. Figure 2.9(b) shows the corresponding net injected charge as a function of the applied voltage at different  $S_p$ . This charge is mainly concentrated at the cathode interface and increases with

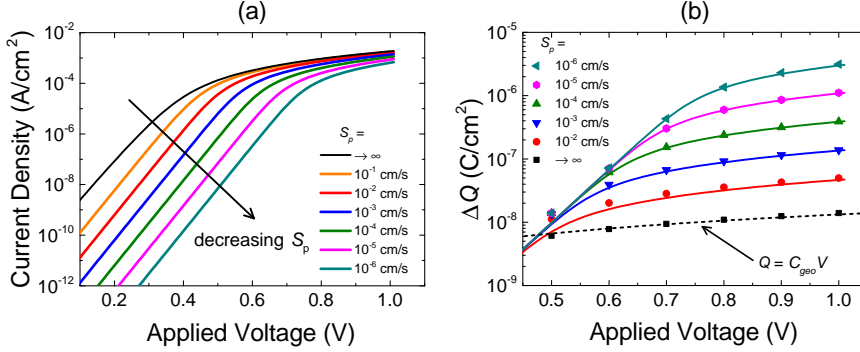


Figure 2.9: The effect of surface recombination velocity  $S_p$  at the hole collecting cathode contact in a hole-only MIM diode. In (a), interface-kinetic-limited  $J$ - $V$  curves for different  $S_p$  are shown. In (b) the net injected charge  $\Delta Q$  at different voltages  $V > V_{bi}$  are simulated (symbols). The analytical approximations Eq. (2.3.17) are indicated by the solid lines. Close to flat-band conditions,  $v_p \approx \mu kT/qd \approx 0.13$  cm/s, where  $\mu = 10^{-4}$  cm²/Vs and  $d = 200$  nm.

decreasing  $S_p$ . We note that, in the SCLC regime ( $J \rightarrow J_{SCLC}$ ), the net injected charge Eq. (2.3.17) is a factor  $\sqrt{\mu kT/qS_p d}$  larger than the corresponding net injected charge (Eq. (2.3.9)) expected in the  $S_p \gg v_p$ -limit.

## 2.4 Bipolar currents in thin-film devices

Thus far we have mainly considered unipolar devices, such as hole-only diodes. If we allow both holes and electrons to be present, charge-carrier recombination within the bulk can no longer be neglected. This is an important process in bipolar (double-carrier) devices such as organic light-emitting diodes and solar cells. The energy level diagrams of a typical bipolar MIM diode are depicted in Figure 2.10.

The steady-state current density  $J = J_p(x) + J_n(x)$  is obtained by solving the hole and electron current equations, subject to Eq. (2.3.1) and (2.3.2) for

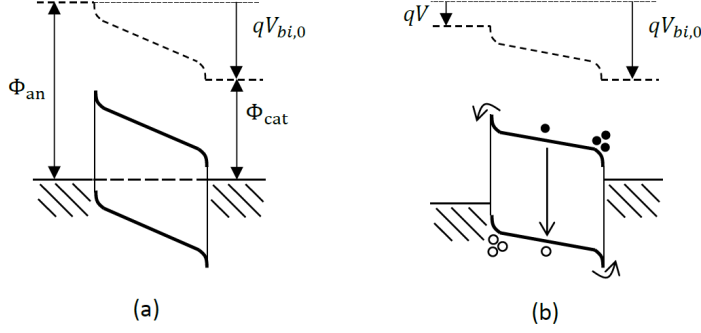


Figure 2.10: Schematic energy level diagrams of a bipolar device (in dark) with a hole-ohmic contact at the anode and an electron-ohmic contact at the cathode (a) at thermal equilibrium ( $V = 0$ ) and (b) under a small forward bias ( $0 < V < V_{bi}$ ). In this case, energy-level bending is present at both contacts. Apart from surface recombination of holes at the cathode, under these conditions also surface recombination of electrons at the anode and bulk recombination (either directly between free electrons and holes or via traps) inside the active layer become significant.

holes and

$$J_n(0) = qS_n [n(0) - n_{an}], \quad (2.4.1)$$

$$J_n(d) = -qS_N [n(d) - n_{cat}], \quad (2.4.2)$$

for electrons;  $S_n$  and  $S_N$  is the surface recombination velocity for electrons at the anode and cathode, respectively, with  $n_{an} = N_c \exp(-\varphi_{n,an}/kT)$  and  $n_{cat} = N_c \exp(-\varphi_{n,cat}/kT)$ . To ensure that the device injects both types of carriers, asymmetric injecting contacts are required. In other words, the contact at the anode needs to be ohmic for hole injection ( $qS_P p_{an} \rightarrow \infty$ ), whereas the contact at the cathode needs to be ohmic for electron injection ( $qS_N n_{cat} \rightarrow \infty$ ).

In the absence of photogeneration, the total current density can be expressed by the sum of the collected hole and electron currents (at the cathode and the anode, respectively) and the bulk recombination current (of carriers lost within

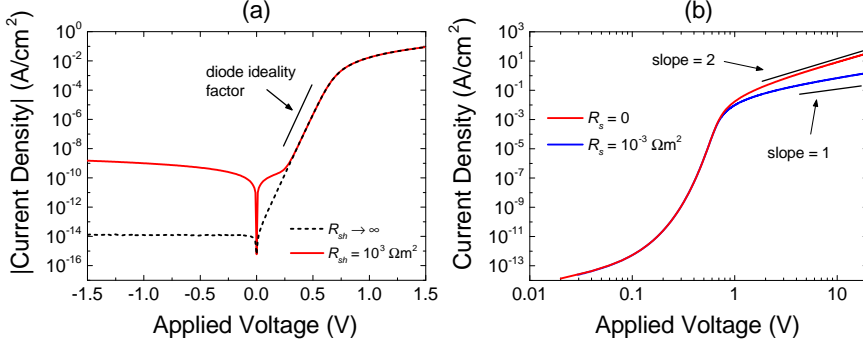


Figure 2.11: Dark current-voltage characteristics of a bipolar MIM diode shown in (a) on a log-lin scale, and (b) in forward bias on log-log scale. The slope of the current within  $0 < V < V_{bi}$  of the log-lin plot determines the diode ideality factor. At low current levels (at small voltages), the current is sensitive to parasitic leakage currents, typically characterized by a finite shunt resistance. At large voltages ( $V > V_{bi}$ ), the space-charge-limited double-injection current is approached, distinguished by the slope of two on the log-log scale ( $J \propto V^2$ ). However, this requires that voltage losses caused by the series resistance from the external circuit, which might become significant at large current levels, are small.

the bulk) as

$$J = J_R + J_S, \quad (2.4.3)$$

where  $J_S = J_n(0) + J_p(d)$  is the net surface recombination current density of minority carriers (*i.e.* electrons at the anode, holes at the cathode) and

$$J_R = q \int_0^d R dx = q \langle R \rangle d, \quad (2.4.4)$$

is the net bulk recombination current density. A typical dark  $J$ - $V$  curve for a bipolar MIM diode is shown in Figure 2.11. It should be noted that at low current levels, parasitic leakage currents characterized by a finite shunt resistance  $R_{sh}$  might become dominating (see Eq. (1.1.1)), increasing the current in reverse bias. At large current levels, on the other hand, voltage losses caused by

a non-zero series resistance  $R_s \neq 0$  of the external circuit reduces the current; when this voltage loss is large the current tends to become linear with the voltage. In the following, however, resistive effects caused by external non-idealities are neglected.

### 2.4.1 The case when bulk recombination dominates

If surface recombination is negligible, the quasi-Fermi level difference between electrons and holes, related to the bulk recombination rate as  $R = \beta_R n_i^2 \times [\exp([E_{Fn} - E_{Fp}]/kT) - 1]$ , is constant throughout the active layer at low voltages and given by  $qV = E_{Fn} - E_{Fp}$ . In this regime ( $V < V_{bi}$ ), the recombination current then reads

$$J = J_R = J_{R,0} \left[ \exp\left(\frac{qV}{kT}\right) - 1 \right] \quad (2.4.5)$$

where  $J_{R,0} = q\langle\beta_R\rangle n_i^2 d \exp(-E_g/kT)$ . If the dominating bulk recombination mechanism is bimolecular, the saturation current  $J_{R,0}$  is independent of the applied voltage. The functional form of Eq. (2.4.5) is in this case consistent with the standard diode equation Eq. (1.1.1), having a diode ideality factor  $\eta_{id} = 1$ .

On the other hand, if trap-assisted bulk recombination dominates,  $J_{R,0}$  generally depends on the applied voltage. Consider the case when trap-assisted recombination predominately takes place via deep gap states. Making use of the regional approximation, *i.e.* that electrons dominate at the cathode side of the active layer and holes at the anode side, we expect  $\beta_R \propto 1/n$  for  $x > d/2$  and  $\beta_R \propto 1/p$  for  $x < d/2$ , in accordance with Eq. (1.3.25). Then, with the carrier densities given by  $n(x) = n_{cat} \exp(qF[d-x]/kT)$  and  $p(x) = p_{an} \exp(qFx/kT)$ , it follows that<sup>7</sup>  $J_{R,0} \propto \exp(-qV/2kT)$  for  $V$  well

---

<sup>7</sup>As per the regional approximation [98], the voltage dependence of  $J_{R,0} = q\langle\beta_R\rangle n_i^2 d$  is given via

$$\langle\beta_R\rangle \propto \frac{1}{d} \left[ \int_{d/2}^d \frac{dx}{n(x)} + \int_0^{d/2} \frac{dx}{p(x)} \right] \propto \frac{kT}{q[V_{bi} - V]} \left[ \exp\left(\frac{q[V_{bi} - V]}{2kT}\right) - 1 \right],$$

below  $V_{bi}$  [11, 98]. Consequently, a principal voltage dependence of the form

$$J(V) \propto \sinh\left(\frac{qV}{2kT}\right) \sim \exp\left(\frac{qV}{2kT}\right) \quad (2.4.6)$$

is expected in the forward bias, corresponding to a diode ideality factor being close to 2 (for  $qV > kT$ ). For a general bulk recombination rate of the recombination order  $\delta$  for free carriers ( $R \propto n^\delta$ ), the voltage dependence of the current in the forward bias follows a diode ideality factor of  $\eta_{id} \approx 2/\delta$  [99]. It should be noted, however, that because of shunt and series resistances, an accurate determination of the diode ideality factor from the dark  $J$ - $V$  curve might be challenging [100, 101].

#### 2.4.2 The case when surface recombination dominates

Also accounting for the surface recombination current, constituting injected carriers that make it to the collecting contact, the total current for  $V < V_{bi}$  may be generally expressed as

$$J(V) = J_0(V) \left[ \exp\left(\frac{qV}{kT}\right) - 1 \right], \quad (2.4.7)$$

where  $J_0(V) = J_{R,0}(V) + J_{S,0}(V)$  is the sum of the contributions of both bulk and surface recombination to the total dark saturation current.

For conditions when the recombination taking place within the bulk is negligible ( $R = 0$ ), we have  $J_{R,0} \ll J_{S,0}$ . This type of situation might occur for thin active layers and/or large mobilities, when carriers have a large probability to traverse the active layer without recombining within the bulk. Under these circumstances, the individual hole and electron currents are constants of  $x$  (since  $dJ_p/dx = dJ_n/dx = 0$ ), flowing in parallel with each other through the active layer:  $J = J_p(d) + J_n(0)$ . The associated dark saturation current is then given

---

when trap-assisted recombination via deep midgap traps is dominating and  $F$  is given by Eq. (2.1.8).

by

$$J_{S,0} = \frac{qv_p p_{cat}}{1 + v_p/S_p} + \frac{qv_n n_{an}}{1 + v_n/S_n}, \quad (2.4.8)$$

where  $v_p$  and  $v_n$  are the effective transport velocities for holes and electrons, respectively, associated with diffusion of carriers within the active layer. Here,  $v_p$  is given in accordance with Eq. (2.3.4). A completely analogous expression is valid for  $v_n$  (see Footnote 8). In case of hole (electron) collection at a neutral cathode (anode) contact, corresponding to the case considered in Section 2.3.2, one directly obtains  $v_{p(n)} \approx \mu_{p(n)} (V_{bi} - V) / d$ .

In case of ohmic collecting contacts, however, also the impact of the energy-level bending at the contacts needs to be considered. For holes collected at the cathode, the energy-level bending at the electron-ohmic cathode creates a steeper potential barrier at the contact, simultaneously reducing the opposing internal electric field inside the active layer; see Figure 2.10(b). An analogous situation applies for electrons collected at the hole-ohmic anode. In the non-degenerate limit, accounting for the impact of energy-level bending in Eq. (2.3.4) then reveals<sup>8</sup>

$$v_p \approx \frac{\mu_p kT}{q\lambda_{cat}}, \quad v_n \approx \frac{\mu_n kT}{q\lambda_{an}}, \quad (2.4.9)$$

where  $\lambda_{an} = \sqrt{2\varepsilon\varepsilon_0 kT/q^2 p_{an}}$  and  $\lambda_{cat} = \sqrt{2\varepsilon\varepsilon_0 kT/q^2 n_{cat}}$ . Accordingly, the saturation current is independent of both the applied voltage and the active layer thickness, the concomitant diode ideality factor  $\eta_{id} = 1$  in this case being the same as for bimolecular recombination.

---

<sup>8</sup>To account for the energy-level bending at the hole-ohmic contact,  $E_c(x)$  can be approximated by  $E_c(x) - E_{F,an} = \varphi_{n,an} - kT \ln[p_{an}/p(x)]$ , with  $p(x)$  given by Eq. (2.1.12) for  $V < V_{bi}$  and  $p(0) = p_{an}$  (see Section 2.1.3). The effective diffusion velocity for electrons can then be evaluated as

$$v_n \equiv \left[ \int_0^d \frac{q}{\mu_n kT} \exp\left(\frac{E_c(x) - E_{F,an} - \varphi_{n,an}}{kT}\right) dx \right]^{-1} \approx \frac{\mu_n kT}{q\lambda_{an}},$$

for  $B\sqrt{2n_0/p_{an}} \ll 1$ .

### 2.4.3 Space-charge-limited double-injection currents

At higher voltages, the number of injected electrons and holes eventually becomes large enough to perturb the electric field within the active layer. When this occurs, the drift component of the injected current start to dominate the transport inside the active layer, the current becoming limited by both space-charge effects and recombination.

Considering a MIM device (with an undoped active layer), the dominating recombination mechanism at high carrier concentrations is bimolecular:  $\beta_R = \beta$ . In the limit of strong recombination ( $\beta \gg \beta_L$ ), the injected carriers immediately recombine when they meet, forming two separate space-charge-limited regions inside the active layer: a hole-dominated region where  $J \approx J_p$  adjacent to the anode and an electron-dominated region with  $J \approx J_n$  on the cathode side (regional approximation). In the weak recombination regime ( $\beta \ll \beta_L$ ), in turn, the injected carriers instead form a charge-neutral plasma (injected-plasma limit); in this limit,  $n \approx p$  applies throughout the active layer. Provided that the series resistance of the external circuit is negligible and the contacts remain ohmic under these (high-injection) conditions, the drift-dominated double-injection current reads [91, 102]

$$J_{DOI} = \frac{9}{8} \varepsilon \varepsilon_0 \mu_R \frac{(V - V_{bi})^2}{d^3}, \quad (2.4.10)$$

where  $\mu_R$  is an effective SCLC mobility for double injection,<sup>9</sup> which takes the limiting values:

---

<sup>9</sup>The general solution for  $\mu_R$  as derived by Parmenter and Ruppel [91, 102], assuming drift-dominated transport, is

$$\mu_R = \frac{8\mu_n\mu_p}{9(\mu_n + \mu_p)} \frac{\beta_L}{\beta} \left[ \frac{\Gamma\left(\frac{3}{2}\nu_n + \frac{3}{2}\nu_p\right)}{\Gamma\left(\frac{3}{2}\nu_n\right)\Gamma\left(\frac{3}{2}\nu_p\right)} \right]^2 \left[ \frac{\Gamma(\nu_n)\Gamma(\nu_p)}{\Gamma(\nu_n + \nu_p)} \right]^3,$$

where  $\nu_n = \frac{2\mu_n}{(\mu_n + \mu_p)} \frac{\beta_L}{\beta}$ ,  $\nu_p = \frac{2\mu_p}{(\mu_n + \mu_p)} \frac{\beta_L}{\beta}$ , and  $\Gamma(s + 1) \equiv s!$  is the Gamma function.



$$\mu_R \approx \begin{cases} \mu_p + \mu_n & , \text{ for } \beta \gg \beta_L, \\ \sqrt{\frac{16\pi\beta_L}{\beta}} \mu_p \mu_n & , \text{ for } \beta \ll \beta_L, \end{cases} \quad (2.4.11)$$

for strong ( $\beta \gg \beta_L$ ) and weak bulk recombination ( $\beta \ll \beta_L$ ).

The above discussion is valid for the case when injected carriers are dominating in the active layer. We note, however, that under conditions when the active layer is doped, the active layer is initially charge-neutral at voltages  $V > V_{bi}$ , as discussed in Section 2.3.6. If the active layer is  $p$ -doped, the corresponding double-injection current in the presence of bimolecular recombination is given by [91]

$$J_{DOI} = \frac{8}{9} q \sqrt{\frac{(\mu_n + \mu_p) \mu_p \mu_n N_p}{\beta}} \frac{(V - V_{bi})^{3/2}}{d^2}. \quad (2.4.12)$$

At high-injection conditions, on the other hand, when the density of injected carriers exceeds the background doping concentration, the limiting case Eq. (2.4.10) is eventually approached. For a more detailed discussion, including the derivations of Eq. (2.4.10) and Eq. (2.4.12), see Ref. [91].

## CHAPTER 3

# Charge extraction by a linearly increasing voltage pulse

Current transient measurements are useful for gaining additional information of transport properties in semiconductor devices. A frequently used method for determining the mobility in organic thin-film devices is charge extraction by linearly increasing voltage (CELIV). In CELIV, one uses a linear ramp-up voltage pulse, applied in reverse bias, to extract photoinduced or dark (either doping-induced or injected) charge carriers. The applied voltage is given by

$$u(t) = \begin{cases} -At + V_{\text{off}} & \text{when } t \geq 0, \\ V_{\text{off}} & \text{when } t < 0. \end{cases} \quad (3.0.1)$$

Here,  $V_{\text{off}}$  is the applied offset (dc) voltage and  $A = u_{\text{max}}/t_{\text{pulse}}$  is the voltage rise speed of the transient voltage pulse with amplitude  $u_{\text{max}}$  and pulse length  $t_{\text{pulse}}$ . From the transient features and the characteristic time scales of the corresponding extraction current transients, the mobility can be calculated.

The standard CELIV theory used for extracting the mobility neglects the influence of the contacts. In sandwich-type thin-film devices, this might lead to severe errors in the mobility determination. In this chapter, the basic CELIV

theory is extended to account for contact effects, such as the presence of a built-in voltage and carrier diffusion from the contacts. Apart from providing a correction for the mobility determination, we also show how the extended CELIV theory can be used to determine the doping concentration, the built-in voltage and the surface recombination velocity.

### 3.1 Basic theory

We start by reviewing the basic theory used for the mobility determination in CELIV. The active layer is assumed to contain uniform distributions of charge carriers. In general, these charges can either be photogenerated, doping-induced or injected from the contacts. Prior to the voltage pulse ( $t < 0$ ), the sample is held at flat-band (or open-circuit) conditions ( $V_{\text{off}} = V_{bi}$ ) and the active layer is assumed electrically neutral with  $p = n$ . Upon applying the ramp-up voltage pulse, charge carriers are subsequently extracted as a uniformly moving sheet; the extraction current transient for  $t \geq 0$  becomes [103, 104]

$$j(t) = j_0 + \Delta j(t), \quad (3.1.1)$$

where  $j_0 = -\varepsilon\varepsilon_0 A/d$  is the average displacement current and  $\Delta j(t)$  is the average conduction current. A schematic picture is shown in Figure 3.1. Neglecting diffusion,

$$\Delta j(t) = \frac{1}{d} \left[ \int_{l_n(t)}^d q\mu_n n F dx + \int_0^{d-l_p(t)} q\mu_p n F dx \right], \quad (3.1.2)$$

where  $l_n(t)$  and  $l_p(t)$  is the extraction depth for electrons and holes, respectively.

#### 3.1.1 Low-conductivity regime

The extraction current in Eq. (3.1.2) is generally dominated by the faster carrier type. In this case, the extraction depth is related to the electric field *within* the

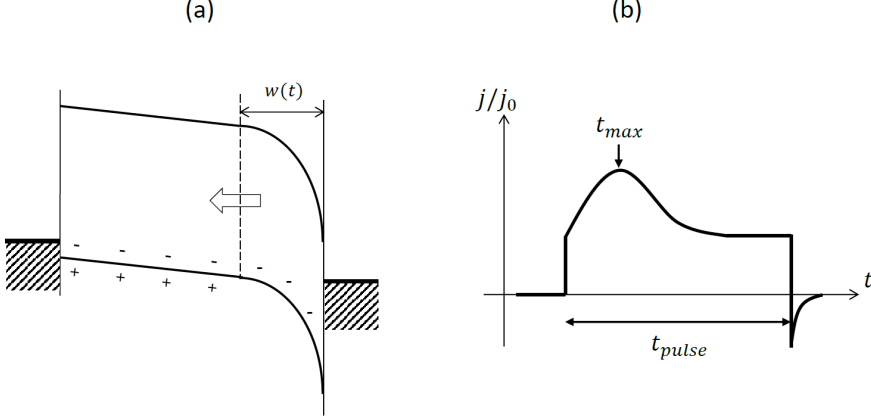


Figure 3.1: Schematic picture of CELIV. (a) The energy level diagram for the case when the charge extraction process is dominated by holes. Upon applying the reversely-biased ramp-up voltage pulse, holes are extracted at the anode, leaving a space-charge region of electrons behind in the active layer. (b) The corresponding extraction current transient  $j(t)$ , normalized to the geometric capacitive current response  $j_0$ . The length of the voltage pulse, applied at  $t = 0$ , is  $t_{pulse}$ .

quasi-neutral region via  $dw/dt = -\mu F$ , where  $\mu$  and  $w$  is the mobility and the extraction depth, respectively, of the faster charge carriers. If space-charge effects are negligible, the extracting electric field is given by  $F = -At/d$ . The average conduction current density Eq. (3.1.2) then simplifies as

$$\frac{\Delta j(t)}{j_0} = \frac{qn\mu t}{\varepsilon\varepsilon_0} \left[ 1 - \frac{t^2}{t_{tr}^2} \right], \quad (3.1.3)$$

for  $0 \leq t \leq t_{tr}$  where  $t_{tr} \equiv \sqrt{2d^2/\mu A}$  is the transit time for the carriers. The mobility can be calculated from the time  $t_{max}$  where the extraction current  $\Delta j(t)/j_0$  has its maximum [103],

$$\mu = \frac{2d^2}{3At_{max}^2}. \quad (3.1.4)$$

The regime of negligible space-charge effects is valid for low carrier concentrations ( $\Delta j(t) \ll j_0$ ), referred to as the low-conductivity regime. It should be noted that, in general, both carrier types contribute to the extracted current, with  $\mu$  being a combination of both carrier mobilities; accounting for both carrier types, the extracted mobility  $\mu$  in Eq. (3.1.4) actually corresponds to  $\mu = (\mu_n^2 + \mu_p^2) / (\mu_n + \mu_p)$ .

### 3.1.2 Moderate-conductivity regime; the impact of space charge

The general assumption in CELIV is that the charge species with the lower mobility is effectively immobile during the extraction process ( $\mu_{fast} \gg \mu_{slow}$ ). Under these conditions, the extraction of the faster carrier will leave a depleted layer of thickness  $w(t)$  of the immobile charges behind within the active layer. If we assume the faster carriers to be holes, the net charge density is then given by

$$\rho_{sc}(x, t) = \begin{cases} -qn & \text{if } d - w \leq x < d, \\ 0 & \text{otherwise,} \end{cases} \quad (3.1.5)$$

reducing the electric field within the neutral (non-depleted) region.<sup>10</sup> Hence,

$$\frac{dw}{dt} = -\mu F(0, t) = \mu \left[ \frac{At}{d} - \frac{qnw^2}{2\varepsilon\varepsilon_0 d} \right], \quad (3.1.6)$$

with the condition  $w(0) = 0$  [103]. Note that the low-conductivity regime applies in the limit when the electric field is changing much faster than the field redistribution due to the space charge, corresponding to  $t_{tr} \ll \varepsilon\varepsilon_0/qn\mu$  (space-charge effects become negligible).

---

<sup>10</sup>The electric field is explicitly obtain by integrating Gauss law, Eq. (1.3.4), as

$$F(x, t) = \begin{cases} F(0, t) + \frac{qn}{\varepsilon\varepsilon_0} (d - w - x) & \text{if } d - w \leq x < d, \\ F(0, t) & \text{, else .} \end{cases}$$

Eq. (3.1.6) is then obtained after making use of  $-At = \int_0^d F(x, t) dx$ .

At moderate conductivities when  $t_{tr} \sim \varepsilon\varepsilon_0/qn\mu$ , however, the space-charge term in Eq. (3.1.6) becomes significant, resulting in a reduced extraction rate of the charge carriers. The net effect of this is to shift  $t_{max}$  to earlier times, relative to Eq. (3.1.4). Unfortunately, the general solution to Eq. (3.1.6) is not analytically tractable.<sup>11</sup> Based on numerical simulations, however, Juška *et al.* obtained [104, 105]

$$\mu = \frac{2d^2}{3At_{max}^2}K, \quad (3.1.7)$$

where  $K = [1 + \chi\Delta j_{max}/j_0]^{-1}$ , with  $\chi$  being a numerical correction factor that takes the field redistribution into account and  $\Delta j_{max} \equiv \Delta j(t_{max})$ . Juška *et al.* initially proposed  $\chi = 0.36$ . The accuracy of this correction factor was later improved by other groups [106–108]; an excellent account on this topic is given by Lorrmann *et al.* [108]. Note that in the limit  $\Delta j_{max}/j_0 \ll 1$ ,  $K \rightarrow 1$  and the low-conductivity regime is reobtained.

### 3.1.3 Influence of bulk recombination

In the derivation of Eq. (3.1.4) and Eq. (3.1.7), recombination between carriers inside the active layer was neglected. In case of extraction of photoinduced carriers, however, this mechanism becomes important. The effect of bulk recombination is to decrease the carrier density during the extraction process, resulting in an additional time dependence in the extraction current [107, 109, 110]. For a bimolecular recombination rate  $dn/dt = -\beta n^2$ , the carrier density

---

<sup>11</sup>The solution to Eq. (3.1.6), with the boundary condition  $w(0) = 0$ , is given by [108]

$$w(t) = 2d \left( \frac{\tau_\sigma}{t_{tr}} \right)^{2/3} \frac{\sqrt{3}Ai' \left( t/\sqrt[3]{\tau_\sigma t_{tr}^2} \right) + Bi' \left( t/\sqrt[3]{\tau_\sigma t_{tr}^2} \right)}{\sqrt{3}Ai \left( t/\sqrt[3]{\tau_\sigma t_{tr}^2} \right) + Bi \left( t/\sqrt[3]{\tau_\sigma t_{tr}^2} \right)},$$

where  $\tau_\sigma = \varepsilon\varepsilon_0/qn\mu$ . Here,  $Ai(u)$  ( $Bi(u)$ ) is the Airy function of the first (second) kind, with  $Ai'(u)$  ( $Bi'(u)$ ) being the respective derivative.

varies with time as

$$n(t) = \frac{n_*}{1 + \beta n_* [t + t_{del}]} = \frac{n(0)}{1 + \beta n(0) t}, \quad (3.1.8)$$

for carriers with an initial density  $n_*$  at  $t = -t_{del}$ , where  $t_{del}$  is the delay time.

Now, if we take space-charge effects to be negligible during the extraction process (*i.e.* the current is given by Eq. (3.1.3)) and assume a time dependence of  $n(t)$  given by Eq. (3.1.8), a relation between  $t_{max}$  and the recombination coefficient  $\beta$  can be established; we find

$$t_{max}^2(\beta) = t_{max}^2(0) \left[ 1 - \frac{\beta \Delta j_{max}}{\beta_L j_0} \right], \quad (3.1.9)$$

where  $\Delta j_{max}$  depends on  $\beta$  and  $n(0)$  (and thus also on  $t_{del}$ ), and  $\beta_L = q\mu/\varepsilon\varepsilon_0$ . The presented analytical approximation [Eq. (3.1.9)] agrees well with numerical simulations by Bange *et al.* [107] for  $\Delta j_{max}/j_0 \ll 1$ , as demonstrated in Figure 3.2. However, a good agreement is also found at moderate  $\Delta j_{max}/j_0$ . Hence, in accordance with Eq. (3.1.9), the mobility is then obtained from

$$\mu \approx K \frac{2d^2}{3At_{max}^2} \left[ 1 - \frac{\beta \Delta j_{max}}{\beta_L j_0} \right]. \quad (3.1.10)$$

For small  $\beta/\beta_L$ , the carrier density changes negligibly during the extraction process. On the other hand, at high carrier concentrations or large  $\beta/\beta_L$ , the recombination sets an upper limit for the extraction current given by

$$\frac{\Delta j_{max}}{j_0} \approx \frac{\beta_L}{\beta}, \quad (3.1.11)$$

as previously pointed out by Juška and co-workers [110, 111]. This upper limit can be used to estimate the bimolecular recombination coefficient  $\beta$ . We note that analogous expressions can also be obtained for monomolecular recombination.<sup>12</sup>

---

<sup>12</sup>In case of monomolecular recombination of carriers ( $dn/dt = -n/\tau$ ) with the lifetime  $\tau$ ,

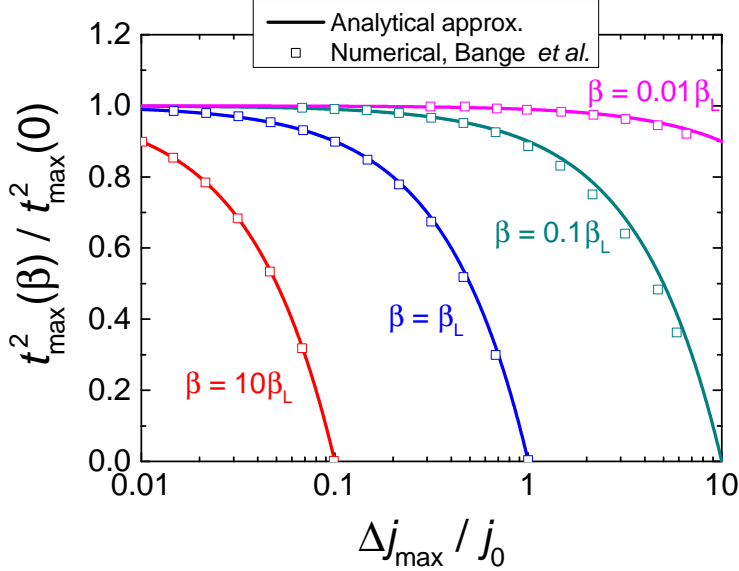


Figure 3.2: The effect of bimolecular recombination on the current transient maximum  $t_{max}(\beta)$  for different recombination coefficients. The symbols correspond to numerical data by Bange *et al.* [107], whereas the analytical approximations *as per* Eq. (3.1.9) are indicated by the solid lines. Here,  $t_{max}(0)$  corresponds to the case without recombination (Eq. (3.1.7)).

### 3.1.4 Non-uniform carrier distributions

The above considerations all assume that the carrier concentrations are uniform throughout the active layer at the application of the pulse. This implies either a doped semiconductor layer, or a uniform photogeneration of carriers prior to the

---

we instead have  $n(t) \propto \exp(-t/\tau)$ ; an analogous treatment then yields for the mobility

$$\mu = \frac{2d^2}{At_{max}^2} \left[ \frac{\tau - t_{max}}{3\tau - t_{max}} \right].$$

For large  $\tau$ , this relation reduces back to Eq. (3.1.3), whereas in the limit of short lifetimes ( $\tau \ll t_{tr}$ ),  $t_{max} \rightarrow \tau$ .



pulse. In case of non-uniform distributions the above mobility formulas are no longer valid. For example, in the case of non-uniform absorption encountered in optically thick layers, the mobility determination becomes strongly dependent on the absorption coefficient of the film [112].

In dark, on the other hand, thin-film diodes based on organic semiconductors are inherently undoped, behaving as MIM devices with exponential distributions of injected carriers (from the contacts); see Section 2.1.2. At low steady-state voltages,  $0 < V_{\text{off}} < V_{bi}$ , the injected hole density is to a good approximation given by

$$p(x) = p(0) \exp\left(-\frac{q[V_{bi} - V_{\text{off}}]x}{kTd}\right). \quad (3.1.12)$$

At these offset voltages, the drift current is closely balanced by diffusion prior to the application of the extracting voltage pulse. In case of an injected carrier distribution Eq. (3.1.12), the mobility can be calculated from [Paper 1]

$$\mu = \frac{kTd^2}{[V_{bi} - V_{\text{off}}]qAt_{max}^2}, \quad (3.1.13)$$

at large voltage rise speeds ( $At_{max} \gg kT/q$ ). In this case,  $t_{max}$  depends on the potential difference prior to the pulse via  $t_{max}^{-2} \propto (V_{bi} - V_{\text{off}})$ . As a result,  $V_{bi}$  can be estimated from a  $t_{max}^{-2}$  vs.  $V_{\text{off}}$  plot by extrapolating to the applied offset voltage at which the measured  $t_{max}^{-2}$  crosses the  $V_{\text{off}}$ -axis [Paper 1].

## 3.2 CELIV on doped samples; the impact of the built-in voltage

In the derivation of Eq. (3.1.6), following the treatment by Juška *et al.* [103], the presence of a built-in voltage was neglected. If the charge carriers are doping-induced, the effect of the built-in voltage can no longer be neglected. Consider a  $p$ -doped active layer with a doping concentration  $p = N_p$  (see Section

2.3.6). In this case, the extraction is dominated by holes, whereas electrons are immobilized (in ionized dopant levels). Taking the effect of the built-in voltage into account, Eq. (3.1.6) is modified as

$$\frac{dw(t)}{dt} = \frac{\mu At}{d} - \frac{q\mu N_p}{2\varepsilon\varepsilon_0 d} \left[ w(t)^2 - w_0^2 \right] \quad (3.2.1)$$

as shown in [**Paper II**], where  $w(0) = w_0$  is given by

$$w_0 = \sqrt{\frac{2\varepsilon\varepsilon_0}{qN_p} \left[ V_{bi} - V_{off} - \frac{kT}{q} \right]}, \quad (3.2.2)$$

being the familiar steady-state depletion region thickness from Section 2.3.6. Analytical approximations to Eq. (3.2.1) are readily obtained in the following two regimes, depending on the voltage rise speed  $A$ .

### 3.2.1 The transport-limited regime

In the  $A \rightarrow \infty$ -limit ( $\Delta j \ll j_0$ ), Eq. (3.2.1) is simplified as  $dw(t)/dt \approx \mu At/d$ , being otherwise identical to the low-conductivity limit in Section 3.1.1, but now a part of the carriers within the device has already been extracted prior to the pulse and  $w(0) \neq 0$ . Solving for  $w(t)$  and inserting into  $\Delta j(t)$ , one then finds  $\mu = 2[d^2 - dw_0]/3At_{max}^2$ . This expression differs from Eq. (3.1.4) by a factor of  $[1 - w_0/d]$ , which represents the correction due to the presence of a steady-state depletion region. For moderate conductivities ( $\Delta j \sim j_0$ ), we correspondingly find [**Paper II**]

$$\mu = \frac{2d^2}{3At_{max}^2} \left[ 1 - \frac{w_0}{d} \right] K, \quad (3.2.3)$$

in analogy with Eq. (3.1.7). Consequently, the effect of  $V_{bi}$  and  $w_0$  is to reduce  $t_{max}$ , leading to an overestimation of the mobility if Eq. (3.1.7) is used in this case. Eq. (3.2.3) is valid as long as the current transient is transport-limited,  $j(t_{max}) \ll \varepsilon\varepsilon_0 A/w_0$ .

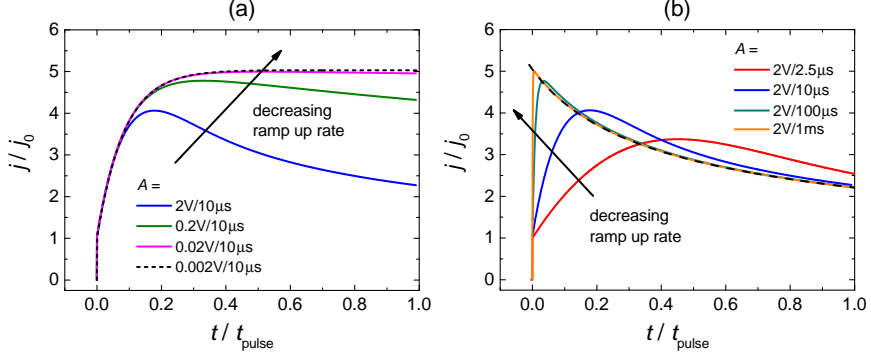


Figure 3.3: The transition from a transport-limited regime to a doping-induced capacitive regime is simulated at varying voltage rise speeds  $A = u_{\text{max}}/t_{\text{pulse}}$ . The extraction current transients becomes capacitive either by (a) decreasing the amplitude  $u_{\text{max}}$  or (b) increasing the duration  $t_{\text{pulse}}$  of the voltage pulse. The analytical expression Eq. (3.2.7) is indicated by the dashed line in (b).

### 3.2.2 The capacitive regime

Figure 3.3 shows simulated CELIV current transients of a  $p$ -doped device at different ramp-up rates  $A$ . In the limit of small  $A$ , corresponding to slowly changing voltage pulses, a saturation of the current transients is seen. In this limit, the current transients are limited by the capacitance of the depletion layer. Depending on the amplitude and pulse length of the voltage pulse, one of the following two situations may arise.

#### Low amplitudes, $t_{\text{pulse}} \ll t_{\text{max}}$

At low amplitudes  $u_{\text{max}}$  of the applied voltage pulse, or high doping concentrations, the change  $\Delta w = w - w_0$  in the depletion layer becomes negligibly small during the pulse. In the limit  $\Delta w(t) \ll w_0$ , Eq. (3.2.1) approximates as

$$\frac{d}{dt}[\Delta w] \approx \frac{\mu A t}{d} - \frac{q N_p \mu w_0}{\varepsilon \varepsilon_0 d} \Delta w. \quad (3.2.4)$$

Solving Eq. (3.2.4) reveals for the extraction current transient [Paper 2]

$$j(t) = j_0 + j_0 \left[ \frac{d}{w_0} - 1 \right] \left[ 1 - \exp \left( -\frac{w_0 t}{d\tau_\sigma} \right) \right], \quad (3.2.5)$$

where  $\tau_\sigma = \varepsilon\varepsilon_0/qN_p\mu$  is the dielectric relaxation time. At  $t \gg \tau_\sigma$ , the current saturates to  $j(t)/j_0 \rightarrow C_w/C_{geo}$ , where  $C_w = \varepsilon\varepsilon_0/w_0$  is the steady-state depletion-layer capacitance (prior to the pulse). Here,  $C_{geo} = \varepsilon\varepsilon_0/d$  is the geometric capacitance. Concomitantly, the extraction current transient at low amplitudes is limited by the charging current of the steady-state depletion layer, with the quasi-neutral region virtually acting as an extension of the contact. A distinguishing feature of this current regime is that  $j(t)/j_0$  becomes independent of the amplitude for a fixed  $t_{pulse}$  (see Figure 3.3(a)).

### Long pulses, $t_{pulse} \gg t_{max}$

At large  $t_{pulse}$ , when the voltage pulse length is long enough for the electric field to have time to redistribute ( $t \gg \tau_\sigma$ ), a perpetual screening of the field inside the quasi-neutral region is taking place during the extraction pulse ( $F \approx 0$ ). In this situation, the  $dw/dt$  term in Eq. (3.2.1) becomes negligibly small compared to the other terms, and the extraction depth can directly be evaluated as

$$w(t) = \sqrt{\frac{2\varepsilon\varepsilon_0}{qN_p} \left[ At + V_{bi} - V_{off} - \frac{kT}{q} \right]}. \quad (3.2.6)$$

The total extraction current transient at slow pulses is subsequently obtained as [Paper II]

$$j(t) = \frac{\varepsilon\varepsilon_0 A}{w}, \quad (3.2.7)$$

with  $w$  given by Eq. (3.2.6). As a result, the extraction current transient becomes limited by the displacement current of depletion layer at slow pulses. A characteristic feature of current transients in the slow-pulse capacitive regime

is that  $j(t)/j_0$  becomes independent of  $t_{pulse}$  (when keeping the amplitude fixed) and depends only on the applied transient voltage (see Figure 3.3(b)).

### 3.2.3 Using CELIV to measure the built-in voltage and the doping concentration

At slow pulses, the extraction current transient is directly proportional to the depletion-layer capacitance. In this case, the extraction current transient can be used to directly obtain the depletion-layer capacitance as

$$C_w = \frac{j}{A} = \left( \frac{j}{j_0} \right) C_{geo}, \quad (3.2.8)$$

at the applied voltage  $u(t) = -At + V_{off}$ , where  $j$  is given by Eq. (3.2.7). When plotting the transient current as function of  $u(t)$  in this regime, the voltage dependence of the depletion-layer capacitance can be mapped. From the voltage dependence of the inverse square of the depletion capacitance ( $1/C_w^2$ ), referred to as a Mott-Schottky plot [15, 97], the doping concentration and the built-in voltage can be estimated. In terms of the normalized current transient  $j/j_0$ , we can write

$$\left( \frac{j}{j_0} \right)^{-2} = \frac{2\varepsilon\varepsilon_0}{qN_p d^2} \left[ V_{bi} - \frac{kT}{q} - u(t) \right], \quad (3.2.9)$$

for  $w < d$ . From the slope and the intercept with the  $u(t)$ -axis, respectively, the doping concentration and built-in voltage can be extracted. Note that it is the (effective) built-in voltage over the depletion region (see Fig. 2.8(b)) which is extracted in this case. An experimental demonstration of this method, referred to as CELIV in the doping-induced capacitive regime (doping-CELIV), is shown in Figure 3.4 on a  $p$ -doped P3HT:PCBM device. The method can also be used to extract the doping profile, as demonstrated by Nyman *et al.* [Paper 3].

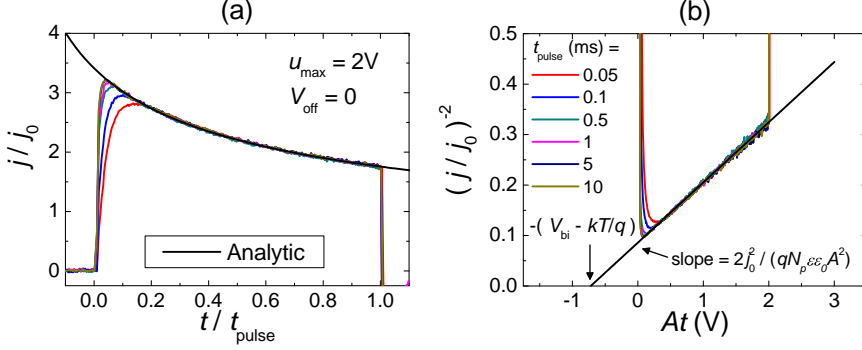


Figure 3.4: The doping-CELIV method. (a) Experimental extraction current transients at different voltage pulse lengths  $t_{\text{pulse}}$  on a p-doped P3HT:PCBM device. The voltage amplitude is kept fixed at  $u_{\text{max}} = 2\text{ V}$  and the offset voltage is zero. (b) The corresponding Mott-Schottky plots,  $(j/j_0)^{-2}$  vs.  $At$ , of the normalized extraction current transients. The device structure is ITO/MoO<sub>3</sub>/P3HT:PCBM/LiF/Al, the experimental details are given in [Paper II].

### 3.3 Extraction of carriers injected into structures with blocking contacts

In an intrinsic semiconductor, the number of dark charge carriers in a single-carrier structure is inherently very low at small offset voltages. However, if the cathode contact is blocking, a significant charge reservoir of holes (injected from the anode) can be created at the cathode for  $V_{\text{off}} > V_{\text{bi}}$ . Juška and co-workers showed that at large enough offset voltages, the subsequent CELIV extraction current transient of the injected carrier reservoir becomes space-charge-limited, allowing for the mobility to be calculated [113, 114]. The blocking contact is realized by introducing a thin wide-bandgap insulating layer between the electrode and the semiconductor, thus forming a metal-insulator-semiconductor (MIS) configuration. This is the basic idea behind the charge extraction of injected carriers by linearly increasing voltage in MIS structures, typically referred to as MIS-CELIV or i-CELIV [114, 115].

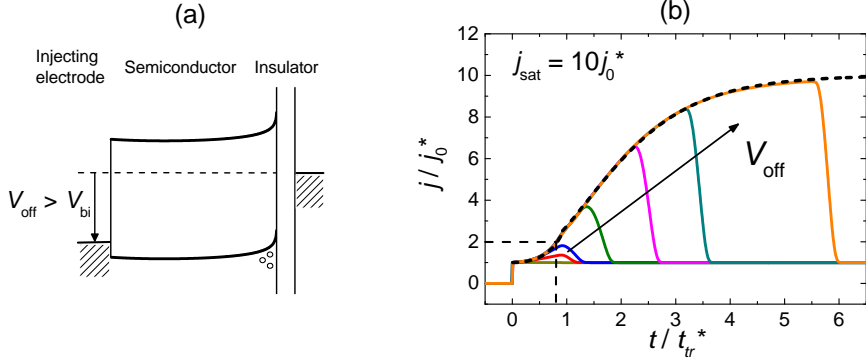


Figure 3.5: Schematic picture of MIS-CELIV, where the cathode contact has been made blocking by covering the cathode with a thin insulator layer. (a) At a large enough offset voltage  $V_{\text{off}} > V_{bi}$ , an injected charge-carrier reservoir can be created at the blocking contact during dc conditions (prior to the CELIV pulse). (b) The subsequent extraction of these injected carriers ideally result in space-charge limited extraction current transients (dashed lines).

### 3.3.1 Space-charge-limited extraction current transients

Consider a hole-only device structure with a hole-injecting anode and a blocking wide-bandgap insulator at the cathode. The insulator layer, with the dielectric constant  $\varepsilon_i$  and thickness  $d_i$ , is assumed to be perfectly blocking ( $S_p = 0$ ). By applying a large offset voltage that injects holes from the anode, an accumulation of charge carriers can be created at the insulator-semiconductor interface. At dc conditions, the current is identically zero across the semiconductor (equilibrium). Upon applying the extraction pulse, the total extraction current transient is obtained as [Paper III]:

$$j(t) = j_0^* + \Delta j^*(t), \quad (3.3.1)$$

where  $j_0^* \equiv -C_{geo}^* A$  and  $\Delta j^*(t)$  are the effective average displacement and conduction currents, respectively, for the semiconductor-insulator system, and  $C_{geo}^* = [d_s/\varepsilon_0\varepsilon_s + d_i/\varepsilon_0\varepsilon_i]^{-1}$  is the total geometric capacitance. A schematic picture of MIS-CELIV is shown in Figure 3.5.

Provided that a large enough offset voltage is applied for a charge reservoir to be formed, the corresponding extraction current transient is space-charge-limited. Under the following simplifying assumptions that i) diffusion is negligible (large extracting electric field), and ii) that the concentration inside the semiconductor is small (all carriers are concentrated at the insulator interface) the space-charge-limited extraction current transient for  $0 \leq t \leq t_{sc}$  is given by

$$j(t) = j_0^* \left[ 1 + \tan^2 \left( \frac{t}{t_{tr}^* \sqrt{1+f}} \right) \right], \quad (3.3.2)$$

where  $t_{tr}^* = d_s \sqrt{2(1+f)/\mu A}$  is the small-charge transit time,  $t_{sc} \approx 0.92t_{tr}$  is the arrival time of the initial front of carriers at the extracting contact, and  $f \equiv \varepsilon_s d_i / \varepsilon_i d_s$  is the ratio between the individual geometric capacitances of the semiconductor and the insulator. The mobility can be extracted using the relation

$$\mu = \frac{\pi^2 d_s^2}{8A^* t_1^2} (1+f), \quad (3.3.3)$$

where  $t_1$  is the time at which  $j(t_1) = 2j_0^*$ , and  $A^* \equiv A/(1+f)$ . At larger times  $t > t_{sc}$ , the extraction current transient approaches

$$j(t) = j_0^* + [j_{sat} - j_0^*] \tanh^2 \left( \frac{3t}{2t_{tr}^*} \sqrt{\frac{j_0^*}{j_{sat}}} \right), \quad (3.3.4)$$

where  $j_{sat} = \varepsilon_i \varepsilon_0 A / d_i$  is the saturation current due to the displacement current



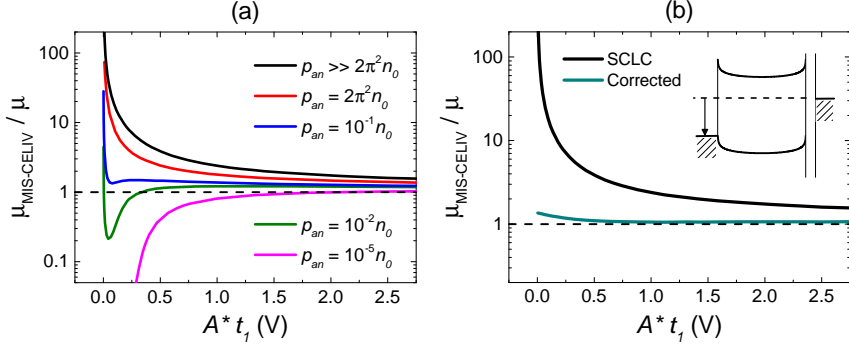


Figure 3.6: The MIS-CELIV mobilities, extracted using the original MIS-CELIV formula Eq. (3.3.3), as obtained from simulated MIS-CELIV extraction current transients at different hole-injecting contacts. The extracted MIS-CELIV mobilities are normalized to the input mobility. It can be seen that when the injecting contact is ohmic ( $p_{an} \gg 2\pi^2 n_0$ ), a severe overestimation of the mobility might occur, depending on the extracting transient voltage  $A^* t_1$ . At moderate barriers at the injecting contact, a better agreement is found. The corresponding barriers at the hole-injecting contacts are 0.27 eV ( $2\pi^2 n_0$ ), 0.41 eV ( $10^{-1} n_0$ ), 0.47 eV ( $10^{-2} n_0$ ), and 0.65 eV ( $10^{-5} n_0$ ). In (b), the extracted MIS-CELIV mobility in case of ohmic contacts, using Eq. (3.3.3) (SCLC) is compared to Eq. (3.3.6) (corrected) that accounts for the ohmic diffusion current at small  $A^* t_1$ .

of the insulator. A necessary condition for Eq. (3.3.3) to be valid is  $j_{sat} > 3.3j_0^*$  [115]. The analytical derivation of Eq. (3.3.2) and Eq. (3.3.4) are detailed in the supplementary material of [Paper III].

### 3.3.2 Effect of diffusion in thin-film devices

In thin-film devices, the above two simplifying assumptions i) and ii) made in the derivation of the space-charge-limited extraction current transient are generally only valid in the limit of large extracting electric fields. Moreover, at small  $A^* t$ , the shape of the extraction current transient is also strongly dependent on the properties of the injecting contact, which might result in large errors in the mobility determination [Paper III]. The situation is illustrated in Figure 3.6.

In case of an ohmic injecting contact, the carrier density inside the active layer at large offset voltages is identical to the case with two symmetric ohmic contacts and given by Eq. (2.1.14), with the large charge accumulation at the insulator interface behaving like a reservoir-type contact under the SCLC extraction process. As a consequence, a non-negligible amount of carriers is present inside the semiconductor layer under dc conditions. During the extraction process, these carriers induce an additional ohmic current regime (see Eq. (2.3.11)),

$$\Delta j^*(t) \approx -\frac{4\pi^2 \varepsilon_s \varepsilon_0 kT \mu A^* t}{q d_s^3}, \quad (3.3.5)$$

which dominates over the SCLC transient response at small  $A^* t_1$  [**Paper III**]. This current contribution give rise to an apparent shift of  $t_1$  to earlier time scales, with Eq. (3.3.3) overestimating the mobility under these conditions. However, the deviation caused by the diffusion-induced ohmic current regime can be taken into account by introducing a correction factor that modifies the mobility expression as [**Paper III**]

$$\mu = \frac{\pi^2 d_s^2}{8 A^* t_1^2} \frac{(1 + f)}{\left[1 + \frac{\pi^4 kT}{2q A^* t_1}\right]}. \quad (3.3.6)$$

For large  $A^* t_1$ , the original mobility formula Eq. (3.3.3) is reobtained, as expected.

### 3.3.3 Using CELIV to measure surface recombination velocity at blocking contacts

Charge extraction by linearly increasing voltage can also be used to quantify the injected charge accumulating within the active layer. For a hole-only structure, the extracted charge is related to the carrier density distribution within the

active layer in accordance with [116]

$$Q_{\text{extr}} \equiv \int_0^{t_{\text{extr}}} \Delta j(t) dt = \int_0^{t_{\text{extr}}} J dt - \frac{q}{d} \int_0^d \left[ \int_x^d p(x', 0) dx' \right] dx, \quad (3.3.7)$$

where the hole-extracting contact is located at  $x = 0$  and  $t_{\text{extr}}$  is the time at which the injected holes have been extracted. As demonstrated in Section 2.3.7, the bias-induced charge reservoir at a blocking contact is directly related to the associated (effective) surface recombination velocity  $S_p$  for voltages  $V_{\text{off}} > V_{bi}$ . Provided that the magnitude of the dc current  $J(V_{\text{off}})$  is small compared to the magnitude of transient current response  $\Delta j(t)$ , we find for  $\lambda \ll d$  that  $|Q_{\text{extr}}| \approx |\Delta Q|$ , where  $\Delta Q$  is given by Eq. (2.3.17) [**Paper I**].<sup>13</sup> The surface recombination velocity can then be calculated from

$$S_p = \frac{2\varepsilon\varepsilon_0 kT}{qQ_{\text{extr}}^2} J_D \times \eta, \quad (3.3.8)$$

where  $J_D = J(V_{\text{off}})$ . Hence, by measuring the extracted charge and dc current density at different offset voltages  $V_{\text{off}} > V_{bi}$ , the associated surface recombination velocity at the blocking contact can be estimated. Here,  $\eta$  is a correction factor that takes DOS filling effects for the accumulated carriers into account; in the non-degenerate limit  $\eta = 1$ . At very large carrier concentrations, however,  $\eta$  deviates from unity. For a Gaussian distribution of states, the correction factor can be numerically approximated as  $\eta \approx 1/\text{erf}\left([- \ln(c)]^{2/3} kT/\sigma\right)$  for  $c \leq 0.1$ , where  $c = p(d)/N_0$  at the blocking contact ( $x = d$ ) [**Paper I**].

---

<sup>13</sup>If  $p_{cat}$  at the blocking contact is large, a large charge carrier reservoir may already be present at  $V_{\text{off}} = 0$ . In this case, Eq. (3.3.8) is to be replaced by:

$$S_p = \frac{J(V_{\text{off}})}{q} \left[ \frac{Q_{\text{extr}}^2(V_{\text{off}})}{2\varepsilon\varepsilon_0 kT} - p_{cat} \right]^{-1} = \frac{2\varepsilon\varepsilon_0 kT}{q [Q_{\text{extr}}^2(V_{\text{off}}) - Q_{\text{extr}}^2(0)]} J(V_{\text{off}}),$$

where  $Q_{\text{extr}}(0) = \sqrt{2\varepsilon\varepsilon_0 kT p_{cat}}$  is the accumulated charge at  $V_{\text{off}} = 0$ .

## CHAPTER 4

# Charge collection and the effect of contacts in organic thin-film solar cells

An important application of sandwich-type thin-film diodes is within the area of thin-film solar cells. The general principle of solar cells is based on utilizing the built-in asymmetry of the semiconductor diode structure to extract charge carriers generated by sunlight. In conventional (high-mobility) solar cells, based on  $p$ - $n$  junctions made of crystalline silicon, the built-in asymmetry is mainly provided by charge selectivity. In thin-film organic solar cells, based on low-mobility semiconductors, however, a different situation applies. The charge collection in organic solar cells has generally been analyzed in accordance with the MIM model. However, the charge collection in these devices is also sensitive to doping-induced space-charge regions and surface recombination at the contacts. In this chapter, the interplay between charge transport, recombination, and contact properties in sandwich-type solar cells, based on low-mobility semiconductors with optically thin active layers, is investigated. The theoretical findings provide tools to identify and distinguish between various loss mechanisms in organic BHJ solar cells.

## 4.1 Charge transport and recombination in organic solar cells

The typical single-absorber layer organic solar cell structure constitute a light-absorbing active BHJ layer, typically a polymer-fullerene blend, which is sandwiched between a hole-collecting anode and an electron-collecting cathode. The total (steady-state) current density under illumination can generally be expressed as

$$J = -qGd + q \int_0^d \beta_R n_i^2 \left[ \exp \left( \frac{qV_{int}(x)}{kT} \right) - 1 \right] dx + J_n(0) + J_p(d), \quad (4.1.1)$$

where  $qV_{int}(x) = E_{Fn}(x) - E_{Fp}(x)$  is the quasi-Fermi level difference inside the active layer and  $G$  is the average photogeneration rate,  $qGd \equiv q \int_0^d G_L(x) dx$ . The active layer is assumed to be optically thin. The open-circuit conditions are reached at the voltage  $V = V_{oc}$  when the total current  $J = 0$ , corresponding to conditions when the total photogeneration is exactly balanced by (bulk and surface) recombination. Ideally, the contacts are selective, meaning that no carriers are extracted and/or injected at the wrong electrode (electrons at anode, holes at cathode); in this case, losses due to surface recombination (of the minority carriers) are absent and  $J_n(0) = J_p(d) = 0$ .

### 4.1.1 Negligible recombination between photoinduced carriers

Taking the contacts to be ideal in terms of charge-carrier selectivity and energy levels, all recombination occur within the bulk. Under conditions when photoinduced carriers are extracted fast enough, or have a low enough density, for the recombination between photogenerated carriers to be negligible compared to the recombination of the injected background carriers,  $J_R$  can be approximated by its corresponding dark current so that

$$J = -qGd + J_{R,0}(V) \left[ \exp \left( \frac{qV}{kT} \right) - 1 \right], \quad (4.1.2)$$

where  $J_{R,0}$  is the dark saturation current for bulk recombination (see Section 2.4.1). At short-circuit conditions, all photoinduced carriers are collected during operating solar cell conditions and the net photocurrent,  $J_{ph} = J_{illum} - J_{dark}$ , is saturated:  $J_{ph,sat} = -qGd$ . This situation is encountered in active layers with (relatively) high mobilities, or at low illumination levels when the recombination within the bulk is negligible.

In the ideal case, when external recombination channels (such as recombination via traps) are absent, the only loss mechanism is by direct bimolecular recombination inside the bulk. In this case, Eq. (4.1.2) simplifies as

$$J = -qGd + q\beta_R n_i^2 d \left[ \exp\left(\frac{qV}{kT}\right) - 1 \right]. \quad (4.1.3)$$

The open-circuit voltage ( $J(V_{oc}) = 0$ ), *i.e.* the voltage at which the photogeneration current is exactly balanced by the recombination current, is given by [51, 117, 118]

$$qV_{oc,max} = E_g - kT \ln \left( \frac{\beta_R N_c N_v}{G_{tot}} \right), \quad (4.1.4)$$

where  $G_{tot} = G + \beta_R n_i^2$ . This corresponds to the maximum attainable open-circuit voltage. Under normal illumination conditions, the external photogeneration rate ( $G$ ) is much larger than the thermal generation rate ( $\beta_R n_i^2$ ), and in the remainder of this work, we assume  $G_{tot} = G$ . Note that if  $\beta_R \propto \exp(\Delta E_{CT}/kT)$  (see Section 1.3.3), we obtain  $qV_{oc} \propto E_{CT}$ , where  $E_{CT}$  is the energy of the CT state (see *e.g.* 3.3.2 and 3.3.3 in Ref. [22], and the work by Koen Vandewal and co-workers [61, 119, 120]).

Eq. (4.1.4) is valid for situations when second-order (bimolecular) recombination is the dominating recombination mechanism for free carriers inside the bulk, provided that surface recombination is absent. In the case of additional bulk recombination channels, such as trap-assisted recombination, a voltage dependence in  $\beta_R$  is to be expected, as discussed in Section 2.4.1. Accordingly, for a free-carrier recombination rate of the order  $\delta$ , we expect

$$qV_{oc} \propto mkT \ln (G/\text{m}^{-3}\text{s}^{-1}), \quad (4.1.5)$$

where the slope  $m$ , referred to as the light ideality factor, is given by  $m_R \equiv 2/\delta$  [118] [Paper 10]. When trap-assisted recombination (via midgap states) dominates, we have  $m_R = 2$  [121]. If the dominating bulk recombination mechanism between free carriers occurs through trap-assisted recombination via tail-states having an exponential distribution [Paper 5], one instead expects  $m_R \approx 2/(1 + kT/E_{ch})$ , where  $E_{ch} > kT$  is the characteristic trap depth [122]. Light-intensity-dependent  $V_{oc}$  measurements, sometimes also referred to as the Suns- $V_{oc}$  method [101], can thus be used to probe the dominating recombination mechanism.

#### 4.1.2 Charge transport *vs.* bulk recombination

In low-mobility semiconductors, the charge collection of photogenerated carriers is generally also limited by the charge transport [123–127]. The shape of the photocurrent is subsequently determined by the competition between charge-carrier extraction and recombination in the active layer, and depends on the dominating recombination mechanism.

#### The case with constant lifetimes

The case when photogenerated carriers have a constant bulk recombination lifetime is discussed briefly here. This type of situation may occur when trap-assisted recombination via deep trap-states is dominate (*cf.* section 2.4.1): the lifetime for holes in the (electron-dominated) cathode side of the active layer is given by  $\tau_p$ , whereas the lifetime of electrons in the (hole-dominated) anode side of the active layer is given by  $\tau_n$ . In case of constant recombination lifetimes, the current is typically analyzed in accordance with the Hecht equation [128].

This equation assumes that the transport of photogenerated carriers is drift-dominated and neglects diffusion. The electric field is assumed constant (of  $x$ ), with the electron and hole current being zero at the anode and cathode, respectively (selective contacts). The current is then given by [129]

$$J_{ph} = -qGd \left( \frac{L_{dr}}{d} \right) \left[ 1 - \exp \left( -\frac{d}{L_{dr}} \right) \right], \quad (4.1.6)$$

for  $F \leq 0$ , where  $L_{dr} = L_{dr,n} + L_{dr,p}$  and

$$\begin{aligned} L_{dr,n} &= \mu_n \tau_n |F|, \\ L_{dr,p} &= \mu_p \tau_p |F| \end{aligned} \quad (4.1.7)$$

are the drift lengths for electrons and holes, respectively. As expected, at high electric field strengths, when  $L_{dr} \gg d$ ,  $J_{ph} \rightarrow -qGd$ . Under these circumstances, the photoinduced carriers are extracted fast enough to avoid recombination within the active layer. Conversely, for  $L_{dr} \ll d$ , the recombination within the active layer is substantial and the magnitude of the photocurrent is heavily reduced:  $J_{ph} \approx qG [\mu_n \tau_n + \mu_p \tau_p] F$ . The  $\mu\tau$ -product represents the key material parameter to be maximized to enhance charge collection.

### The case with bimolecular bulk recombination

An expression analogous to the Hecht equation can also be obtained for the case when bimolecular bulk recombination dominates. If the impact of the dark carriers is negligible and the currents are dominated by drift, the continuity equations simplify as

$$\mu_n F \frac{dn}{dx} = -G + \beta_R np, \quad (4.1.8)$$

$$\mu_p F \frac{dp}{dx} = G - \beta_R np, \quad (4.1.9)$$

assuming the electric field to be uniform. Then, for selective contacts and



$F \approx (V - V_{oc})/d$ , the photocurrent takes the form<sup>14</sup>

$$J_{ph} = \begin{cases} q\mu_{\text{eff}}\sqrt{\frac{G}{\beta_R}}\frac{(V-V_{oc})}{d} & \text{if } L_{dr}^* \ll d, \\ -qGd & \text{if } L_{dr}^* \gg d, \end{cases} \quad (4.1.10)$$

where  $L_{dr}^* = \mu_{\text{eff}}|F|\tau_\beta$  is an effective drift length,  $\mu_{\text{eff}} = 2\sqrt{\mu_n\mu_p}$  is the effective mobility, and  $\tau_\beta = 1/\sqrt{\beta_R G}$  is the bimolecular recombination lifetime. When the recombination is substantial ( $L_{dr}^* \ll d$ ), the photocurrent is linear with the voltage (analogous to Eq. (4.1.6)); however, a square-root dependence of the generation rate is obtained,  $J_{ph} \propto \sqrt{G}$ . Conversely, when the bulk recombination is negligible, corresponding to the limit of large mobilities, strong electric fields, and/or low intensities, the magnitude of the current saturates to its maximum value  $|J_{ph}| = qGd$ . The characteristic material parameter that needs to be maximized in this case is  $\mu_n\mu_p/\beta_R$ .

In the derivation of Eq. (4.1.10), the impact of the injected carriers was neglected. In the general case described by Eq. (4.1.1), however, the current is governed by both photogenerated and injected carriers, recombining with each other. An analytical current expression that accounts for the injected carriers can be obtained by making the effective approximation  $\int_0^d \exp(qV_{int}/kT)dx = d \exp(q[V - JR_{\text{eff}}]/kT)$  in Eq. (4.1.1), where  $R_{\text{eff}} = \exp(-q[V - JR_{\text{eff}}]/2kT) \times [d/q\mu_{\text{eff}}n_i]$  is the associated transport resistance (per unit area) of the active layer [125, 130]. Based on these considerations, Neher *et al.* showed that the

---

<sup>14</sup>For a uniform  $F < 0$ , taking  $J_n(0) = J_p(d) = 0$ , the solutions to Eq. (4.1.8) and Eq. (4.1.9) are given by  $n(x) = n_- \sqrt{\mu_p/\mu_n}$  and  $p(x) = n_+ \sqrt{\mu_n/\mu_p}$ , where

$$n_{+/-} = \mathcal{A}\sqrt{\frac{G}{\beta_R}} \left\{ \tan\left(\frac{\mathcal{A}d}{L_{dr}^*}\right) \pm \tan\left(\frac{\mathcal{A}}{L_{dr}^*}[d - 2x]\right) \right\}$$

and  $0 \leq \mathcal{A} = \cos(\mathcal{A}d/L_{dr}^*) \leq 1$ . The current,  $J_{ph} = qn(x)\mu_n F + qp(x)\mu_p F$ , then reads

$$J_{ph} = -qGL_{dr}^* \sin\left(\frac{\mathcal{A}d}{L_{dr}^*}\right),$$

where: i)  $\mathcal{A} \rightarrow \pi L_{dr}^*/2d$  for  $L_{dr} \ll d$ , and ii)  $\mathcal{A} \rightarrow 1$  for  $L_{dr}^* \gg d$ .

current can be approximated as [131]

$$J = -qGd \left\{ 1 - \exp \left[ \frac{q(V - V_{oc})}{(1 + \alpha)kT} \right] \right\}, \quad (4.1.11)$$

where  $qV_{oc} = kT \ln (G/\beta_R n_i^2)$  as per Eq. (4.1.4), and  $\alpha = (d/L^*)^2$  with  $L^* = \sqrt{\mu_{\text{eff}} kT \tau_\beta / q}$ . Eq. (4.1.11) reproduces the photocurrent [Eq. (4.1.10)] in the limit of significant ( $\alpha \gg 1$ ) and negligible ( $\alpha \ll 1$ ) bulk recombination, and reduces to Eq. (4.1.3) under conditions when the transport is not limiting the current-voltage characteristics.

### 4.1.3 Diffusion-limited photocurrents

The above considerations all assume selective contacts and neglects the impact of diffusion and surface recombination. However, taking the electric field to be independent of  $x$ , the drift-diffusion equations can be solved analytically for the case of negligible bulk recombination. This type of situation was considered by Sokel and Hughes for a device with non-selective and non-injecting contacts ( $n_{\text{cat}/\text{an}} = p_{\text{cat}/\text{an}} \rightarrow 0$ ). For this case, the photocurrent becomes [132]

$$J_{ph} = -qGd \left( 1 - 2 \left[ \frac{kT}{q(V_{bi} - V)} - \frac{1}{\exp \left( \frac{q[V_{bi} - V]}{kT} \right) - 1} \right] \right). \quad (4.1.12)$$

In this limit, the charge collection of photo-carriers is limited by diffusion and the recombination is exclusively taking place by surface recombination at the contacts. The effect of diffusion becomes important for voltages close to the built-in voltage where a considerable surface recombination is present. The open-circuit condition is obtained at  $V_{oc} = V_{bi}$ , when the extraction of electrons (holes) at the cathode (anode) is exactly balanced by an equal extraction of holes (electrons) at the same contact, resulting in a zero net current.

The effect of introducing bulk recombination and injecting contacts mainly give rise to additional recombination channels, resulting in  $V_{oc} < V_{bi}$ . Con-

comitantly, the implication of Eq. (4.1.12) is that when both contacts are *non-selective*, the upper limit of  $V_{oc}$  is generally given by the built-in voltage [22, 100, 133]. The saturation of  $V_{oc}$  to  $V_{bi}$  at low temperatures or high light intensities is a clear indication that both contacts are non-selective. This indeed occurs in organic Ca/Al/P3HT:PCBM/PEDOT:PSS solar cells, suggesting that Ca/Al and PEDOT:PSS both form non-selective contacts in these devices [133]. The impact of surface recombination, and the role of the charge-carrier selectivity at the contacts is clarified in the next section.

## 4.2 The role of the contacts

In this section, the correlation between surface recombination, the energy levels at the contacts, and the role of charge-carrier selectivity at the contacts in thin-film solar cells based on low-mobility semiconductors is clarified.

### 4.2.1 Simplified analytical model

Insights into how surface recombination and the charge-carrier selectivity, characterized in terms of the surface recombination velocities, at the contacts impact the photocurrent can be gained by extending the analysis of negligible bulk recombination ( $R = 0$ ), discussed in Section 4.1.3 above, to the case with finite surface recombination velocities and injecting contacts. In the following, we assume the extraction of majority carriers (holes at the anode, electrons at the cathode) to be ideal ( $S_P = S_N \rightarrow \infty$ ). Then, for conditions when space-charge effects and bulk recombination are negligible, an analytical solution for the current can then be obtained as

$$J = -qGd[1 - f_S] + J_{S,0} \left[ \exp\left(\frac{qV}{kT}\right) - 1 \right], \quad (4.2.1)$$

where

$$f_S = \left\{ \frac{kT}{q(V_{bi} - V)} - \frac{1}{\exp\left(\frac{q[V_{bi} - V]}{kT}\right) - 1} \right\} \left[ \frac{1}{1 + \frac{v_n}{S_n}} + \frac{1}{1 + \frac{v_p}{S_p}} \right] \quad (4.2.2)$$

describes the surface-recombination-induced reduction of the photocurrent,  $J_{S,0}$  is the dark saturation current component given by Eq. (2.4.8), and

$$v_{p(n)} = \frac{\mu_{p(n)} [V_{bi} - V]}{d \left[ 1 - \exp\left(\frac{q[V - V_{bi}]}{kT}\right) \right]} \quad (4.2.3)$$

is the diffusion velocity for holes (electrons), as before.<sup>15</sup> The current Eq. (4.2.1) is illustrated in Figure 4.1 for the case when the contacts are non-injecting ( $J_{S,0} \rightarrow 0$ ), corresponding to the upper limit for the photocurrent (for  $V < V_{oc}$ ) and the open-circuit voltage as set by the contacts. When both contacts are non-selective, *i.e.*  $S_{n(p)} \gg v_{n(p)}$ , Eq. (4.2.1) reduces back to Eq. (4.1.12), as expected. In this case, the built-in driving force for charge extraction is solely provided by the built-in voltage  $V_{bi}$ , being the upper limit of the open-circuit voltage.

By reducing the surface recombination velocity at one of the contacts, in this case at the cathode, to such an extent that  $S_p < v_p$  (for voltages below  $V_{bi}$ ), the open-circuit voltage can be increased beyond the built-in voltage. This is demonstrated in Figure 4.1(a). In the absence of injection, the effect of

---

<sup>15</sup>For electrons,  $J_n(0) - qGx' = q\mu_n F n(x') + \mu_n kT dn/dx'$ , where  $F = [V - V_{bi}]/d$ . Multiplying with  $\exp(qFx'/kT)$  and integrating from  $x' = 0$  to  $x' = x$  we find

$$n(x) = n(0) e^{-\frac{qFx}{kT}} + \frac{J_n(0)}{q\mu_n F} \left[ 1 - e^{-\frac{qFx}{kT}} \right] - \frac{GkT}{q\mu_n F^2} \left[ e^{-\frac{qFx}{kT}} + \frac{qFx}{kT} - 1 \right].$$

With the conditions  $n(d) = n_{an} \exp(qV_{bi}/kT)$  and  $n(0) = J_n(0)/qS_n + n_{an}$ , solving for  $J_n(0)$  yields

$$J_n(0) = \frac{qv_n}{1 + v_n/S_n} \left\{ n_{an} [e^{qV/kT} - 1] + \frac{Gd}{\mu_n F} \left[ \frac{kT}{qFd} + \left( 1 - \frac{kT}{qFd} \right) e^{\frac{qFd}{kT}} \right] \right\}.$$

An analogous expression can be obtained for  $J_p(d)$ . The total current is given by  $J = -qGd + J_n(0) + J_p(d)$ .

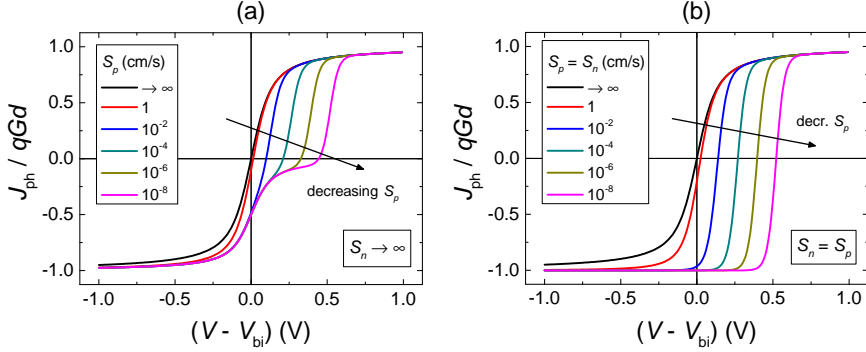


Figure 4.1: Normalized photocurrents of Eq. (4.2.1) for a device with different surface recombination velocities for holes ( $S_p$ ) and electrons ( $S_n$ ) at the cathode and anode, respectively, under conditions when both the bulk recombination and the space-charge effects are negligible ( $R = \rho_{sc} = 0$ ). The parameters used are  $\mu_p = \mu_n = 10^{-4}$  cm<sup>2</sup>/Vs and  $d = 100$  nm, corresponding to  $v_{p,n} = \mu_{p,n}kT/qd \approx 0.26$  cm/s at  $V = V_{bi}$ .

increasing the selectivity at one of the contacts is to increase the open-circuit voltage by

$$\Delta_S \approx \frac{kT}{q} \ln \left( 1 + \frac{\mu_p kT}{q S_p d} \right). \quad (4.2.4)$$

However, as  $S_p$  is decreased, an additional s-shape feature is developed in the  $J$ - $V$  curve for  $V_{bi} < V < V_{oc}$ , the photocurrent changing from  $-qGd/2$  to 0. The reason for the low current levels within this voltage regime can be traced back to the electric field reversing its sign when  $V > V_{bi}$ . As the (reversed) electric field increases, more electrons are driven in the wrong direction towards the non-selective anode, resulting in a considerable surface recombination of electrons at the anode, and reduced current levels.

This issue can be overcome by increasing the selectivity at both contacts simultaneously, to such an extent that  $S_p \ll v_p$  and  $S_n \ll v_n$ . In this case, the surface recombination at both contacts is significantly reduced and the overall

curve, along with the open-circuit voltage, can be shifted to larger voltages, as demonstrated Figure 4.1(b). Although the electric field is reversed for  $V_{bi} < V < V_{oc}$ , the charge collection remains efficient, this is because the surface recombination is negligible below the open-circuit conditions (the photoinduced carriers accumulate in the active layer until they diffuse out at the collecting contacts). In this case, the photocurrent is purely diffusion-driven and the built-in asymmetry is provided by the charge selectivity of the contacts [21].

The above analysis does not account for losses due to bulk recombination. The effect of bulk recombination is to introduce an upper limit to the open-circuit voltage (as given by Eq. (4.1.4)) and reduce the magnitude of the photocurrent at voltages around  $V = V_{oc}$  [134]. We note, however, that in case of ohmic contacts, also an additional photocurrent multiplication effect might be present in the forward bias at  $V > V_{oc}$  [135]. In the remainder of this section, the interplay between surface recombination, bulk recombination, and injection from the contacts is clarified.

#### 4.2.2 Competition between bulk recombination and surface recombination in case of ohmic contacts

Figure 4.2 shows the effect of bulk recombination and injection on the  $J$ - $V$  curves of solar cells with (a) perfectly selective ( $S_p = S_n \rightarrow 0$ ) and (b) non-selective ( $S_p = S_n \rightarrow \infty$ ) ohmic contacts. In the ideal case with perfectly selective contacts, bulk recombination presents the only recombination channel. In this case, the open-circuit voltage is given by Eq. (4.1.4), as expected. However, in case of non-selective contacts, losses due to surface recombination become significant, limiting the open-circuit voltage at low bulk recombination rates.

Figure 4.3 shows the corresponding open-circuit voltages, simulated for a solar cell device with ohmic contacts at different surface recombination velocities. For ohmic contacts, the open-circuit voltage can generally be expressed as

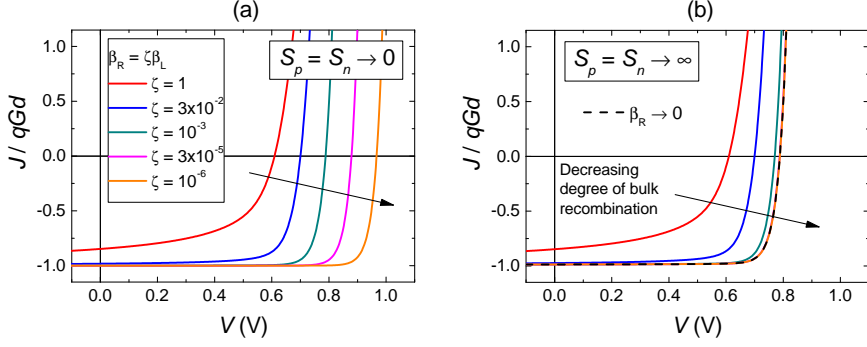


Figure 4.2: Simulated  $J$ - $V$  curves for a solar cell device with ohmic contacts is shown at different bulk recombination coefficients  $\beta_R$ . In (a) the case with perfectly selective contacts ( $S_p = S_n = 0$ ) is shown, corresponding to the ideal case with optimized electrodes. In (b) the case with non-selective contact ( $S_p = S_n \rightarrow \infty$ ). The surface recombination (at non-selective contacts) becomes significant at small  $\beta_R$ .

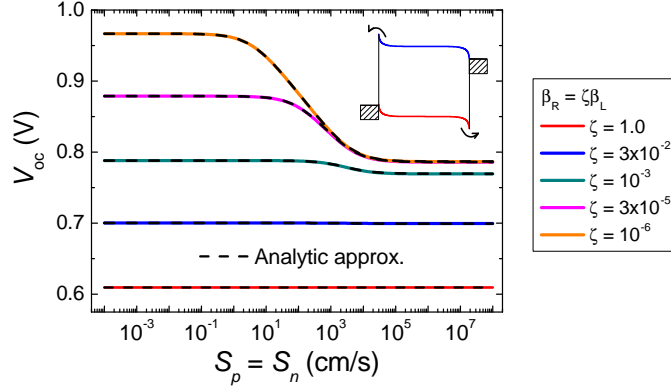


Figure 4.3: The corresponding open-circuit voltages of the solar cell devices with ohmic contacts considered in Figure 4.2 at the different  $\beta_R$ . The open-circuit voltage is shown as a function of the surface recombination velocity  $S_p = S_n$ . The analytical approximations Eq. (4.2.5), with  $v_p^* = v_n^*$  given by Eq. (4.2.8), are indicated by the black dashed lines.

$$qV_{oc} = E_g - kT \ln \left( \frac{[\beta_R + \beta_S] N_v N_c}{G} \right), \quad (4.2.5)$$

where  $\beta_S = \beta_{S,n} + \beta_{S,p}$  is an effective recombination coefficient describing surface recombination of minority carriers at the contacts [**Paper IV**]. For holes at the cathode,

$$\beta_{S,p} = \frac{v_p^* p_{cat}}{n_i^2 d} \left[ 1 + \frac{v_p^*}{S_p} \right]^{-1}, \quad (4.2.6)$$

where

$$v_p^* = \frac{\mu_p kT}{q} \times \left[ \int_0^d \frac{J_p(x)}{J_p(d)} \exp \left( \frac{E_{F,cat} - \varphi_{cat} - E_v(x)}{kT} \right) dx \right]^{-1}. \quad (4.2.7)$$

Analogous expressions are valid for electrons at the anode.<sup>16</sup>

An analytical approximation of Eq. (4.2.7) can be obtained for ohmic contacts when surface recombination is dominating under open-circuit conditions. Assuming Boltzmann statistics, it can then be shown that [**Paper IV**]

$$v_p^* \approx \frac{\mu_p kT}{q \lambda_{cat}}. \quad (4.2.8)$$

The agreement between the simulations and the analytical approximation is excellent. Note that the light-intensity dependence in Eq. (4.2.5) (the light ideality factor) when surface recombination (at ohmic contacts) dominates is the same as when bimolecular bulk recombination dominates, *i.e.*  $m = 1$ . At

---

<sup>16</sup>For surface recombination of electrons at the anode, we instead obtain

$$\beta_{S,n} = \frac{v_n^* n_{an}}{n_i^2 d} \left[ 1 + \frac{v_n^*}{S_n} \right]^{-1},$$

where

$$v_n^* = \frac{\mu_n kT}{q} \times \left[ \int_0^d \frac{J_n(x)}{J_n(0)} \exp \left( -\frac{E_{F,an} + \varphi_{an} - E_c(x)}{kT} \right) dx \right]^{-1}.$$



large  $S_p$  ( $= S_n$ ), the surface recombination is diffusion-limited, with  $V_{oc}$  being independent of  $S_p$ . In this case, Eq. (4.2.5) predicts a mobility dependence of the open-circuit voltage when surface recombination is dominating (high mobilities and low  $\beta_R$ ), consistent with previous studies [51, 89, 136]. At small enough  $S_p$ , in turn, when  $S_p < v_p^*$ , the surface recombination is instead limited by interface kinetics at the contacts. Based on Eq. (4.2.5), the requirement for the cathode contact to be selective is  $\beta_{S,p} < \beta_R$ , corresponding to  $S_p < \beta_R n_{cat} d$ .

The surface recombination at  $V = V_{oc}$  also increases with decreasing active layer thickness,  $\beta_{S,p} \propto 1/d$ . Noting that the average photogeneration rate is related to the saturated photocurrent via  $|J_{ph,sat}| = qGd$ , the dark saturation current  $J_0 = |J_{ph,sat}| \exp(-V_{oc}/kT)$  will then be independent of  $d$  if surface recombination is dominating, whereas a linear dependence of  $d$  is expected when bulk recombination dominates. This was recently demonstrated by Zonno *et al.* [137]; based on this method, organic solar cell structures where surface recombination is dominating could be experimentally identified. It should be stressed, however, that a different situation applies in the case when one or both of the contacts are non-ohmic.

### 4.2.3 Interplay between bulk recombination and surface recombination at non-ohmic contacts

The case when one of the contacts is non-ohmic is considered next. A non-ohmic contact might be the result of non-optimized or degraded energy levels at the electrode. In particular the energetics at low-WF metal cathodes (which are sensitive to oxygen) and metal-oxide-based electrodes is known to change during operating and/or processing conditions [138–142]. Figure 4.4 shows the effect of a non-ohmic contact at the cathode. Here, the anode is assumed perfectly selective ( $S_n = 0$ ) and ohmic for holes. Depending on whether the surface recombination of holes at the cathode is limited by diffusion (large  $S_p$ ) or by interface kinetics at the cathode contact (small  $S_p$ ), different scenarios might occur.

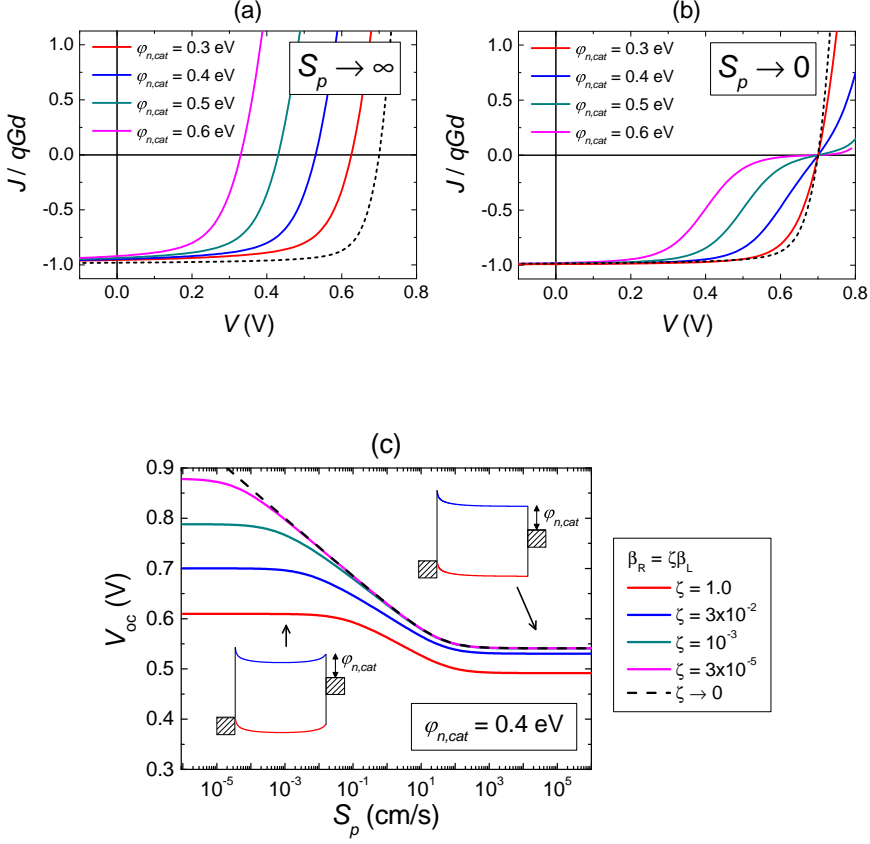


Figure 4.4: The effect of a non-ohmic contact at the cathode. In (a) and (b), the simulated  $J$ - $V$  curves for the case when the cathode contact is non-selective ( $S_p \rightarrow \infty$ ) and perfectly selective ( $S_p \rightarrow 0$ ) at different electron-injection barriers  $\varphi_n$  at the cathode, assuming  $\zeta = 3 \times 10^{-2}$ . The short-dashed line depicts the case when the cathode contact is ohmic. In (c), the corresponding open-circuit voltage as a function of  $S_p$ , at different  $\beta_R = \zeta\beta_L$ , is shown for  $\varphi_{n,cat} = 0.4$  eV. The insets in (c) shows typical energy level diagrams at open-circuit conditions for large  $S_p$  (upper diagram, to the right) and small  $S_p$  (lower diagram, to the left). In the simulations, the anode is assumed perfectly selective ( $S_n = 0$ ) and ohmic for holes; the other parameters are the same as in Figure 4.2 and Figure 4.3.

### Diffusion-limited surface recombination

If the cathode is non-selective ( $S_p \gg v_p$ ), two competing loss mechanisms will be present: diffusion-limited surface recombination (of holes at the cathode) and bulk recombination. When the density of photoinduced carriers is small (low intensities),  $n_{ph} \ll n_{cat} = N_c \exp(-\varphi_{n,cat}/kT)$ , the open-circuit voltage is controlled by the dark current. In this case, if  $J_{S,0} \ll J_{R,0}$ , the bulk recombination is dominating and the open-circuit voltage is directly given by Eq. (4.1.4). Conversely, if  $J_{S,0} \gg J_{R,0}$ , the bulk recombination is negligible and surface recombination dominates at open-circuit conditions; *as per* Eq. (4.2.1), the open-circuit voltage for  $V_{oc} \leq V_{bi}$  then reads

$$qV_{oc} = E_g - \varphi_{n,cat} - kT \ln \left( \frac{v_p^* N_v}{Gd} \right), \quad (4.2.9)$$

where  $v_p^* = v_p/[1 - f_S]$ , with  $v_p$  given by Eq. (4.2.3) and  $f_S$  given by Eq. (4.2.2) (with  $S_n = 0$  and  $S_p = \infty$ ). In this situation, the open-circuit voltage is limited by diffusion-induced surface recombination of holes at the cathode. For  $V_{bi} - V_{oc} \gg kT/q$ ,  $v_p^*$  can be approximated as

$$v_p^* \approx \frac{\mu_p [V_{bi} - V_{oc} + kT/q]}{d}. \quad (4.2.10)$$

As  $V_{oc} \rightarrow V_{bi}$ , however, the surface recombination current  $J_p(d)$  (balanced by  $-J_n(d)$ ) is maximized; a further increase in  $V_{oc}$  is compensated by an equal reduction in  $b/q$  (effective increase in  $V_{bi}$ ), leaving the flat-band condition unchanged, and  $v_p^* \rightarrow 2\mu_p kT/qd$  [**Paper IV**]. The open-circuit voltage as a function of the light intensity is shown in Figure 4.5(a).

At intermediate carrier concentrations, when i) the electron density  $n_{bulk}$  well inside the active layer is high enough for bulk recombination to become limiting ( $n_{bulk} \sim \sqrt{G/\beta_R}$ ), and ii)  $n_{bulk} > n_{cat}$ , a transition from the low-concentration limit to an intermediate regime takes place. In this case, the surface recombination-controlled zone is restricted to a region of thickness  $L^* \approx$

$\sqrt{\mu_{\text{eff}} kT \tau_{\beta} / q}$  adjacent to the cathode (at open-circuit conditions) [**Paper IV**]. The surface recombination at the cathode is accompanied by an internal voltage loss  $\Delta E_{Fn} = kT \ln(n_{\text{bulk}}/n_{\text{cat}})$  over this region [**Paper V**]. The corresponding open-circuit voltage can then be found as

$$qV_{oc} = E_g - \varphi_{n,\text{cat}} - \frac{kT}{2} \ln \left( \frac{\mu_p \beta_R N_v}{\mu_n G} \right). \quad (4.2.11)$$

An interesting feature of Eq. (4.2.11) is the factor of 1/2 appearing in front of the logarithm, implying that the light ideality factor is halved ( $m = m_R/2$ ), with respect to the one expected for Eq. (4.1.4), when this regime is entered. This feature was recently verified by light-intensity-dependent  $V_{oc}$  measurements by Solak *et al.* [143, 144], and is consistent with experimental  $V_{oc}$ - $T$  characteristics presented by Rauh *et al.* [133]. The above analytical findings (Eq. (4.2.9) and Eq. (4.2.11)) are also consistent with recent work by Spies *et al.* [145]. Note that the open-circuit voltage is directly proportional to the injection barrier (or the WF of the non-ohmic contact), this is a characteristic feature of when a contact (in this case the cathode) is limiting the open-circuit voltage [118, 146, 147].

We note that, if also the anode is allowed to be non-selective ( $S_n \gg v_n$ ), at high enough carrier concentrations, the photoinduced carrier densities within the active layer eventually exceed the majority carrier densities at both contacts ( $n_{\text{bulk}} > n_{\text{cat}}, p_{\text{an}}$ ). In this case, the situation discussed in Section 4.1.3 is approached and the open-circuit voltage saturates as  $V_{oc} \rightarrow V_{bi,0} = [E_g - \varphi_{n,\text{cat}} - \varphi_{p,\text{an}}]/q$ . This kind of situation might arise either at high light intensities, low temperatures, or high injection barriers at the contacts, however, only if both of the contacts are non-selective [22]. If the bulk recombination dominates within the active layer, the open-circuit voltage can in this case be summarized by

$$qV_{oc} \approx E_g - \max \left( \varphi_{n,\text{cat}}, \frac{kT}{2} \ln \left[ \frac{\mu_n \beta_R N_c^2}{\mu_p G} \right] \right) - \max \left( \varphi_{p,\text{an}}, \frac{kT}{2} \ln \left[ \frac{\mu_p \beta_R N_v^2}{\mu_n G} \right] \right), \quad (4.2.12)$$

for non-selective contacts, as pointed out in [**Paper V**].

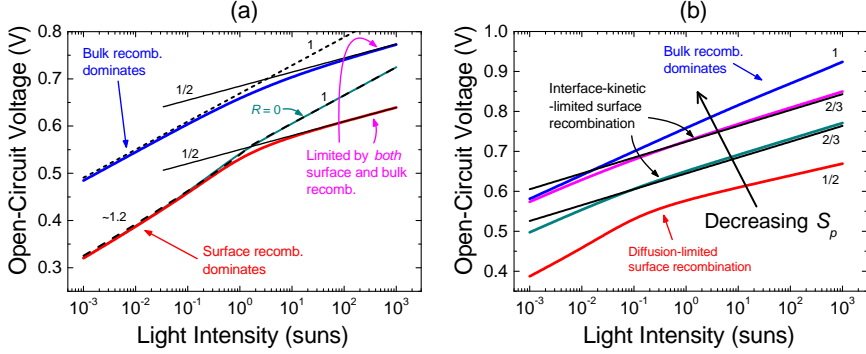


Figure 4.5: (a) Open-circuit voltage as a function of the photogeneration rate (light intensity), for a solar cell device with a non-selective contact at the cathode. The cases for strong and weak bulk recombination are shown. The black lines correspond to Eq. (4.1.4) (short-dashed), Eq. (4.2.9) (dashed), and Eq. (4.2.11) (solid). The corresponding light ideality factors are indicated by the numbers. (b) The increase of the open-circuit voltage obtained by decreasing the surface recombination velocity for holes at the cathode is demonstrated. At non-selective contacts, the surface recombination is limited by diffusion. As the charge-carrier selectivity is increased, the surface recombination becomes limited by interface kinetics at the cathode contact. The solid black lines correspond to Eq. (4.2.13). The anode is assumed perfectly selective and ohmic for holes ( $S_p = 0$ ).

### Interface-kinetic-limited surface recombination

We return to the case with  $S_n = 0$  and variable  $S_p$ , presented in Figure 4.4(c). At small  $S_p$ , an increase of the open-circuit voltage is obtained. This occurs when  $S_p < v_p^*$  and the surface recombination of holes becomes limited by kinetics at the cathode contact. As the open-circuit voltage is increased beyond  $V_{bi}$ , however, an s kink is developed in the  $J$ - $V$  curve [**Paper VI**]. Analogous to the situation in Figure 4.1(a), this occurs when the average electric field with the active layer is reversed. This is demonstrated in Figure 4.4(b) for the limit  $S_p = S_n = 0$ , when surface recombination is absent and the open-circuit voltage is fixed at  $V_{oc} = V_{oc,max}$ , as given by Eq. (4.1.4). It can be seen that as  $V_{bi}$  ( $= [E_g - b - \varphi_{n,cat}]/q$ ) is decreased below  $V_{oc}$ , with increasing injection barrier,

the inflection point of the  $s$  kink is shifted in the negative voltage direction (the interval  $V_{bi} < V < V_{oc,max}$  grows larger). Noting that a large accumulation of injected holes is present at the hole-blocking cathode contact for  $V > V_{bi}$  (Section 2.3.7), the low current levels at  $V_{bi} < V < V_{oc}$  are in this case mainly caused by the recombination of photogenerated carriers (diffusing against the electric field) with injected holes.

The behavior in the  $S_p$ -dependent  $V_{oc}$  region, seen at moderate  $S_p$  in Figure 4.4(c), can be explained in the following way. When bulk recombination is significant at open-circuit conditions, on average, only electrons within a distance  $L_n^{**}$  from the cathode can be extracted at the cathode:  $J_n(d) = -qGL_n^{**}$ . Here,  $L_n^{**} = \sqrt{\mu_n kT \tau_n^{**}/q}$  is a reduced effective diffusion length for electrons, with  $\tau_n^{**}$  being the associated recombination lifetime. Since electrons are predominantly recombining with injected holes accumulating at the cathode contact, we expect  $\tau_n^{**} \sim 1/\beta_R p(d)$ , where  $p(d) = p_{cat} \exp(qV_{oc}/kT)$  in accordance with Eq. (2.3.16). At  $V = V_{oc}$ , this electron current is exactly balanced by an interface-kinetic-limited surface recombination current of holes at the cathode,  $J_p(d) = qS_p p(d)$ . The corresponding open-circuit voltage can then be obtained as

$$qV_{oc} = E_g - \varphi_{n,cat} - \frac{2}{3}kT \ln \left( K \frac{S_p N_v^{3/2}}{G} \right), \quad (4.2.13)$$

where  $K \sim (\mu_n kT/q\beta_R)^{-1/2}$  is determined by material parameters of the active layer; a more rigorous treatment yields [**Paper IV**]

$$K \approx \frac{\beta_R}{\mu_n} \sqrt{\frac{8\varepsilon\varepsilon_0}{kT}} \left[ \sqrt{1 + \frac{8\varepsilon\varepsilon_0\beta_R}{q\mu_n}} + 1 \right]^{-1}, \quad (4.2.14)$$

related to  $L_n^{**}$  via  $L_n^{**} = K^{-1}/\sqrt{p(d)}$ . A distinguishing feature of Eq. (4.2.13) is the additional factor of  $2/3$  in front of the logarithm. Consequently, under conditions when bulk recombination dominates within the active layer, but the open-circuit voltage is controlled by interface-kinetic-limited surface recombina-

tion at the non-ohmic contact, a light ideality factor of  $m = 2/3$  is expected; see Figure 4.5(b). This is experimentally verified in Section 4.4.3.

In general, Eq. (4.2.13) is no longer valid when either i) the recombination within the bulk is small, corresponding to low light intensities and/or high mobilities, or ii)  $S_p \rightarrow 0$ , corresponding to the case when the surface recombination becomes negligible compared to the recombination in the bulk. After taking the cases i) and ii) into account, Eq. (4.2.13) can be generalized as **[Paper IV]**

$$qV_{oc} = E_g - kT \ln \left( \frac{\left[ \beta_R + \frac{S_p}{n_{cat}d_{eff}} \right] N_c N_v}{G} \right), \quad (4.2.15)$$

for  $S_p \ll v_n^*$ , where  $d_{eff} = L_n^{**}$  for  $L_n^{**} \ll d$  and  $d_{eff} = d$  for  $L_n^{**} \gg d$ . Consequently, at negligible bulk recombination ( $d_{eff} = d$ ), the open-circuit voltage simplifies as  $qV_{oc} = E_g - \varphi_{cat} - kT \ln(S_p N_v / Gd)$ . Under these conditions, a situation similar to the case depicted in Figure 4.1(b) is encountered.

On the other hand, when the hole surface recombination velocity at the cathode becomes small enough for  $S_p < \beta_R n_{cat} d_{eff}$ , the open circuit voltage saturates to the upper limit set by bulk recombination:  $V_{oc} \rightarrow V_{oc,max}$ . Hence, to avoid losses due to surface recombination,  $S_p$  needs to be smaller than  $\beta_R n_{cat} d_{eff}$ . Unsurprisingly, for a smaller electron-injection barrier (*i.e.* larger  $n_{cat}$ /smaller  $p_{cat}$ ) and/or a larger bulk recombination coefficient, a less selective contact is required in order to avoid surface recombination. Note that for ohmic contacts ( $d_{eff} \rightarrow d$ ), Eq. (4.2.15) becomes identical to Eq. (4.2.5) (with  $S_p \ll v_p^*$  and  $S_n = 0$ ).

#### 4.2.4 Poor extraction of majority carriers at the contacts

Thus far we assumed the extraction of majority carriers at the contacts, *i.e.* holes at the anode and electrons at the cathode, to be excellent ( $S_P = S_N \rightarrow \infty$ ). In the following, we consider the case when this assumption is violated. A reduced extraction rate of electrons at the cathode contact may be caused by poor interface quality, the formation of an unintentional oxide layer at the contact

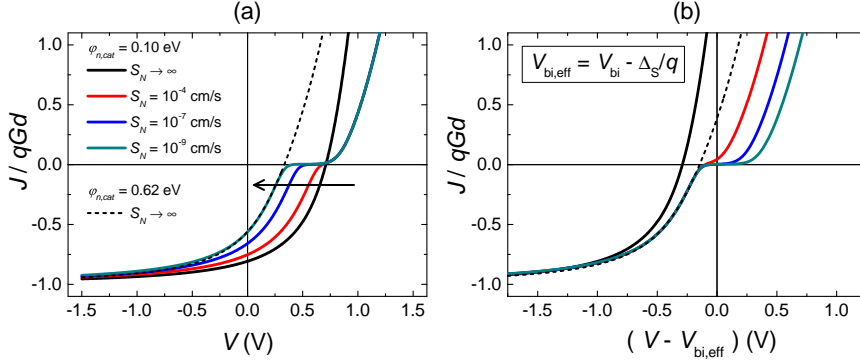


Figure 4.6: The case with non-ideal extraction of majority carriers at the cathode. In (a) simulated current-voltage curves for a device under illumination with different reduced surface recombination velocities  $S_N$  for electrons at the cathode are shown. In (b), the corresponding currents are plotted vs.  $(V - V_{bi,eff})$ , where  $V_{bi,eff} \equiv V_{bi} - \Delta_S$  and  $\Delta_S$  is given by Eq. (4.2.16). The dashed thin line corresponds to the case  $S_N \rightarrow \infty$ , but where the injection barrier at the cathode has been increased by the corresponding  $\Delta_S$  for  $S_N = 10^{-9}$  cm/s. The bulk recombination within the active layer is strong; the parameters are given in [Paper V].

[29, 148, 149], or if an energy barrier (energy level offset) for extraction is present at the active layer-electrode interlayer interface [150, 151]. This may qualitatively be described by an effectively reduced surface recombination velocity for electrons at the cathode  $S_N$  (see Section 2.2.2).

The effect of a reduced surface recombination velocity  $S_N$  for electrons at the cathode is shown in Figure 4.6. Under conditions when  $S_N$  is significantly reduced, a considerable electron accumulation of majority carriers will be present at the cathode contact [29]. The corresponding  $J$ - $V$  curve is plagued by an s kink in the fourth quadrant, as illustrated in Figure 4.6(a). The behavior in Figure 4.6(a) is inverted relative to the one in Figure 4.1(a), with the  $J$ - $V$  curve below  $V_{oc}$  in this case being shifted in the negative voltage direction with decreasing  $S_N$ . Analogous to Eq. (4.2.4), this shift can be described by  $\Delta_S = kT \ln \left( 1 + \mu_n kT / q S_N \tilde{L}_n \right)$ , where  $d$  has been replaced by an effective diffusion length  $\tilde{L}_n$  to account for recombination of electrons inside the active



layer [**Paper V**]. If the recombination inside the active layer is significant, the cathode side of the active layer ( $x > d/2$ ) is dominated by electrons and we may approximate  $\tilde{L}_n \approx d/2$ . Hence,

$$\Delta_S = kT \ln \left( 1 + \frac{2\mu_n kT}{qS_N d} \right). \quad (4.2.16)$$

As demonstrated in Figure 4.6(b), Eq. (4.2.16) may be interpreted as an effective increase of the electron-injection barrier at the cathode. Below the open-circuit voltage, the solar cell thus behaves as a device having an effectively reduced built-in voltage  $V_{bi,\text{eff}} = V_{bi} - \Delta_S/q$ .

### 4.3 The impact of space charge on the photocurrent

The charge collection in low-mobility semiconductor devices is also strongly sensitive to the presence of space-charge regions [127, 152–157]. The effect of a space-charge region is to redistribute the electric field within the active layer, typically resulting in inefficient charge collection and large recombination. Space-charge-limited photocurrents caused by doping and imbalanced mobilities, either within the active layer or in the vicinity of the contact, are discussed in this section.

#### 4.3.1 The influence of a doping-induced space-charge region

A source for degraded device performance in low-mobility solar cells is unintentional doping of the active layer [97]. The doping can be caused by impurities [Paper 6], or oxidation of the active layer in presence of oxygen and/or water (see [**Paper II**] and references therein). If the active layer is *p*-doped, with a high enough concentration of negatively charged dopants within the active layer, a depleted space-charge region (SCR) of thickness  $w_0 < d$  is formed within the layer, adjacent to the cathode (see Section 2.3.6). Within the SCR, the charge collection is driven by the electric field, while in the rest of the active layer (the

field-free quasi-neutral region), the charge collection is driven by diffusion [158].

Since the electric field is mainly concentrated to the thin space-charge region, the recombination of photogenerated carriers within thin region is expected to be negligible, and the photocurrent density can be expressed as  $J_{ph} = -qG_L w_0 + J_{NR}$ , where  $J_{NR}$  is the photocurrent contribution from the quasi-neutral region. The hole density within the hole-dominated quasi-neutral region is assumed to be unchanged under illumination and given by  $p = N_p$ . The current  $J_{NR}$  is then exclusively consisting of electrons with a characteristic diffusion length and lifetime given by

$$L_n = \sqrt{\frac{\mu_n \tau_n kT}{q}}, \quad \tau_n = \frac{1}{\beta_R N_p}, \quad (4.3.1)$$

respectively, within the quasi-neutral region. Assuming that the depletion region is acting as a sink for photoinduced electrons ( $n(x_j) \approx 0$ ), the diffusion-driven electron current  $J_n(x) = qD_n dn/dx$  originating from the quasi-neutral region can be obtained,<sup>17</sup> where  $x_j = d - w_0$  is the thickness of the quasi-neutral region. Neglecting surface recombination at the anode ( $J_n(0) = 0$ ), the current contribution from the quasi-neutral region is found as

$$J_{NR} = -q \int_0^{d-w_0} \left[ G - \frac{n}{\tau} \right] dx = -qGL_n \tanh \left( \frac{d-w_0}{L_n} \right). \quad (4.3.2)$$

We note that, under conditions when the diffusion length is much shorter than the thickness of the quasi-neutral region, the diffusion current simplifies as  $J_{NR} \approx -qGL_n$ .

---

<sup>17</sup>The continuity equation for electrons within the quasi-neutral region, where  $F = 0$  and  $R = \beta N_p n = n/\tau_n$ , is

$$G - \frac{n}{\tau_n} = -\frac{1}{q} \frac{dJ_n}{dx} = -\frac{\mu_n kT}{q} \frac{d^2 n}{dx^2}.$$

After solving this differential equation with respect to  $n(x)$  for  $0 \leq x \leq x_j$ , subject to the boundary conditions  $J_n(0) = 0$  and  $n(x_j) = 0$ , Eq. (4.3.2) is readily obtained.

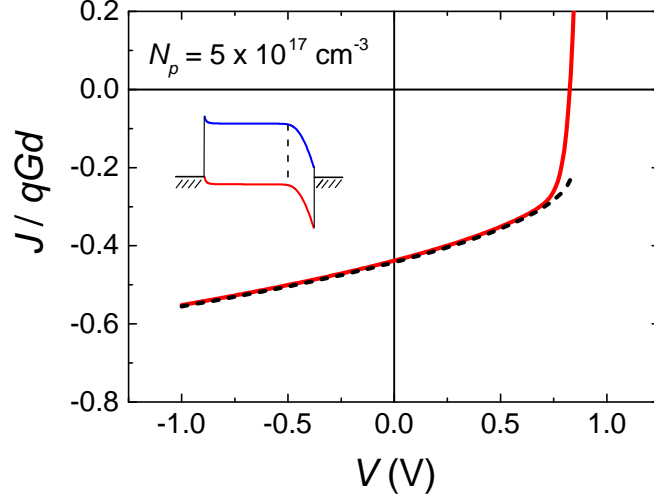


Figure 4.7: Simulated  $J$ - $V$  curve (solid lines) under illumination for a  $p$ -doped active layer with  $N_p = 5 \times 10^{17} \text{ cm}^{-3}$ . The analytical approximation, Eq. (4.3.3), is indicated by the dashed lines. The inset shows the corresponding energy level diagram at short-circuit conditions. The parameters used in the simulations are:  $\mu_n = \mu_p = 10^{-4} \text{ cm}^{-2} \text{ V}^{-1} \text{ s}^{-1}$ ,  $\beta_R = 10^{-2} \beta_L$ ,  $G = 6.24 \times 10^{27} \text{ m}^{-2} \text{ s}^{-1}$ ,  $\varepsilon = 3$ , and  $d = 100 \text{ nm}$ .

The total photocurrent can then be written as

$$J_{ph} = -qG \left[ w_0 + L_n \tanh \left( \frac{d - w_0}{L_n} \right) \right], \quad (4.3.3)$$

where

$$w_0 = \sqrt{\frac{2\varepsilon\varepsilon [V_{bi} - V]}{qN_p}}. \quad (4.3.4)$$

A typical  $J$ - $V$  curve of an organic solar cell with a  $p$ -doped active layer is simulated in Figure 4.7, showing good agreement between the analytical approximation Eq. (4.3.3) and the simulated current. The photocurrent equation

Eq. (4.3.3) states that a voltage dependence of the form  $\sim \sqrt{V_{bi} - V}$  is expected for the photocurrent in case of a doped active layer. Noting that  $N_p$  and  $V_{bi}$  can be obtained by CELIV, as shown in Section 3.2.3, it is in principle possible to extract the ratio  $\mu_n/\beta_R$  (via the diffusion length) from a  $J_{ph}-w_0$  plot of a  $p$ -doped solar cell. Using this method on  $J-V$  curves of  $p$ -doped active layer of P3HT:PCBM (the light-soaked device in Figure 4.10) then yields  $\beta_L/\beta_R \sim 130$  if one assumes  $\beta_L \sim q\mu_n/\varepsilon\varepsilon_0$ .

In the limit of negligible bulk recombination,  $L_n \gg d$ , Eq. (4.3.3) reduces to  $J_{ph} = -qGd$ , as expected. It should be noted that at large  $\beta_R$  ( $\sim \beta_L$ ), the recombination within the depletion region is no longer negligible and Eq. (4.3.3) overestimates the magnitude of the photocurrent under these circumstances.

### 4.3.2 Space-charge-limited photocurrents due to imbalanced mobilities

A space-charge region can also be formed in an undoped active layer, constituting only photoinduced carriers, if the transport is highly unbalanced due to imbalanced mobilities. Under these conditions, the photocurrent is limited by the space charge of the slower carriers [159, 160]. As pointed out by Goodman and Rose, the photocurrent within this region is space-charge-limited, taking the form:  $J_{ph} \sim -qG^{3/4} (9\mu_s\varepsilon\varepsilon_0/8q)^{1/4} (V_0 - V)^{1/2}$  [161], where  $\mu_s$  is the mobility of the slower carrier and  $V_0$  is the potential drop across the space-charge region at  $V = 0$ . This expression, however, does not account for the spatial dependence of the electron and hole currents within the space-charge region.

To account for this effect, consider a device where the mobility of holes is much lower than the mobility of electrons ( $\mu_s = \mu_p \ll \mu_n$ ). Upon illuminating the active layer, the charge build-up of holes will redistribute the electric field, creating a region of a charge-neutral electron-hole plasma inside active layer. The electric field is zero in the neutral region, resulting in a large recombination and  $G \approx R$  within this region. The electric field is instead concentrated to a thin hole-dominated space-charge region of thickness  $w_s$  close to the anode.

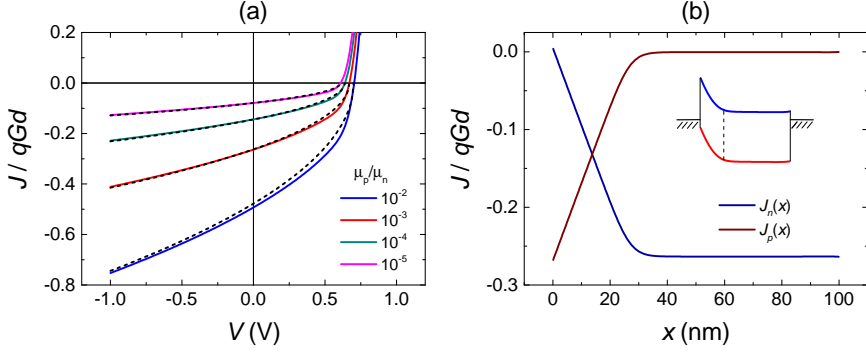


Figure 4.8: (a) Simulated  $J$ - $V$  curves (solid lines) for active layers with imbalanced mobilities. The corresponding analytical approximations, Eq. (4.3.5), are indicated by the dashed lines. In (b), the individual electron and hole currents are simulated for  $\mu_p = 10^{-3}\mu_n$  at short-circuit conditions; the inset shows the corresponding energy level diagram. The parameters used in the simulations are:  $\mu_n = 10^{-4} \text{ cm}^{-2}\text{V}^{-1}\text{s}^{-1}$ ,  $\beta = 10^{-2}\beta_L$ ,  $G = 6.24 \times 10^{27} \text{ m}^{-2}\text{s}^{-1}$ ,  $\varepsilon = 3$ , and  $d = 100 \text{ nm}$ . For the analytical curves, Eq. (4.3.5), we approximate:  $V_0 = V_{oc}$ .

The recombination within the space-charge region is assumed to be negligible ( $R = 0$ ), and the transport dominated by drift. The hole current is subsequently given by  $J_p(x) = q\mu_s pF \approx qG[x - w_s]$  for  $0 \leq x \leq w_s$ , and zero otherwise (for electrons:  $J_n(x) \approx -qGx$  for  $0 \leq x \leq w_s$ , and  $J_n(x) = -qGw_s$  otherwise; see Figure 4.8(b)). Within the space-charge region, the Poisson equation can then be expressed as  $dF/dx = qp/\varepsilon\varepsilon_0 = G[x - w_s]/\mu_s\varepsilon\varepsilon_0 F$ . Taking the electric field to be zero within the neutral zone,  $F(w_s) = 0$ , it then follows that

$$J_{ph} = -qG^{3/4} \left( \frac{4\mu_s\varepsilon\varepsilon_0}{q} \right)^{1/4} (V_0 - V)^{1/2}, \quad (4.3.5)$$

for  $w_s < d$ , where

$$w_s = \sqrt{2(V_0 - V)} \left( \frac{\varepsilon\varepsilon_0\mu_s}{qG} \right)^{1/4}. \quad (4.3.6)$$

In Figure 4.8, Eq. (4.3.5) is compared with simulated  $J$ - $V$  curves for a device under illumination. Indeed, an excellent agreement between the simulations and Eq. (4.3.5) is obtained at highly imbalanced mobilities. Note that the analytical result, Eq. (4.3.5), differs by a factor of  $\sqrt[4]{32/9} \approx 1.37$  from the corresponding phenomenological Goodman and Rose result.

### 4.3.3 The effect of a space-charge region in the vicinity of the electrode

Unintentional doping of the active layer can also be caused by diffusion of dopants originating from the contacts into the active layer or by diffusion of impurities that reacts with the electrodes [162] [Paper 3, Paper 6]. In such cases, the doping concentration is not necessarily uniform throughout the active layer, and might be higher close to the contacts. Taking the doping to be  $p$ -type, a larger  $p$ -doping close to the anode tends to increase the hole conductivity close to this contact, in effect acting as an extension of the contact. An interesting situation occurs, however, when the profile of  $p$ -dopants is increasing towards the cathode. In this case, a thin  $p$ -doped layer may be formed at the cathode, corresponding to doping the region near the cathode with minority carriers.

Consider a profile of negatively charged  $p$ -dopants of the form

$$N_p(x) = \begin{cases} 0 & \text{if } x < d - d_{p,cat}, \\ N_p & \text{if } x \geq d - d_{p,cat}, \end{cases} \quad (4.3.7)$$

where  $d_{p,cat}$  is the extension of the minority carrier dopants into the active layer from the cathode. If the doping concentration  $N_p$  is high, the thickness of the depleted space-charge region is given by **[Paper V]**

$$w_1 = \begin{cases} \sqrt{\frac{2\varepsilon\varepsilon[V_{bi}-V]}{qN_p}} & \text{if } V \geq V_1, \\ d & \text{if } V < V_1, \end{cases} \quad (4.3.8)$$

in accordance with the Poisson equation, where  $V_1 = V_{bi} - \Delta_{p,cat}$  is the cross-over voltage and

$$\Delta_{p,cat} = \frac{qN_p d_{p,cat}^2}{2\epsilon\epsilon_0}. \quad (4.3.9)$$

For voltages  $V > V_1$ , when  $w_1 < d_{p,cat}$ , the entire potential difference drops over the depleted space-charge region of negatively charged dopants. In this case, the potential difference across the undoped region is close to zero, and the local potential distribution within this region is similar to that of a symmetric device with two hole-injecting contacts (*cf.* Figure 2.3(b)).

Under illumination, the recombination within the undoped region is substantial and the contribution to the photocurrent from this region is small. Conversely, due to the strong electric field inside the depleted space-charge region, all carriers generated within the space-charge region are extracted. If the recombination in the undoped region is strong, the photocurrent within this voltage regime is then

$$J_{ph} \approx -qGw_1. \quad (4.3.10)$$

This is identical to the case of bulk doping ( $d_{p,cat} = d$ ) of same doping concentration (when  $L_n \ll w_0$ ). The situation is demonstrated in Figure 4.9. As the applied voltage is reduced below  $V_1$ , ( $V < V_1$ ), on the other hand, the depleted space region reaches its maximum value  $w_1 = d_{p,cat}$ . From this point on, the remaining voltage will mostly drop across the undoped region, then having an electric field given by  $F \approx (V - V_{bi} + \Delta_{p,cat})/d$ . When this occurs the photocurrent will cross-over from the bulk doping-like current regime to an undoped current regime, with the undoped region acting as an active layer with an effectively reduced built-in voltage [**Paper V**]

$$V_{bi,eff} = V_{bi} - \Delta_{p,cat}. \quad (4.3.11)$$

The cross-over between these two current regimes is manifested by an s kink.

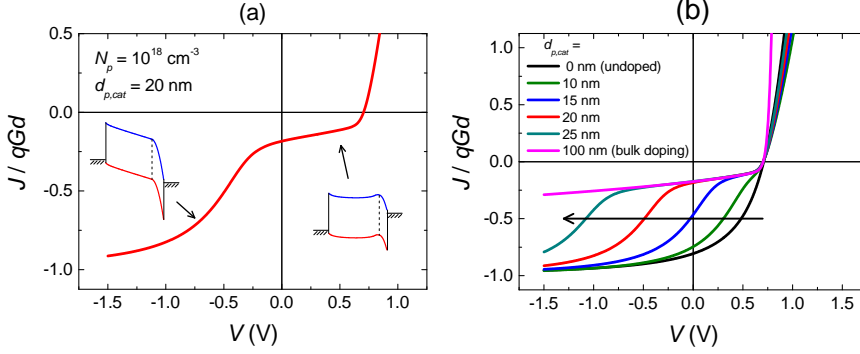


Figure 4.9: Simulated  $J$ - $V$  curves for a solar cell with a  $p$ -doped region, of thickness  $d_{p,cat}$ , in the vicinity of the electron-collecting cathode contact. The thickness of active layer is  $d = 100 \text{ nm}$ . In (a)  $d_{p,cat} = 20 \text{ nm}$  and in (b)  $d_{p,cat}$  is varied between  $d_{p,cat} = 0$  (undoped active layer) and  $d_{p,cat} = d$  (bulk doping). The dopant concentration is  $N_p = 10^{18} \text{ cm}^{-3}$ . The parameters used in the simulations are given in [Paper V].

The s kink is in this case caused by a thin space-charge region screening the electric field within the active layer at low voltages, but which is eventually overcome at larger electric field strengths. This type of behavior can also be induced by trapped majority carriers in the vicinity of the electrode interface [Paper V], *e.g.* due to impurities accumulated at the contact [162], surface dipoles [163], or by a significantly reduced mobility for majority carriers in a region close to the electrodes [164].

## 4.4 Experimental demonstration on inverted organic solar cell devices

In this section, some of the analytical tools and methods developed above, which can be used to clarify charge collection in thin-film devices based on low-mobility semiconductors, are experimentally demonstrated on organic solar cells.



#### 4.4.1 The model system $\text{TiO}_2/\text{P3HT}:\text{PCBM}$ and the light-soaking effect

The model system used for the experiments consists of an active organic layer of P3HT:PCBM, employing  $\text{TiO}_2$  as electron-selective cathode interlayer. This structure has been used as a central ingredient in organic solar cells with inverted device architectures. Figure 4.10 shows the current-voltage characteristics of an inverted solar cell device with a bottom cathode of ITO, covered with  $\text{TiO}_2$ , the organic active layer, and a hole-collecting anode of  $\text{MoO}_3/\text{Ag}$  on top. The experimental details of the system is given in [Paper VI]. The  $J$ - $V$  curves of inverted organic solar cells with a metal-oxide-based electron-selective cathode layer, such as  $\text{TiO}_2$  and  $\text{ZnO}$ , have been reported to require light soaking, typically UV light, before the full efficiency is reached (see [Paper VI] and references therein). Prior to the light soaking (pristine device), s-shaped  $J$ - $V$  characteristics are typically encountered in these devices. By soaking the device in UV light for a certain period of time, the s kink is gradually removed, and the normal "J-shaped" curve obtained. However, in many cases the s kink is restored after storage in oxygen atmosphere.

The poor device performance prior to the light soaking has generally been associated with a reduced collection of electrons. Many groups have attributed the reduced electron collection to poor electron transport (and trapping) within the metal oxide layer, which is significantly improved during light soaking [165–167]. Conversely, a decrease of the WF at the metal-oxide contact is typically observed in conjunction with the UV exposure [168, 169]. In the following, we utilize CELIV and light-intensity-dependent  $V_{oc}$  measurements to clarify the charge collection in the model system presented in Figure 4.10.

#### 4.4.2 Investigating the reason for the s kink in the $J$ - $V$ curve using CELIV

To obtain a deeper understanding of the reason behind these phenomena, we combine the  $J$ - $V$  measurements with CELIV. The blend in this system is prone

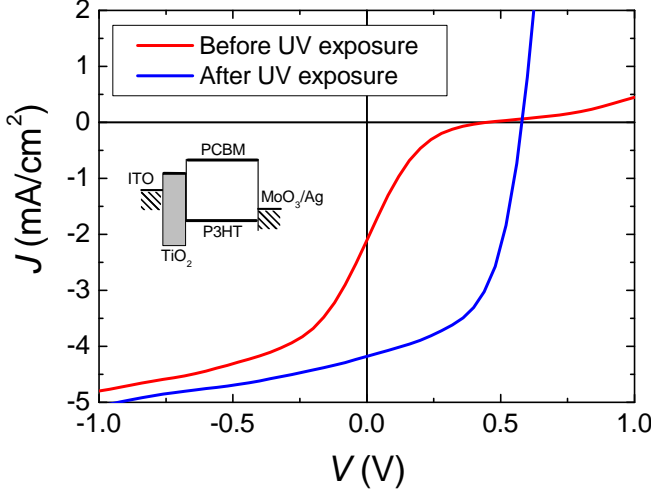


Figure 4.10: Experimental  $J$ - $V$  curves of an inverted P3HT:PCBM solar cell device, with  $\text{TiO}_2$  as electron-selective cathode interlayer. In the pristine device (prior to UV exposure) a prominent kink is present in the  $J$ - $V$  curves. After soaking the device in UV light, the kink gradually disappears. The experimental details are given in [Paper VI].

to  $p$ -doping at thick active layers. Under these conditions, doping-CELIV can be used to monitor changes in the work function of the ITO/ $\text{TiO}_2$  cathode (relative to the WF set by the doping level in the bulk) during the light soaking [Paper VI]. In Figure 4.11, the doping-CELIV current transients of the device in Figure 4.10 is shown at different UV-exposure times. Based on the measurements, it turns out that the extracted built-in voltage is initially very low, but then increases during the light soaking until it saturates to a value typical for well-working P3HT:PCBM devices. The corresponding change in the WF of the cathode is more than 0.7 eV. Clearly, the electron-injection barrier at the cathode is initially very high.

From the CELIV current transients (MIS-CELIV) at forward-biased offset voltages, a large injected charge reservoir can be observed in the pristine device

[**Paper VI**]. The charge reservoir is then gradually diminished during the light soaking. Based on these findings, the s kink is a direct result of the high injection barrier at the electron-selective  $\text{TiO}_2$  contact, which lead to a low onset for hole injection from the anode in the pristine device. Combined with the hole-blocking properties of the  $\text{TiO}_2$ , this creates a large reservoir of injected holes at the electron-extracting cathode contact at voltages  $V_{bi} < V < V_{oc}$ . The subsequent recombination gives rise to the s shape, in line with the discussion regarding Figure 4.4(b) in Section 4.2.3. As the injection barrier at the hole-blocking  $\text{TiO}_2$  cathode is decreased during the UV soaking, the built-in voltage is increased, the onset for injection is shifted to larger voltages and the s shape gradually disappears (as  $V_{bi} > V_{oc}$ ). As the electron-injection barrier is lowered, also the number of electrons present at the contact is increased, further impairing the formation of a hole reservoir after the light soaking.

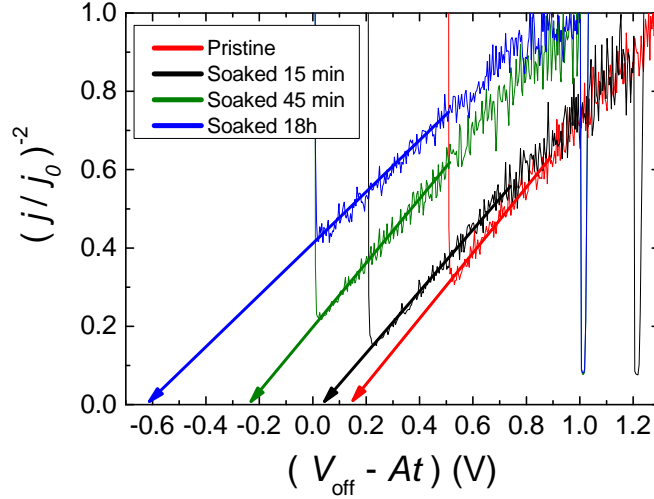


Figure 4.11: Doping-CELIV current transients presented as  $(j/j_0)^{-2}$  vs.  $(V_{\text{off}} - At)$  (Mott-Schottky plot) for the device in Figure 4.10 at different UV exposure times. The doping concentration was found to change negligibly during the soaking.

### 4.4.3 Light-intensity-dependent open-circuit voltage measurements

To gain more insight into the dominating recombination mechanism, light-intensity-dependent open-circuit voltage measurements are very useful. If bulk recombination dominates at open-circuit conditions:  $m = m_R = 2/\delta$ , in accordance with Eq. (4.1.5) and Section 4.1.1. However, the light ideality factor  $m$  is also strongly dependent on surface recombination and the associated contact properties. If surface recombination dominates in a device with *ohmic contacts*, we expect  $m = 1$  (see Section 4.2.2). Conversely, in the case when one of the contacts is non-ohmic, different situations may arise depending on whether the surface recombination at the non-ohmic contact is diffusion-limited or interface-kinetic-limited [**Paper IV**], as summarized in Figure 4.5 (Section 4.2.3). It should be noted that if both contacts are non-selective, we ultimately obtain  $m \rightarrow 0$  at high enough intensities (as  $V_{oc} \rightarrow V_{bi}$ ) [100, 133], in accordance with Eq. (4.2.12).

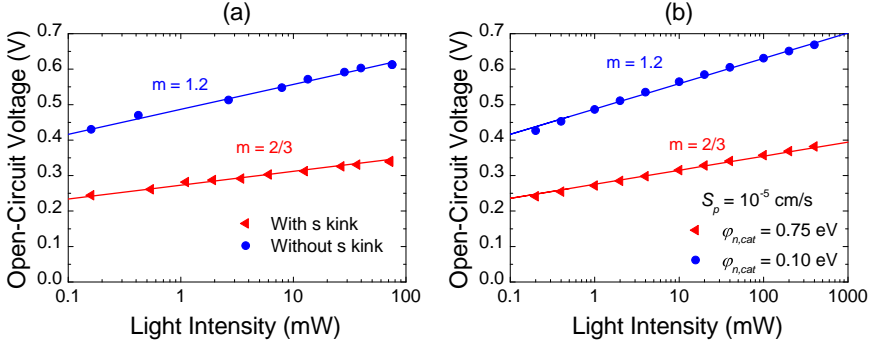


Figure 4.12: (a) Experimental light-intensity-dependent open-circuit voltage measurements (symbols) of the device in Figure 4.10, before (with s shape) and after UV exposure (without s shape). The corresponding light ideality factors  $m = 1.2$  and  $m = 2/3$  are indicated by the solid lines as a guide to the eye. (b) The corresponding qualitative simulations of the system using the drift-diffusion model. The parameters used in the simulation are given in [**Paper VI**]. A green laser (514 nm) was used to avoid UV soaking during the measurements.

In Figure 4.12, light-intensity-dependent  $V_{oc}$  measurements of the inverted solar cell device (from Figure 4.10) is shown. It turns out that for the pristine device, a distinct ideality factor of 2/3 is obtained, consistent with Eq. (4.2.13). This suggests that the open-circuit voltage is in this case controlled by interface-kinetic-limited surface recombination at a non-ohmic contact. This supports the claim that the s kink is caused by a combined effect of un-optimized energy levels (large  $\varphi_{n,cat}$ ) at and inherent hole-blocking properties (reduced  $S_p$ ) of the electron-selective  $\text{TiO}_2$  contact, rather than by poor electron transport properties of the  $\text{TiO}_2$  layer itself. After the light soaking, the open-circuit voltage has increased, and the light ideality factor takes a value of 1.2, consistent with typically observed values in P3HT:PCBM solar cells [170]. The qualitative behavior of the experimental light-intensity-dependent  $V_{oc}$  measurements for the pristine and the light-soaked device are nicely reproduced by drift-diffusion simulations, suggesting a surface recombination velocity  $S_p$  for holes at the  $\text{TiO}_2$ /organic contact on the order of  $S_p \sim 10^{-5}$  cm/s. Note that since the open-circuit voltage in the pristine devices is controlled by interface-kinetic-limited surface recombination ( $S_p \neq 0$ ), holes are still able to be extracted at the  $\text{TiO}_2$ /organic contact, suggesting that some recombination between holes at the interface and electrons (possibly via gap states or recombination centers) in the ITO/ $\text{TiO}_2$  do occur.

#### 4.4.4 The surface recombination velocity of holes at $\text{TiO}_2$ /P3HT

Using the method described in Section 3.3.3, the surface recombination velocity at the  $\text{TiO}_2$ /organic interface can be characterized with CELIV. For the measurements, we use a hole-only ITO/ $\text{TiO}_2$ /P3HT:PCBM/Cu device structure with a hole-injecting Cu anode. From CELIV, the size of the injected charge reservoir,  $Q_{\text{extr}} = \int_0^{t_{\text{pulse}}} \Delta j(t) dt$ , is extracted as a function of the offset voltage  $V_{\text{off}} > V_{bi}$  [**Paper I**]. The corresponding steady-state current density  $J(V_{\text{off}})$  is obtained from the dark  $J$ - $V$  curves. Figure 4.13 shows the extracted hole surface recombination velocities at different dc voltages, using Eq. (3.3.8) (assuming  $\eta = 1$ ). The analysis reveals a value of  $S_p \approx 5.8 \times 10^{-6}$  cm/s for the

surface recombination velocity of holes at  $\text{TiO}_2$ /organic interface, in excellent agreement with the qualitative simulations used to reproduce the behavior of the light-intensity-dependent  $V_{oc}$  measurements in Figure 4.12. This is to be compared to  $v_p = \mu_p kT/qd$  (at flat-band conditions), estimated to be 0.06 cm/s in the organic semiconductor layer.

For comparison, the same method is also used to estimate the hole surface recombination velocities at P3HT interfaces with two different (thin) wide-bandgap insulators:  $\text{ZrO}_2$ /P3HT and  $\text{SiO}_2$ /P3HT, as included in Figure 4.13. The corresponding values for  $S_p$  are close to  $S_p = 2.1 \times 10^{-7}$  cm/s and  $S_p = 4.5 \times 10^{-9}$  cm/s, respectively. As expected, the obtained values at these wide-bandgap charge-blocking layers are lower than at the  $\text{TiO}_2$  contact. It is interesting to note that the obtained values for  $S_p$  in Figure 4.13 are orders of magnitude smaller than values typically encountered in inorganic systems [171]. The low  $S_p$  obtained in this case are likely related to hopping transport dominating the current conduction in these systems (see Section 2.2.2), however, further studies are needed in order to clarify this phenomenon.

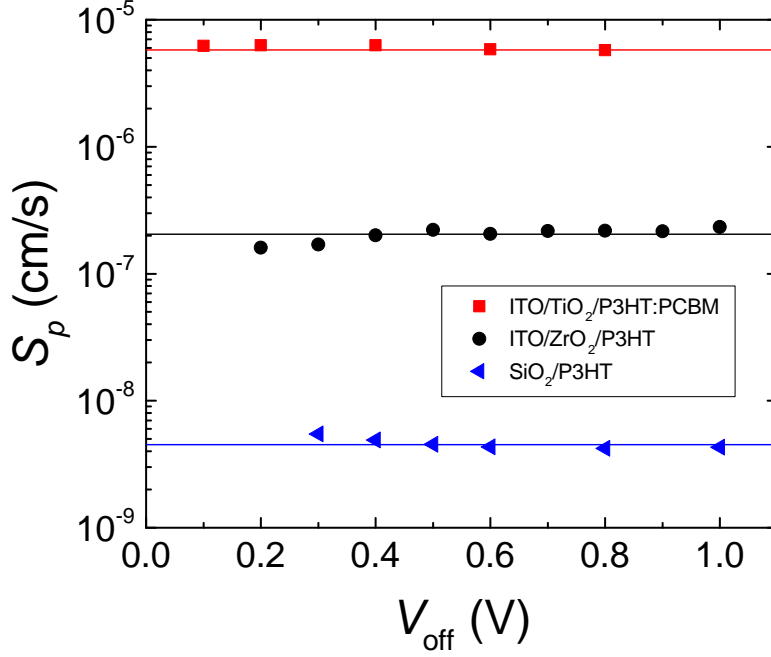


Figure 4.13: Experimental surface recombination velocity for holes at hole-blocking layer/organic interface as measured by CELIV. The red squares show the obtained values for ITO/TiO<sub>2</sub>(7 nm)/P3HT:PCBM, being close  $S_p = 5.8 \times 10^{-6}$  cm/s (indicated by the red solid line). For comparison, also the hole surface recombination velocities obtained at the insulator/organic interfaces in ITO/ZrO<sub>2</sub>(~30 nm)/P3HT/Ag and ITO/SiO<sub>2</sub>(5 nm)/P3HT/MoO<sub>3</sub>/Ag are shown. The corresponding hole surface recombination velocities at ZrO<sub>2</sub>/P3HT and SiO<sub>2</sub>/P3HT are close to  $S_p = 2.1 \times 10^{-7}$  cm/s (black line) and  $S_p = 4.5 \times 10^{-9}$  cm/s (blue line), respectively. Note that the SiO<sub>2</sub>/P3HT data has been corrected for shunts; the details are given in [Paper I]. The ZrO<sub>2</sub>/P3HT device was measured by Dahlström *et al.* [172]; the blocking layers were fabricated by dip-coating.

## CHAPTER 5

### Summary

In this work, the charge collection in thin-film devices, based on low-mobility semiconductors, has been investigated by means of analytical derivations and numerical device simulations, with emphasis on organic diodes and solar cells. The charge collection in these devices is strongly influenced by charge transport, recombination and properties of the contacts. The theoretical aspects of the charge-carrier collection in unipolar and bipolar diode devices have been discussed from the viewpoint of sandwich-type thin-film device structures.

Furthermore, the competition between charge transport and recombination, and the role of the charge-carrier selectivity at the contacts in organic solar cells is investigated. It is found that the open-circuit voltage, corresponding to the point at which the charge collection is exactly balanced by recombination, is strongly dependent on the prevailing contact conditions. Depending on the interplay between the mobilities, the surface recombination velocities (used to describe the charge-carrier selectivity of the contacts), the injection barriers, and the prevailing bulk recombination, different light-intensity and thickness dependences of the open-circuit voltage are expected. Moreover, the current-voltage characteristics typically display an s kink in the case of reduced surface recombination velocity at un-optimized contacts in low-mobility materials. The charge collection is also dependent on the presence of space-charge regions within



## *Chapter 5. Summary*

the active layer. Such space-charge regions may be formed as a consequence of doping or imbalanced mobilities, generally degrading the device performance. The associated space-charge-limited photocurrents exhibit distinctive voltage and light-intensity dependences which can be used to distinguish these from other loss mechanisms.

A popular technique to characterize the mobility in organic solar cells is the charge extraction by linearly increasing voltage technique, or CELIV. In this work, the underlying theory for the mobility determination using CELIV is reviewed and extended to account for contact effects, such as the presence of a built-in voltage and diffusion. Furthermore, we show how the extended theory of CELIV can be used to determine doping concentration, built-in voltage, and the surface recombination velocity. These quantities are key parameters associated with loss mechanisms for charge collection in organic solar cells.

# Bibliography

- [1] R. Meerheim, B. Lüssem, and Karl Leo, Proc. IEEE **97**, 1606 (2009).
- [2] C. Brabec, U. Scherf, and V. Dyakonov, *Organic Photovoltaics* (Wiley VCH, Weinheim, Germany, 2008).
- [3] H. Sirringhaus, Adv. Mater. **26**, 1319 (2014).
- [4] J. Nelson, Mater. Today **14**, 462 (2011).
- [5] L. Dou, J. You, Z. Hong, Z. Xu, G. Li, R. A. Street, and Y. Yang, Adv. Mater. **25**, 6642 (2013).
- [6] O. Inganäs and S. Admassie, Adv. Energy Mater. **26**, 830 (2014).
- [7] M. A. Green, Y. Hoshikawa, E. D. Dunlop, D. H. Levi, J. Hohl-Ebinger, A. W.Y. Ho-Baillie, Prog. Photovoltaics **26**, 3 (2018).
- [8] N.-G. Park, Mater. Today **18**, 65 (2015).
- [9] M. K. Nazeeruddin, and H. Snaith, MRS Bull. **40**, 641 (2015).
- [10] J. P. Correa-Baena, M. Saliba, T. Buonassisi, M. Grätzel, A. Abate, W. Tress, and A. Hagfeldt, Science **358**, 739 (2017).
- [11] J. Nelson, *The physics of solar cells* (Imperial College Press, London, 2003).

## Bibliography

- [12] G. A. Chamberlain, *Solar Cells*, **8**, 47, 1983.
- [13] C. Deibel and V. Dyakonov, *Rep. Prog. Phys.* **73**, 096401 (2010).
- [14] C. W. Tang, *Appl. Phys. Lett.* **48**, 183 (1986).
- [15] S. M. Sze, *Physics of Semiconductor Devices*, 3rd ed. (Wiley & Sons, New York, 1981).
- [16] Sergei Baranovski (edited by), *Charge transport in disordered solids* (John Wiley & Sons, 2006).
- [17] M. Pope and C. E. Swenberg, *Electronic processes in organic crystals and polymers*, 2nd ed. (Oxford University Express, New York, 1999).
- [18] A. Köhler and H. Bässler, *Top. Curr. Chem.* **312**, 1 (2012).
- [19] K. C. Kao and W. Hwang, *Electrical Transport in Solids* (Pergamon Press, Oxford, 1981).
- [20] J. C. Blakesley and N. C. Greenham, *J. Appl. Phys.* **106**, 034507 (2009).
- [21] P. Würfel, *Physics of Solar Cells*, 2nd ed. (Wiley-VCH, Weinheim, Germany, 2009).
- [22] W. Tress, *Organic Solar Cells: Theory, Experiment, and Device Simulation* (Springer, 2014).
- [23] S. Selberherr, *Analysis and Simulation of Semiconductor Devices* (Springer-Verlag, Wien, 1984).
- [24] P. Nelson, *Biological Physics: Energy, Information, Life* (W. H. Freeman Co. Ltd, New York, 2004).
- [25] R. de Leive and H. Moreira, *J. Membrane Biol.* **9**, 241 (1972).
- [26] R. de Leive, N. G. Seidah and H. Moreira, *J. Membrane Biol.* **10**, 171 (1972).

- [27] P. S. Davids, I. H. Campbell, D. L. Smith, J. Appl. Phys. **82**, 6319 (1997).
- [28] L. J. A. Koster, E. C. P. Smits, V. D. Mihailetschi, and P. W. M. Blom, Phys. Rev. B **72**, 085205 (2005).
- [29] A. Wagenpfahl, D. Rauh, M. Binder, C. Deibel, and V. Dyakonov, Phys. Rev. B **82**, 115306 (2010).
- [30] P. de Bruyn, A. H. P. van Rest, G. A. H. Wetzelaer, D.M. de Leeuw, and P.W. M. Blom, Phys. Rev. Lett. **111**, 186801 (2013).
- [31] R. Coehoorn and P. A. Bobbert, Phys. Status Solidi A **209**, 12 (2012).
- [32] Y. Roichman and N. Tessler, Appl. Phys. Lett. **80**, 1948 (2002).
- [33] F. Neumann, Y. A. Genenko, and H. von Seggern, J. Appl. Phys. **99**, 013704 (2006).
- [34] G. A. H. Wetzelaer, L. J. A. Koster, and P.W. M. Blom, Phys. Rev. Lett. **107**, 066605 (2011).
- [35] H. K. Gummel, IEEE Trans. Electron Devices **11**, 455 (1964).
- [36] D. L. Scharfetter and H. K. Gummel, IEEE Trans. Electron Devices **16**, 64 (1969).
- [37] O. Sandberg, *Modellering av laddningstransport och rekombination i polymera solceller* (in Swedish) (M.Sc. Thesis, Åbo Akademi University, Turku, Finland, 2012).
- [38] D. Mendels and N. Tessler, J. Phys. Chem. C **117**, 3287 (2013).
- [39] H. Cordes, S. D. Baranovskii, K. Kohary, P. Thomas, S. Yamasaki, F. Hensel, and J.-H. Wendorff, Phys. Rev. B **63**, 094201 (2001).
- [40] H. Bässler, Phys. Status Solidi B **175**, 15 (1993).

## *Bibliography*

- [41] W. F. Pasveer, J. Cottaar, C. Tanase, R. Coehoorn, P. A. Bobbert, P. W. M. Blom, D. M. de Leeuw, and M. A. J. Michels, *Phys. Rev. Lett.* **94**, 206601 (2005).
- [42] A. J. Mozer, N. S. Sariciftci, A. Pivrikas, R. Österbacka, G. Juška, L. Brassat, H. Bässler, *Phys. Rev. B* **71**, 035214 (2005).
- [43] A. Melianas, V. Pranculis, A. Devižis, V. Gulbinas, O. Inganäs, and M. Kemerink, *Adv. Funct. Mater.* **24**, 4507 (2014).
- [44] A. Melianas, F. Etzold, T. J. Savenije, F. Laquai, O. Inganäs, and M. Kemerink, *Nat. Commun.* **6**, 8778 (2015).
- [45] M. P. Langevin, *Ann. Chim. Phys.* **28**, 433 (1903).
- [46] C. Groves and N. C. Greenham, *Phys. Rev. B* **78**, 155205 (2008).
- [47] C. Deibel, A. Wagenpfahl, V. Dyakonov, *Phys Rev B* **80**, 075203 (2009).
- [48] L. J. A. Koster, V. D. Mihailetschi, P. W. M. Blom, *Appl. Phys. Lett.* **88**, 052104 (2006).
- [49] M. C. Heiber, C. Baumbach, V. Dyakonov, and C. Deibel, *Phys. Rev. Lett.* **114**, 136602 (2015).
- [50] C. M. Proctor, M. Kuik, T.-Q. Nguyen, *Prog. Polymer Science* **38**, 1941 (2013).
- [51] W. Tress, K. Leo, and M. Riede, *Phys. Rev. B* **85**, 155201 (2012).
- [52] T. M. Burke, S. Sweetnam, K. Vandewal, and M. D. McGehee, *Adv. Energy Mater.* **5**, 1500123 (2015).
- [53] A. A. Bakulin, A. Rao, V. G. Pavelyev, P. H. M. van Loosdrecht, M. S. Pshenichnikov, D. Niedzialek, J. Cornil, D. Beljonne, and R. H. Friend, *Science* **335**, 1340 (2012).
- [54] L. Onsager, *J. Chem. Phys.* **2**, 599 (1934).

- [55] C. L. Braun, J. Chem. Phys. **80**, 4157 (1984).
- [56] F. Gao, W. Tress, J. Wang, and O. Inganäs, Phys. Rev. Lett. **114**, 128701 (2015).
- [57] M. Stolterfoht, A. Armin, S. Shoaee, I. Kassal, P. Burn, and P. Meredith, Nat. Commun. **7**, 11944 (2016).
- [58] A. Pivrikas, G. Juška, A. J. Mozer, M. Scharber, K. Arlauskas, N. S. Sariciftci, H. Stubb, and R. Österbacka, Phys. Rev. Lett. **94**, 176806 (2005).
- [59] A. Pivrikas, N. S. Sariciftci, G. Juška and R. Österbacka, Prog. Photovolt: Res. Appl. **15**, 677 (2007).
- [60] G. A. H. Wetzelaer, N. J. Van der Kaap, L. J. A. Koster, and P.W. M. Blom, Adv. Energy Mater. **3**, 1130 (2013).
- [61] J. Benduhn, K. Tvingstedt, F. Piersimoni, S. Ullbrich, Y. Fan, M. Tropicano, K. A. McGarry, O. Zeika, M. K. Riede, C. J. Douglas, S. Barlow, S. R. Marder, D. Neher, D. Spoltore, and K. Vandewal, Nature Energy **2**, 17053 (2017).
- [62] W. Shockley and W. T. Read, Phys. Rev. **87**, 835 (1952).
- [63] R. N. Hall, Physical Review **87**, 387 (1952).
- [64] M. Kuik, L. J. A. Koster, G. A. H. Wetzelaer, and P.W. M. Blom, Phys. Rev. Lett. **107**, 256805 (2011).
- [65] B. Lüssem, M. Riede, and K. Leo, Phys. Stat. Sol. A **210**, 9 (2013).
- [66] M. L. Tietze, L. Burtone, M. Riede, B. Lüssem, and K. Leo, Phys. Rev. B **86**, 035320 (2012).
- [67] H. Ishii, K. Sugiyama, E. Ito, and K. Seki, Adv. Mater. **11**, 605 (1999).
- [68] J. Hwang, A. Wan, A. Kahn, Mater. Sci. Eng. R **64**, 1-31 (2009).

## Bibliography

- [69] S. Braun, W. R. Salaneck, and M. Fahlman, *Adv. Mater.* **21**, 1450 (2009).
- [70] M. Oehzelt, N. Koch, and G. Heimel, *Nat. Commun.* **5**, 4174 (2014).
- [71] J. G. Simmons, *J. Phys. Chem. Solids* **32**, 1987 (1971).
- [72] G. Paasch, H. Peisert, M. Knupfer, J. Fink, and S. Scheinert, *J. Appl. Phys.* **93**, 6084 (2003).
- [73] I. Lange, J. C. Blakesley, J. Frisch, A. Vollmer, N. Koch, and D. Neher, *Phys. Rev. Lett.* **106**, 216402 (2011).
- [74] D. Cheyns, J. Poortmans, P. Heremans, C. Deibel, S. Verlaak, B. P. Rand, and J. Genoe, *Phys. Rev. B* **77**, 165332 (2008).
- [75] Yu. A. Genenko, S. V. Yampolskii, C. Melzer, K. Stegmaier, and H. von Seggern, *Phys. Rev. B* **81**, 125310 (2010).
- [76] D. J. Griffiths, *Introduction to Electrodynamics*, 3rd ed. (Pearson, Upper Saddle River, NJ, 1999), pp. 188-190.
- [77] P. De Visschere, *Solid-State Electronics* **29**, 813 (1986).
- [78] J. D. Jackson, *Classical Electrodynamics*, 3rd ed. (Wiley & Sons, 1999).
- [79] N.W. Ashcroft and N.D. Mermin, *Solid State Physics* (Holt, Rinehart and Winston, New York, 1976), p. 362-364.
- [80] C.R. Crowell, S.M. Sze, *Solid State Electron.* **9**, 1035 (1966).
- [81] M.A. Abkowitz, H.A. Mizes, J.S. Facci, *Appl. Phys. Lett.* **66**, 1288 (1995).
- [82] Yu.N. Gartstein, E.M. Conwell, *Chem. Phys. Lett.* **255**, 93 (1996).
- [83] U. Wolf, V. I. Arkhipov, and H. Bässler, *Phys Rev B* **59**, 7507 (1999).
- [84] V. I. Arkhipov, U. Wolf, and H. Bässler, *Phys Rev B* **59**, 7514 (1999).
- [85] A. Burin and M. Ratner, *J. Chem. Phys.* **113**, 3941 (2000).

- [86] J. J. M. van der Holst, F. W. A. van Oost, R. Coehoorn, and P. A. Bobbert, Phys. Rev. B **80**, 235202 (2009).
- [87] T. Van Woudenberg, P. W. M. Blom, M.C.J.M. Vissenberg, J. N. Huiberts, Appl. Phys. Lett. **79**, 1697 (2001).
- [88] J. C. Scott and G. G. Malliaras, Chem. Phys. Lett. **299**, 115 (1999).
- [89] T. Kirchartz, B. E. Pieters, K. Taretto, and U. Rau, Phys. Rev. B **80**, 035334 (2009).
- [90] E. L. Ratcliff, B. Zacher, and N. R. Armstrong, J. Phys. Chem. Lett. **2**, 1337 (2011).
- [91] M. A. Lampert and P. Mark, *Current Injection in Solids* (Academic Press, New York, 1970).
- [92] P. R. Emtage and J. J. O'dwyer, Phys. Rev. Lett. **16**, 356 (1966).
- [93] O. J. Sandberg *et al.* Unpublished.
- [94] K. E. Lilja, H. S. Majumdar, F. S. Pettersson, R. Österbacka, and T. Joutsenoja, ACS Appl. Mater. Interfaces **3**, 7 (2011).
- [95] K. E. Lilja, H. S. Majumdar, K. Lahtonen, P. Heljo, S. Tuukkanen, T. Joutsenoja, M. Valden, R. Österbacka, and D. Lupo, J. Phys. D: Appl. Phys. **44**, 295301 (2011).
- [96] S. L. M. van Mensfoort and R. Coehoorn, Phys. Rev. B **78**, 085207 (2008).
- [97] T. Kirchartz, W. Gong, S. A. Hawks, T. Agostinelli, R. C. I. MacKenzie, Y. Yang, and J. Nelson, J. Phys. Chem. C **116**, 7672 (2012).
- [98] C.T. Sah, R. N. Noyce, W. Shockley, Proc. Institute of Radio Engineers, 1228 (1957).
- [99] T. Kirchartz, B. E. Pieters, J. Kirkpatrick, U. Rau, and J. Nelson, Phys. Rev. B **83**, 115209 (2011).



## *Bibliography*

- [100] T. Kirchartz, F. Deledalle, P. Shakya Tuladhar, J. R. Durrant, and J. Nelson, *Phys. Chem. Lett.* **4**, 2371 (2013).
- [101] K. Tvingstedt and C. Deibel, *Adv. Energy Mater.* **6**, 1502230 (2016).
- [102] R. H. Parmenter and W. Ruppel, *J. Appl. Phys.* **30**, 1548 (1959).
- [103] G. Juška, K. Arlauskas, M. Viliunas, and J. Kocka, *Phys. Rev. Lett.* **84**, 4946 (2000).
- [104] G. Juška, K. Genevicius, K. Arlauskas, R. Österbacka, and H. Stubb, *Phys. Rev. B* **65**, 233208 (2002).
- [105] G. Juška, K. Arlauskas, M. Viliunas, K. Genevicius, R. Österbacka, and H. Stubb, *Phys. Rev. B* **62**, R16235 (2000).
- [106] C. Deibel, *Phys. Stat. Sol. A* **206**, 2731 (2009).
- [107] S. Bange, M. Schubert, and D. Neher, *Phys. Rev. B* **81**, 035209 (2010).
- [108] J. Lorrmann, B. H. Badada, O. Inganäs, V. Dyakonov, and C. Deibel, *J. Appl. Phys.* **108**, 113705 (2010).
- [109] B. Philippa, C. Vijila, R. D. White, P. Sonar, P. L. Burn, P. Meredith, A. Pivrikas, *Org. Electron.* **16**, 205 (2015).
- [110] N. Nekrasas, K. Genevicius, M. Viliunas, and G. Juška, *Chem. Phys.* **404**, 56 (2012).
- [111] A. Armin, M. Velusamy, P. L. Burn, P. Meredith, and A. Pivrikas, *Appl. Phys. Lett.* **101**, 083306 (2012).
- [112] G. Juška, N. Nekrašas, V. Valentinavicius, P. Meredith, and A. Pivrikas, *Phys. Rev. B* **84**, 155202 (2011).
- [113] G. Juška, N. Nekrašas, and K. Genevicius, *J. Non-Cryst. Sol.* **358**, 748 (2012).

- [114] A. Armin, G. Juška, M. Ullah, M. Velusamy, P. L. Burn, P. Meredith, and A. Pivrikas, *Adv. Energy Mater.* **4**, 1300954 (2014).
- [115] J. Vazgela, K. Genevicius, and G. Juška, *Chem. Phys.* **478**, 126 (2016).
- [116] S. A. Hawks, B. Y. Finck, and B. J. Schwartz, *Phys. Rev. Applied* **3**, 044014 (2015).
- [117] L. J. A. Koster, V. D. Mihailetschi, R. Ramaker, and P.W. M. Blom, *Appl. Phys. Lett.* **86**, 123509 (2005).
- [118] J. C. Blakesley and D. Neher, *Phys. Rev. B* **84**, 075210 (2011).
- [119] K. Vandewal, K. Tvingstedt, A. Gadisa, O. Inganäs, and J. V. Manca, *Nat. Mater.* **8**, 904 (2009).
- [120] K. R. Graham, P. Erwin, D. Nordlund, K. Vandewal, R. Li, G. O. Ngongang Ndjawa, E. T. Hoke, A. Salleo, M. E. Thompson, M. D. McGehee, and A. Amassian, *Adv. Mater.* **25**, 6076 (2013).
- [121] W. Tress, K. Leo, and M. Riede, *Appl. Phys. Lett.* **102**, 163901 (2013).
- [122] T. Kirchartz and J. Nelson, *Phys. Rev. B* **86**, 165201 (2012).
- [123] D. Bartesaghi, I. del Carmen Pérez, J. Kniepert, S. Roland, M. Turbiez, D. Neher, and L. J. A. Koster, *Nat. Commun.* **6**, 7083 (2015).
- [124] M. L. I. Ibrahim, Z. Ahmad, and K. Sulaiman, *AIP Advances* **5**, 027115 (2015).
- [125] U. Würfel, D. Neher, A. Spies, and S. Albrecht, *Nat. Commun.* **6**, 6951 (2015).
- [126] P. Kaienburg, U. Rau, T. Kirchartz, *Phys. Rev. Applied* **6**, 024001 (2016).
- [127] T. Kirchartz, T. Agostinelli, M. Campoy-Quiles, W. Gong, and J. Nelson, *J. Phys. Chem. Lett.* **3**, 3470 (2012).

## *Bibliography*

- [128] K. Hecht, Z. Phys. **77**, 235 (1932).
- [129] R. S. Crandall, J. Appl. Phys. **53**, 3350 (1982).
- [130] S. Schiefer, B. Zimmermann, and U. Würfel, J. Appl. Phys. **115**, 044506 (2014).
- [131] D. Neher, J. Kniepert, A. Elimelech, and L. J. A. Koster, Sci. Rep. **6**, 24861 (2016).
- [132] R. Sokel and R. C. Hughes, J. Appl. Phys. **53**, 7414 (1982).
- [133] D. Rauh, A. Wagenpfahl, C. Deibel, and V. Dyakonov, Appl. Phys. Lett. **98**, 133301 (2011).
- [134] A. Petersen, T. Kirchartz, and T. A. Wagner, Phys. Rev. B **85**, 045208 (2012).
- [135] D. J. Wehenkel, L. J. A. Koster, M.M. Wienk, and R. A. J. Janssen, Phys. Rev. B **85**, 125203 (2012).
- [136] A. Wagenpfahl, C. Deibel, and V. Dyakonov, IEEE J. Sel. Top. Quantum Electron. **16**, 1759 (2010).
- [137] I. Zonno, B. Krogmeier, V. Katte, D. Lübke, A. Martinez-Otero, and T. Kirchartz, Appl. Phys. Lett. **109**, 183301 (2016).
- [138] Y. Zhou, J.W. Shim, C. F. Hernanderz, A. Sharma, K. A. Knauer, A. J. Giordano, S. R. Marder, and B.Kippelen, Phys. Chem. Chem. Phys. **14**, 12014 (2012).
- [139] S. Wheeler, F. Deledalle, N. Tokmoldin, T. Kirchartz, J. Nelson, and J. R. Durrant, Phys. Rev. Appl. **4**, 024020 (2015).
- [140] S. Schäfer, A. Petersen, T. A. Wagner, R. Kniprath, D. Lingenfelser, A. Zen, T. Kirchartz, B. Zimmermann, U. Würfel, X. Feng, and T. Mayer, Phys. Rev. B **83**, 165311 (2011).

- [141] M. Lu, P. de Bruyn, H. T. Nicolai, G.-J. A. Wetzelaer, and P.W. Blom, *Org. Electron.* **13**, 1693 (2012).
- [142] K. Zilberberg, A. Behrendt, M. Kraft, U. Scherf, T. Riedl, *Org. Electron.* **14**, 951 (2013).
- [143] S. Solak, P. W. M. Blom, and G. A. H. Wetzelaer, *Appl. Phys. Lett.* **109**, 053302 (2016).
- [144] S. Solak, A. G. Ricciardulli, T. Lenz, N. I. Craciun, P. W. M. Blom, and G. A. H. Wetzelaer, *Appl. Phys. Lett.* **110**, 163301 (2017).
- [145] A. Spies, M. List, T. Sarkar, and U. Würfel, *Adv. Energy Mater.* **7**, 1601750 (2017).
- [146] V. D. Mihailetschi, P.W.M. Blom, J. C. Hummelen, and M. T. Rispens, *J. Appl. Phys.* **94**, 6849 (2003).
- [147] J. Reinhardt, M. Grein, C. Bühler, M. Schubert, and U. Würfel, *Adv. Energy Mater.* **4**, 1400081 (2014).
- [148] J. C. Wang, X. C. Ren, S. Q. Shi, C.W. Leung, and P. K. Chan, *Org. Electron.* **12**, 880 (2011).
- [149] M. Glatthaar, M. Riede, N. Keegan, K. Sylvester-Hvid, B. Zimmermann, M. Niggemann, A. Hinsch, and A. Gombert, *Solar Energy Mater. Sol. Cells* **91**, 390 (2007).
- [150] W. Tress, K. Leo, and M. Riede, *Adv. Funct. Mater.* **21**, 2140 (2011).
- [151] W. Tress and O. Inganäs, *Solar Energy Mater. Sol. Cells* **117**, 599 (2013).
- [152] V. A. Trukhanov, V. V. Bruevich, and D. Y. Paraschuk, *Phys. Rev. B* **84**, 205318 (2011).
- [153] F. Deledalle, T. Kirchartz, M. S. Vezie, M. Campoy-Quiles, P. S. Tuladhar, J. Nelson, and J. R. Durrant, *Phys. Rev. X* **5**, 011032 (2015).

## *Bibliography*

- [154] J. Wang, L. Xu, Y.-J. Lee, M. De Anda Villa, A. V. Malko, and J. W. P. Hsu, *Nano Lett.* **15**, 7627 (2015).
- [155] J. G. Tait, U.W. Paetzold, D. Cheyns, M. Turbiez, P. Heremans, and B. P. Rand, *ACS Appl. Mater. Interfaces* **8**, 2211 (2016).
- [156] F. F. Stelzl and U. Würfel, *Phys. Rev. B* **86**, 075315 (2012).
- [157] G. F. A. Dibb, M.-A. Muth, T. Kirchartz, S. Engmann, H. Hoppe, G. Gobsch, M. Thelakkat, N. Blouin, S. Tierney, M. Carrasco-Orozco, J. R. Durrant, J. Nelson, *Sci. Rep.* **3**, 3335 (2013).
- [158] W. W. Gärtner, *Phys. Rev.* **116**, 84 (1954).
- [159] V. D. Mihailetschi, J. Wildeman, and P.W. M. Blom, *Phys. Rev. Lett.* **94**, 126602 (2005).
- [160] M. Stolterfoht, A. Armin, B. Philippa, and D. Neher, *J. Phys. Chem. Lett.* **7**, 4716 (2016).
- [161] A. M. Goodman and A. Rose, *J. Appl. Phys.* **42**, 2823 (1971).
- [162] W. R. Mateker, J. D. Douglas, C. Cabanetos, I. T. Sachs- Quintana, J. A. Bartelt, E. T. Hoke, A. El Labban, P. M. Beaujuge, J. M. J. Fréchet, and M. D. McGehee, *Energy Environ. Sci.* **6**, 2529 (2013).
- [163] A. Kumar, S. Sista, and Y. Yang, *J. Appl. Phys.* **105**, 094512 (2009).
- [164] B. Y. Finck and B. J. Schwartz, *Appl. Phys. Lett.* **103**, 053306 (2013).
- [165] C. S. Kim, S. S. Lee, E. D. Gomez, J. B. Kim, and Y.-L. Loo, *Appl. Phys. Lett.* **94**, 113302 (2009).
- [166] B. Ecker, H.-J. Egelhaaf, R. Steim, J. Parisi, and E. von Hauff, *J. Phys. Chem. C* **116**, 16333 (2012).
- [167] B. Romero, G. D. Pozo, E. Destouesse, S. Chambon, and B. Arredondo, *Org. Electron.* **15**, 3546 (2014).

- [168] H. Schmidt, K. Zilberberg, S. Schmale, H. Flügge, T. Riedl, W. Kowalsky, Appl. Phys. Lett. **96**, 243305 (2010).
- [169] M. R. Lilliedal, A. J. Medford, M. V. Madsen, K. Norrman, F. C. Krebs, Sol. Energy Mater. Sol. Cells **94**, 2018 (2010).
- [170] M. Lenes , S. W. Shelton, A. B. Sieval, D. F. Kronholm, J. C. K. Hummelen, and P. W. M. Blom, Adv. Funct. Mater. **19**, 3002 (2009).
- [171] A. Richter, S. W. Glunz, F. Werner, J. Schmidt, and A. Cuevas, Phys. Rev. B **86**, 165202 (2012).
- [172] Staffan Dahlström, Christian Weinberger, Oskar J. Sandberg, Jan-Henrik Smått, Ronald Österbacka, Unpublished (2017).

## *Bibliography*

## Svensk resumé

Solceller är en förnybar energiteknologi som fått alltmer uppmärksamhet. De kommersiella solcellerna på marknaden idag är nästan uteslutande baserade på kristallint kisel. En nackdel med kiselsolcellerna är att dessa är relativt dyra att framställa och kräver en stor mängd råmaterial. Solceller baserade på organiska halvledare är ett attraktivt alternativ till kisel. En organisk solcell består av en diodstruktur med ett tunt aktivt organiskt halvledarlagert mellan två elektroder (anoden och katoden). Fördelen med denna typ av solceller är dess potential för miljövänlig och hållbar produktion i stor skala till ett lågt pris. Nackdelen med organiska solceller är den låga effektiviteten. För att kunna förbättra prestandan och öka på effektiviteten i organiska solceller är det viktigt att förstå den underliggande fysiken bakom de begränsande förlustmekanismerna.

Det organiska halvledarlagret består typiskt av en blandning mellan en halvledande polymer och ett fulleren-baserat halvledarmaterial. Då solljus absorberas i halvledarmaterialet, exciteras elektron-hålpar från grundtillståndet. Dessa elektron-hålpar kan separeras till fria laddningar vid organiska gränssytor inne i det aktiva lagret. De fria elektronerna (hålen) transporteras vidare inne i det aktiva lagret till katoden (anoden), där de extraheras till den yttre kretsen och ger upphov till en ström. På vägen till elektroderna kan elektroner och hål dock rekombinera med varandra och förloras. Denna process är en viktig förlustmekanism i organiska solceller. Förhållandet mellan laddningsextraktion och rekombination i organiska solceller är starkt beroende av laddningstransportegenskaperna i det organiska halvledarmaterialet. Laddningstransporten i halv-



ledare klassificeras ofta enligt dess mobilitet. Medan mobiliteten i kristallint kisel är hög, är den motsvarande mobiliteten i organiska halvledare ofta väldigt låg.

Syftet med denna avhandling är att klargöra fysiken bakom laddningsextraktion av elektroner och hål i diodstrukturer baserade på halvledarmaterial med låga mobiliteter och tunna aktiva lager. Med hjälp av drift-diffusionssimuleringar diskuteras den teoretiska bakgrunden för laddningstransport och extraktion vid kontakterna i tunnfilmsdioder. Denna teori tillämpas sedan på transienta extraktionsmätningar och ström-spänningskurvor i organiska solceller. Förutom förhållandet mellan laddningstransport och rekombination inom det aktiva lagret, är laddningsextraktionen i dessa system också väldigt känslig för icke-ideala kontakter och oavsiktlig dopning av det aktiva lagret. I kombination med transienta laddningsextraktionsmätningar, kan de teoretiska resultaten användas för att identifiera och urskilja dominerande förlustmekanismer, samt användas för att bestämma parametrar relevanta för laddningsextraktionen i organiska solceller.

